RESILIENT MICROGRIDS USING A STATE CONTROLLER

by

Oluwafemi J. Aworo

B.Sc. Obafemi Awolowo University, 2011

M.Sc. The University of Edinburgh, 2015

Submitted to the Graduate Faculty of

Swanson School of Engineering in partial fulfillment

of the requirements for the degree of

Doctor of Philosophy

University of Pittsburgh
2019

UNIVERSITY OF PITTSBURGH

SWANSON SCHOOL OF ENGINEERING

This dissertation was presented

by

Oluwafemi J. Aworo

It was defended on

January 18, 2019

and approved by

Zhi-Hong Mao, Ph.D., Professor
Department of Electrical and Computer Engineering, Department of Bioengineering

Gregory Reed, Ph.D., Professor
Department of Electrical and Computer Engineering

Ervin Sejdic, Ph.D., Associate Professor
Department of Electrical and Computer Engineering

Sylvanus Wosu, Ph.D., Associate Professor
Department of Mechanical Engineering and Materials Science

Dissertation Director: Alexis Kwasinski, Ph.D., Associate Professor
Department of Electrical and Computer Engineering

RESILIENT MICROGRIDS USING A STATE CONTROLLER

Oluwafemi Aworo, Ph.D.

University of Pittsburgh, 2019

Wind energy technology is fast becoming a major component of renewable energy deployment in electric grids. This technology however, has a major challenge of low machine inertia that could impact the frequency stability of the system when deployed in microgrids. The frequency response rate to abrupt load changes becomes an issue when many wind turbines are connected in a microgrid. This dissertation investigates the impact of this low machine inertia on the nominal frequency and voltage of a microgrid. The impact of varying wind conditions on the electrical power output is also studied. The system is modelled in MATLAB/Simulink using a DFIG wind turbine rated at 1.5 MVA. This thesis studies control strategies to bring the system to a stability irrespective of the wind speeds, load conditions or perturbations. This work further focuses on how the state controller is used to improve the power system reliability, availability and resilience during extreme events such as hurricanes, earthquakes and wildfires.

TABLE OF CONTENTS

ACKNOWLEDGEMENT……………..…………………………………...……..xiii

GLOSSARY…………………………...…………………………...……..xiv

1.0 INTRODUCTION…………………………...………………………………...…1

1.1 STATEMENT OF PROBLEM……………………………………………………..3

1.2 SCOPE OF WORK………………………………………………………………5

1.3 AIMS & OBJECTIVES…………………………………………...…………..7

1.4 CONTRIBUTION…………………………………………………………………..7

1.5 OUTLINE OF THE DISSERTATION….………..…………………………...…………8

2.0 RESILIENCE AND RESILIENCE METRICS………………………...…………....….9

2.1 RESILIENCE………………………………………………...………………..…9

2.1.1 Recent impacts of natural disasters……………………………………...…10

2.1.2 Resilience metric…………………………………………………………….12

3.0 RENEWABLE ENERGY SOURCES AND TRANSIENT STABILITY STUDIES...…15

3.1 LITERATURE SURVEY…………..…………………………………………..…15

4.0 POWER ELECTRONICS AND ELECTRIC GRID RESILIENCE……………...……..19

4.1 INVERTER CHARACTERISTIC FOR THE TEST SYSTEM……………….…….21

4.1.1 Harmonic Injection……………………………………………………….22

4.1.2 Frequency-watt compensation………………………………..………23

4.2 CONTROL ARCHITECTURE AND PROTECTION SCHEME FOR ONLINE INVERTER…..…………………………………………..……………………..24

4.3 EXPERIEMTAL DETERMINATION OF PV INVERTER RESPONSE TO GRID PHASE SHIFT EVENTS……………………………………………………………….31

4.3.1 PV Inverter Modelling and Grid Synchronization………………………..32

4.3.2 Simulation Methods and Results…………………………………………37

4.3.3 Experimental Methods and Results………………………………………41

4.4 LABORATORY TESTING OF UTILITY-SCALE PV INVERTER'S OPERATIONAL RESPONSE TO GRID DISTURBANCES……………………....47

4.5 LABORATORY TESTING METHOD……………………………………………..50

4.5.1 Experimental Results………………………………………………………56

4.5.2 Results and Discussions……………………………………………………59

4.6 PROPOSED STATE CONTROLLER……………………………………………61

4.6.1 Analysis of the Microgrid Controllable Resilience during Extreme Events……65

4.6.2 Case Study: 2008 Hurricane Ike in the Matagorda Area of Texas………67

4.7 ONLINE IMPLEMENTATION OF COORDINATIVE REAL-TIME SUB TRANSMISSION VOLT-VAR CONTROL (CREST-VCT) UNDER HIGH PHOTOVOLTAIC PENETRATION……………………………………………..69

4.8 HIL SETUP AND TEST SYSTEM…………………………………………..…71

4.8.1 Modified IEEE 118-bus test system……………………………………...72

4.8.2 Simulation in ePHASORsim……………………………………………..73

4.8.3 Input Signals……………………………………………………………...75

4.8.4 Demonstration and Results………………………………………………76

5.0 SIMULATIONS FOR SYSTEM STABILITY AND RESILIENCE…………….………79

5.1 RESULTS AND DISCUSSIONS……………………………..……………….………..87

6.0 CONCLUSION…………………………...……………………………...………........98

APPENDIX………...………….……………………………………………………….....100

BIBLIOGRAPHY…………………………………………………………………….….102

LIST OF TABLES

Table I. Parameters of the solar PV and inverter…………………………………..…………..…21

Table II. Parameters of the experimental PV inverter and the grid simulator……………..…..…42

Table III. Summary of PV inverter response to all tested scenarios…………………………….59

Table IV. Table of resilience values, uptime and downtime……………..………..…….………69

LIST OF FIGURES

Figure 1. A typical microgrid with local loads……………………………………………………..…3

Figure 2. Downed pole after the 2017 Hurricane Maria in Puerto Rico………………………………..…11

Figure 3. Damage to high voltage towers in the Southern part of Puerto Rico………….................…..…11

Figure 4. Graph of resilience versus time during natural disasters……………...………….……………14

Figure 5. Schematic of the proposed method…………………………………………….…………..24

Figure 6. Feedback control loop for the PV inverter system……………………………………..…..25

Figure 7. Flow chart for the start detection mechanism………………………………….……………27

Figure 8. The action of the proposed controller in the test circuit………………………………………..28

Figure 9. Graph of voltage (top) and current (bottom) on phase c under normal operating condition…………………………………………………………………………...………29

Figure 10. Graph of voltage on phase c versus time under fault conditions…………..…………..………29

Figure 11. Graph of current on phase c versus time under fault conditions…………………....………30

Figure 12. Graph of current on phase c versus time (controlled)………………...……………..………30

Figure 13. Block diagram of the PLL………………………………………………………………35

Figure 14. PV inverter model………………………………………………………………………39

Figure 15. Three-phase voltages, V_a,V_b, V_c, when the phase shift is 15°………………………………..39

Figure 16. Three-phase currents, I_a,I_b, I_c, when the phase shift is 15^0…………………………………40

Figure 17. Three-phase voltages, V_a,V_b, V_c, when the phase shift is 30°………………………………..40

Figure 18. Three-phase currents, I_a,I_b, I_c, when the phase shift is 30°……………………………….40

Figure 19. Three-phase voltages, V_a,V_b, V_c, when the phase shift is 60°……………………………..…41

Figure 20. Three-phase currents, I_a,I_b, I_c, when the phase shift is 60°……………………………...…..41

Figure 21. A view of the laboratory experimental set-up……………………………………………..43

Figure 22. Three-phase voltages and currents at zero phase shift……………………………………...44

Figure 23. Three phase voltages and currents when phase shift is 15°……………………………………..45

Figure 24. Three phase voltages and currents when phase shift is 30°……………………………………..45

Figure 25. Three phase voltages and currents when phase shift is 60°…………………………………..…46

Figure 26. Grid disturbance three-phase voltage waveforms used for testing and representing different types and durations of characteristic faulted system conditions…………………………………………………….52

Figure 27. Frequency and time envelopes of frequency ride-through capabilities for Distribution and Transmission protective settings…………………………………………………………………………..53

Figure 28. Diagram of the experimental setup of the 500 kW PV inverter under test including OpalRT operating as a signal generator and an oscilloscope for data capture……………………………………….55

Figure 29. Grid reference voltages and simulated grid voltages produced during the phase-to-phase fault scenario…………………………………………………………………………………………………56

Figure 30. PV inverter response to characteristic distribution-level grid disturbance (slow clearing of fault) with Distribution frequency ride-through settings……………………………………………..………..57

Figure 31. PV inverter response to characteristic transmission-level grid disturbance (fast clearing of fault) with Transmission frequency ride-through settings……………………………………………………..58

Figure 32. PV inverter response to characteristic transmission-level phase-to-phase fault disturbance (fast clearing of fault) with Transmission frequency ride-through settings…………………………………...58

Figure 33. Hierarchical control architecture…………………………………………..…………………..…65

Figure 34. Resilience curve with and without the state controller during extreme events……………......68

Figure 35. CReST-VCT control architecture……………………………………………………………...72

Figure 36. Framework for HIL integration………………………………………………………………..73

Figure 37. Data exchange…………………………...……………………………………………………..75

Figure 38. Bus voltages at *time* = 50*s* from GAMS-only and Opal with controller simulation……………..77

Figure 39. Specific bus voltages from GAMS-only and Opal with controller simulation…………………78

Figure 40. Closed-loop control system…………………………………………………………..…..……81

Figure 41. Open-loop simulation model in MATLAB/Simulink……………………………………….…...….82

Figure 42. Graph of system frequency versus time under a light load of 0.6 MW………………….…..…...83

Figure 43. Graph of system frequency versus time under a very light load of 10 kW……………….........83

Figure 44. Graph of system frequency versus time when the load is increased to 2 MW..........................84

Figure 45. Graph of output electrical power versus time when load = 2 MW……………………......……84

Figure 46. Graph of torque versus time when load = 2 MW…………………………………........……85

Figure 47. Turbine output power versus speed characteristic………………………………......…..….85

Figure 48. Graph of power output versus time when wind speed = 12m/s.....................................………86

Figure 49. Graph of power output versus time when wind speed =15m/s……………………......……...86

Figure 50. Graph of power output versus time when wind speed = 20m/s……………………...…..…….86

Figure 51. Closed - loop system of the model in MATLAB/Simulink………………………….…….....…87

Figure 52. Graph of system frequency versus time when H = 5s…………………………………..……..88

Figure 53. Graph of mechanical torque versus time when H= 5s……………………….….…..………88

Figure 54. Graph of mechanical power versus time when H = 5s…………………………..…...……..88

Figure 55. Graph of system frequency versus time when H =2s……………………………..….…..………89

Figure 56. Graph of mechanical torque versus time when H= 2s…………………….……………...……89

Figure 57. Graph of mechanical power versus time when H = 2s……………………………..….………89

Figure 58. Graph of system frequency versus time when H= 1.5s……………………….….…..………..90

Figure 59. Graph of mechanical torque versus time when H = 1.5s……………...…………...…………90

Figure 60. Graph of torque versus mechanical power when H = 1.5s……………………..…….….……..90

Figure 61. Graph of system frequency versus time when H =1.0s…………………………..…………91

Figure 62. Graph of mechanical torque versus time when H = 1.0s………………………..…….…….…91

Figure 63. Graph of mechanical power versus time when H = 1.0s.............……………………..…..…..91

Figure 64. Graph of system frequency versus time when H = 0.5s………………..…………..……....92

Figure 65. Graph of mechanical torque versus time when H = 0.5s……………….…………..…...…..92

Figure 66. Graph of mechanical power versus time when H = 0.5s……………….…………..…....…92

Figure 67. Graph of system frequency versus time when H = 0.3s……………………………..……...93

Figure 68. Graph of mechanical torque versus time when H = 0.3s…………………………...…...…..93

Figure 69. Graph of mechanical power versus time when H = 0.3s…………………..……………..…..93

Figure 70. System architecture with varying load and different wind conditions……….……………......95

Figure 71. Graph of system frequency versus time using a state controller……………………..……..96

Figure 72. Graph of direct (red) and quadrature (green) axis voltage……………………..…………...96

ACKNOWLEDGEMENT

My utmost gratitude goes to the Almighty, the God of all knowledge and existence for directing the affairs of my life thus far. I cannot forget to thank my loving mother, Mrs. Abosede Maria Aworo for giving me a legacy, a rare one through her motivation to providing me the basic education and foundation required to proceed forward in my education to the attainment of a rewarding career. All thanks to my sister, Mrs. Bunmi Afolabi and my entire family.

My sincere appreciation to Professor Thomas McDermott for setting my feet on ground from the start of my Ph.D. program, his motivation, support, encouragement and great attitude to me has been beneficial to me in my entire career. I would like to also thank my supervisor, Professor Alexis Kwasinski for his guide and supervision through the course of my Ph.D. I am also grateful to friends, colleagues whom have been supportive in a team, working together to unlocking solutions to modern challenges in electric power systems particularly to Dr. Barry Mather at the National Renewable Energy Laboratory (NREL), Golden, CO, USA and the entire Electricity Infrastructure Group (Analytics) at the Pacific Northwest National Laboratory (PNNL), Richland, Washington, USA. Special thanks to all the committee members who had also taken precious time and effort to be part of this feat.

Finally, I would like to appreciate everyone who has come to this citadel of learning to acquire or contribute knowledge with the aim of making the world a better and safer place.

GLOSSARY

E_{ss}	Amount of necessary energy storage
$E_{\mu G}$	Consumed electrical energy in the time interval under consideration
Δf_{max}	Maximum allowed frequency excursion
$H_{gen,i}$	Microgrid inertia constant
H	Inertia constant
J	Moment of inertia
T_U	Time when the battery is receiving the necessary power from the grid
T_D	Time when the load is not receiving power from the microgrid
T_{bank}	Battery bank capacity based on the autonomy it provides to its load
ρ_L	Local resilience
ρ_B	Baseline resilience
μ	Inverse of the downtime
τ_m	Mechanical torque
τ_e	Electrical or load torque
ω_s	Grid supply frequency in rad/s
ω_r	Rotor angular speed
s	Slip
R_s	Stator resistance
L_s	Stator inductance
R'_r	Referred rotor resistance
L'_r	Referred rotor inductance
L_m	Mutual Inductance

V_c	Capacitor voltage
V_o	Capacitor nominal voltage
$V_{s(\alpha\beta)}$	Time varying stator voltage space vector in the αβ frame
$V_{r(\alpha\beta)}$	Time varying rotor voltage space vector in the αβ frame
$V_{sa}(t)$, $V_{sb}(t)$, $V_{sc}(t)$	Three phase voltages applied to the stator
$V_{ra}(t)$, $V_{rb}(t)$, $V_{rc}(t)$	Three phase voltages applied to the rotor

1.0 INTRODUCTION

Over the recent years, greater emphasis has been placed on the deployment of renewable energy sources on the electric power grid to combat the climate change associated with greenhouse gases from fossil fuel sources. Carbon taxation and tradeable pollution permits are economic policies that are proposed to cut emissions overall. In addition, an overall increase in the need for energy due to the world increasing population had also called for a diverse energy mix. The idea of smart grid comes into focus, in which case, various stakeholders such as consumers, utilities, regulators, policy makers, environmental groups and researchers have long embarked on technologies, policies to support a more robust, flexible, and resilient electric grid. Smart grid is an avenue to deploy some recent technologies such as net metering, dynamic pricing and electric vehicle discharge for grid support, a concept popularly known as vehicle-to-grid (V2G). These technologies would allow for consumer participation, thereby assisting the grid with peak load shaving and scheduling via demand-side management. The goal of the United States is to reach a renewable target of 30% by 2030 [1]. In certain states, rebates are given as incentives to promote the installation of solar PV. Humans can now rely more on nature for survival. The integration of renewable energy sources is a way to improving energy security, electric grid reliability and resilience. Amongst the most commonly used renewable energy technology, besides hydropower in the past few decades are wind and solar PV [2]. However, associated with these technologies are challenges emanating from satisfactory integration to the grid, voltage stability, frequency stability among others [3].

To overcome some challenges associated with the conventional (traditional) grid, modern concepts have been trying to introduce microgrids (MG). The US Department of Energy Microgrid Exchange Group defines a microgrid as “a group of interconnected loads and distributed energy resources within clearly defined electrical boundaries that act as a single controllable entity with respect to the grid [4]. Microgrids can either be in an islanding mode or grid-connected. An example of an MG system with local loads is shown in Figure 1. Traditional electric grids are fast ageing due to poor infrastructural funding and lack of proper maintenance. However, policy makers have made efforts to decentralize the electricity market, whereby making it possible to generate, distribute and consume a few kilowatts to megawatts of electricity within a few kilometers, otherwise known as microgrids. This allows for effective utilization of renewables whose resource locations are usually far from the demand location whereby requiring a long-distance transport of energy. While the traditional power grid is more prone to failure and blackouts arising from damage, MGs would on the other hand, enhance overall system reliability and resilience. Resilience is the ability to prevent, adapt, withstand, and recover during low-probability high impact events. It is therefore, very important to make the grid more resistant for it to counter the effects of extreme events such as natural disasters or deliberate attack. In such situations, MGs may be required to operate in islanded mode so that they could supply their local load.

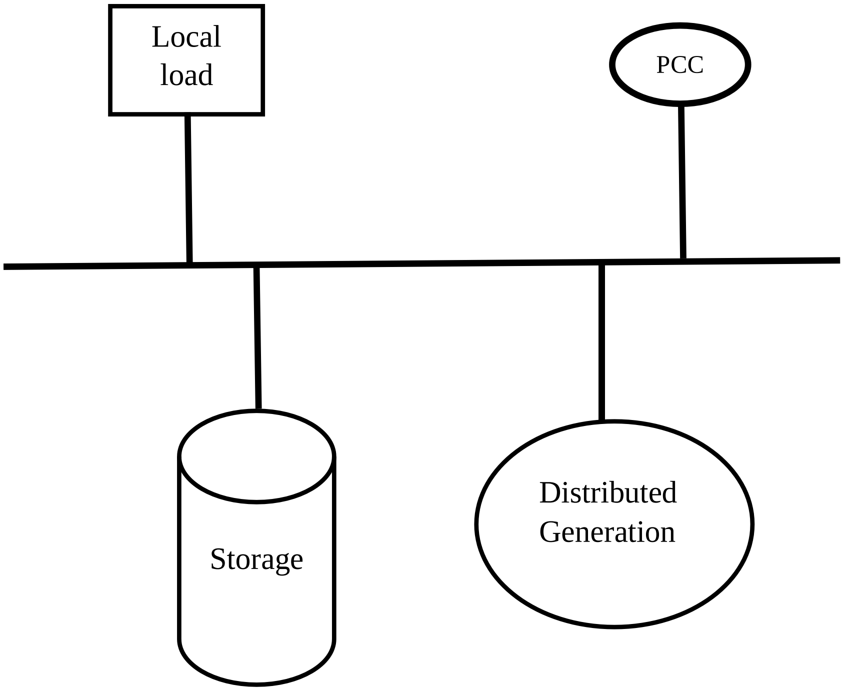

Figure 1. A typical microgrid with local loads.

1.1 STATEMENT OF PROBLEM

In recent years, there have been growing concerns on the impact of extreme weather conditions such as hurricanes, blizzard and earthquake on power system infrastructure [5]. Hence, the need for resilient power system to combat power outages and blackouts [5]. Microgrids have been considered as the promising method of improving resilience in islanded mode or in a networked topology. Typically, a microgrid consists of a point of common coupling (PCC), distributed generation (DG), energy storage and local load.

Microgrids allowed the deployment of distribution generation (DG) sources such as wind, solar, microturbines, fuel cells. It should however be noted that renewables such as wind and solar are partially stochastic in a real-time grid, coupled with an unpredictable load demand that changes abruptly. One of the purposes of the electrical engineer is to ensure that the electric grid frequency is maintained at a constant nominal frequency, say 60 Hz in the case of the United States power grid. However, changes in load demand and variation in wind speeds in the case of wind turbines may fluctuate the electrical grid frequency. These fluctuations could cause instability in the system and hence could lead to a shut down if the frequency goes below or beyond a certain limit. This thesis focuses on the resilience of the microgrid during adverse weather conditions or natural disasters while exploring the use of microgrids and energy storage.

Wind turbines have a low inertia with a characteristic low frequency response rate during load changes. An aggregate of these type of machines implies a system with very low inertia and hence stability issues could arise during transients and steady state. In this work, the effect of inertia constant (or inertia) on the transient stability of the system was investigated. The output mechanical torque and the output power was also plotted against time. Because power imbalances are one of the major issues with microgrids, then the frequency response of the system was also studied under varying load conditions. The load demand, P_D was varied near and far from the power supply, P_G. This study also employed battery energy storage (BES) or ultracapacitors as a method to mitigate the factors that could contribute to low resilience.

Renewables such as wind is intermittent and as such, rated wind speeds are not guaranteed for rated power at all times. The use of DFIG in wind turbines also serves a very great advantage since the rotor can operate within certain speed limits asides the higher efficiency. For most wind turbines in practice, the cut-in speed mainly due to low wind speeds is usually about 3 m/s while the cut-off speed due to heavy wind speed (due to tornadoes, hurricanes) is usually about 24 m/s. The rated speed for most practical wind turbines is 12-23 m/s, however an averaged constant wind speed of 20 m/s has been assumed for this application.

1.2 SCOPE OF WORK

Every complete electrical power system requires generation, transmission, and distribution to ensure the transport of energy from generation sources to demand centers where they would be utilized. Key sectors of an economy such as transportation, buildings, manufacturing (energy intensive iron & steel industry) and households with manufacturing taking a very large part of the electricity consumption [6] are very energy intensive. Furthermore, with the large influx and possible policies favoring the electric vehicles, a possible power demand surge is likely on the electrical grid. However, some technologies are being proposed to allow for vehicle-to-grid (V2G) applications [7] with the intent of reducing the load demand on the grid. The question is now, who benefits? Who pays? MGs essentially have been able to remove the barrier and provided a good answer of what we aim to achieve using V2G. Energy efficiency policy has been embraced to promote the use of energy efficient products in buildings and a public sensitization that addresses how the human social life can affect carbon footprints had all proven less effective.

An ac microgrid was considered using a wind turbine in chapter 5. The generation part of this system is a 1.5 MWA wind generator, the distribution line is a 0.5km long resistive line and the load is determined according to the simulation. There is a transformer between the transmission line and the load that performs the function of stepping down the voltage from 1 kV to 208 V.

We want to ensure that the frequency of the system follows the power profile and that when the power load demand is higher than the power generated, the frequency drops below 60 Hz. Alternatively, if the power load demand is higher than the power generated, the frequency would rise above 60 Hz. The frequency is expected to be exactly 60 Hz when the power generated matches the power load demand. Below in equation (1) and (2) is a mathematical description of what is observed on the grid. In a dc microgrid, the dc voltage is also expected to be at 1.0 p.u. Hence, a state controller is used to achieve this purpose.

$$P_G > P_L;\ f_s > 60\text{ Hz} \tag{1}$$

$$P_G < P_L;\ f_s < 60\text{ Hz} \tag{2}$$

where P_G is the power generated in MW; P_L is the load power demand in MW and f_s is the system frequency = 60 Hz.

However, we aim to develop a control technique such that the generator power output follows the load as given in equation (3).

$$P_G - P_L \rightarrow 0 \tag{3}$$

Equation (3) implies that the load always tries as much as possible to match the generation such that the difference in power is very near zero.

1.3 AIMS & OBJECTIVES

The aim of this dissertation is to achieve the following:

- Ensure that a working microgrid model is achieved using wind energy and solar PV as the renewable energy source.
- To ensure that the system output frequency varies as expected per varying load demands for ac grids.
- To ensure to show the dependency of wind turbines power output on wind speeds.
- To show that a low inertia is responsible for slow frequency response rate, frequency instability and transients in wind turbines.
- To develop a control mechanism to stabilize the system frequency irrespective of the wind speed and load variations. Also stabilizes voltage for dc microgrid.
- To finally achieve a working and resilient microgrid whose resilience is improved using a state controller.

1.4 CONTRIBUTION

This dissertation proposes a state controller, which examines the state of the system and hence determine the level of real and reactive power that is needed to keep the system frequency and voltage within the limits of operation. In such way, the stability and resilience of the system is enhanced during extreme events. A detailed analysis of this dissertation explains how the state controller is used to quantify resilience improvement. Several sections of this dissertation described in detail both analytically and experimentally on how the controller interacts with the different power system components such as the PV inverter and energy storage systems to ensure that the power system maintains a stable and resilient systems conditions during natural disasters. Chapter 4 explains how the PV inverter system can play a key role in maintaining system operation during natural disaster. Some of these approaches are not limited to fault detection strategy during such events, characteristic inverter responses during voltage phase shift events and online reactive power control in real-time.

1.5 OUTLINE OF THE DISSERTATION

Chapter 1 explains the introduction and the motivation for investigating the challenges associated with renewable energy deployment in microgrids including wind and solar PV.

Chapter 2 explains details on previous papers, literatures, existing technologies, resilience metrics and reasons why resilience is very important to the power system.

Chapter 3 shows the detailed explanation of the power system transient studies and their impact on system resilience and stability

Chapter 4 details the impact of power electronic interfaces in improving power system resilience.

Chapter 5 shows the results, graphs, voltage and frequency set points and the interpretation of the results achieved for simulation of the system stability during impacts.

Chapter 6 presents a concise conclusion of the dissertation work.

2.0 RESILIENCE AND RESILIENCE METRICS

This chapter discusses the definition, the origin of the word ’resilience’ and why it has become a very important policy subject and an important part of our lives. Resilience index is also discussed in detail.

2.1 RESILIENCE

Crawford Holling first defined resilience in 1973 as a measure of “*the persistence of systems and of their ability to absorb change and disturbance and still maintain the same relationships between populations or state variables.”* [8]. The word resilience was derived from the Latin word “resilíre” meaning “to leap back”. Considering the impacts of natural disasters on power system stability, reliability, and availability, it has become very important to study the resilience of power systems, as such topic had recently gained attention in both research and policy framework. According to the U.S. Presidential Policy Directive 21 (PPD-21), the term "*resilience*" means “*the ability to prepare for and adapt to changing conditions and withstand and recover rapidly from disruptions such as deliberate attacks, accidents, or naturally occurring threats or incidents*” [9]. Hence, in the context of power systems, resilience can be modelled in part as a function of the recovery speed of power system infrastructure after an extreme event.

2.1.1 Recent impacts of natural disasters

As there are growing concerns on the impact of climate change and their debilitating impact on the planet including the environment, the effects of the natural disasters on human survival remains largely striking, and particularly the damage caused on power system infrastructure. Aside the expected condition of power losses, and prolonged blackouts, including costs that are estimated in billions of dollars [4]. Human lives are further threatened when there is no power supply to critical infrastructures such as hospitals, water facilities and data centers. About a hundred deaths resulted from Hurricane Irma and it was recently recorded that over 3000 people have died from Hurricane Maria when it struck the islands of Puerto Rico in 2017 [10]. Hurricane Maria resulted in a total power loss (total blackout and low resilience) in Puerto Rico. Not only medical centers were affected and rendered inefficient; communication, water, traffic and road infrastructures are also in disarray. This further emphasizes the dependence of life supporting infrastructures on the stability, availability and resilient power system.

In 2018, Hurricane Florence hit the coasts of North Carolina, South Carolina and Virginia leading to loss of power to several thousands of people. It is not new that the most vulnerable parts are the distribution lines, electric poles, and other facilities that transport energy to customers. It was reported that a solar PV installation remained unscathed during this hurricane, whereby vindicating the assertion that renewables and decentralized systems (microgrids) boost power system resilience. There are other natural disasters that can affect the power system such as earthquake, tornadoes, wildfire and floods; however, hurricane event had gained wider attention because of its frequency of occurrence and the degree of impact on the U.S. coasts. It should be noted that hurricane and flood may be simultaneous events. Figures 2 and 3 show the damages to some power system infrastructures after an extreme event, specifically the 2017 Hurricane Maria in Puerto Rico.

Figure 2. Downed pole after the 2017 Hurricane Maria in Puerto Rico. (© Alexis Kwasinski, used with permission)

Figure 3. Damage to high voltage towers in the Southern part of Puerto Rico. (© Alexis Kwasinski, used with permission)

2.1.2 Resilience metric

Due to a known fact that we may not be able to stop extreme events from happening, we can thus reduce its impact on the power system by integrating the state controller. While most power system planners focused more on systems that can withstand extreme events, the ability to quickly recover the power system after natural disasters is an important component that should be extracted for detailed discussion. Beyond the recovery speed is also the ability to bring the system back to near the pre-event level. Several resilience indices have been proposed to ascertain resilience level before, during and after an extreme event, but the underlying principle is the ability of the system to supply a given load during a specified time interval. Hence, resilience can be computed in terms of the uptime and downtime of the system [11], as defined by equations (4) and (5):

$$\rho_L = 1 - (1 - \rho_B)e^{-\mu T_{bank}} \tag{4}$$

$$\rho_B = \frac{T_U}{T_{U+} T_D} \tag{5}$$

where ρ_L is the local resilience, ρ_B is the base resilience, μ is the inverse of the power supply downtime T_D, and T_{bank} is the battery bank capacity, T_U is the time when the load is receiving power and T_D is the time when the load is not receiving power. For N loads resilience is calculated as:

$$\rho_B = \frac{\sum_{i=1}^{N} T_{U,\,i}}{\sum_{i=1}^{N}(T_{U,\,i} \; + \; T_{D,\,i})} \tag{6}$$

This metric for resilience is analogous to that of availability [12]. However, while resiliency deals with only one failure and repair cycle, availability applies to an infinite number of such cycles. Resilience is not to be equally confused with reliability because reliability in its strict sense does not consider repairs and because it assumes normal standard operating conditions.

Furthermore, resilience involves the adaptation to an anticipatory high impact, low-probability event, and the ability to quickly recover to its pre-event restorative phase and a learning of the event to prevent or more properly manage future recurrence. This adaptation process can be related to the general control system concept of feedback in which sensing over a system output signal is used to adjust system variables in order to achieve a given objective.

However, a non-linear state controller has been adopted in this approach to increase the operational resilience by reducing the downtimes associated with a V-shaped region as in Figure 4, which approximates a triangular shape observed when plotting the resilience metric vs. time. A power system maintains a certain level of resilience in the pre-event phase before experiencing a disturbance from a natural disaster, and when such extreme event happens, the power system experiences a sharp decline in performance into the degradation phase, the degradation can take a very short period of time if the power system is adequately planned for such conditions, depending on the speed of recovery and alternate power supplies; the performance begins to increase into the restoration phase when repairs and alternative source of power delivery to the load might have been initiated. Finally, the post-restoration phase is when the system is fully back into normal operation, but potentially lower than the amount of load that came back online. This V-shaped, indicates the most likely shape of the resilience curve that is normally obtained during the degradation and restoration phases of the power system. In [13][14], enabling resilience of complex engineered systems using control theory was proposed, but without proven details expressing the relationship between the controller and resilience metric. There have not been enough known efforts to quantify resilience with the state controller approach due to the multi-dimensional nature of resilience. However, this dissertation shows how a state controller can be used to increase resilience by quantifying the system metrics, and how it maintains the system operating during the period of disturbance. It is possible then to refer to an operational resilience, which relates to “intelligent” control-based actions taken to provide the assets with control capability and resources to effectively withstand disturbances as it unfolds [15]. The application of the proposed controller in reducing the downtime and the area of the V-shape is further discussed in detail in Chapter 4. It can be easily observed from Figure 4 that the post-restoration resilience level was not restored to the exact level at the pre-event phase, which is what is obtainable in a real- life scenario.

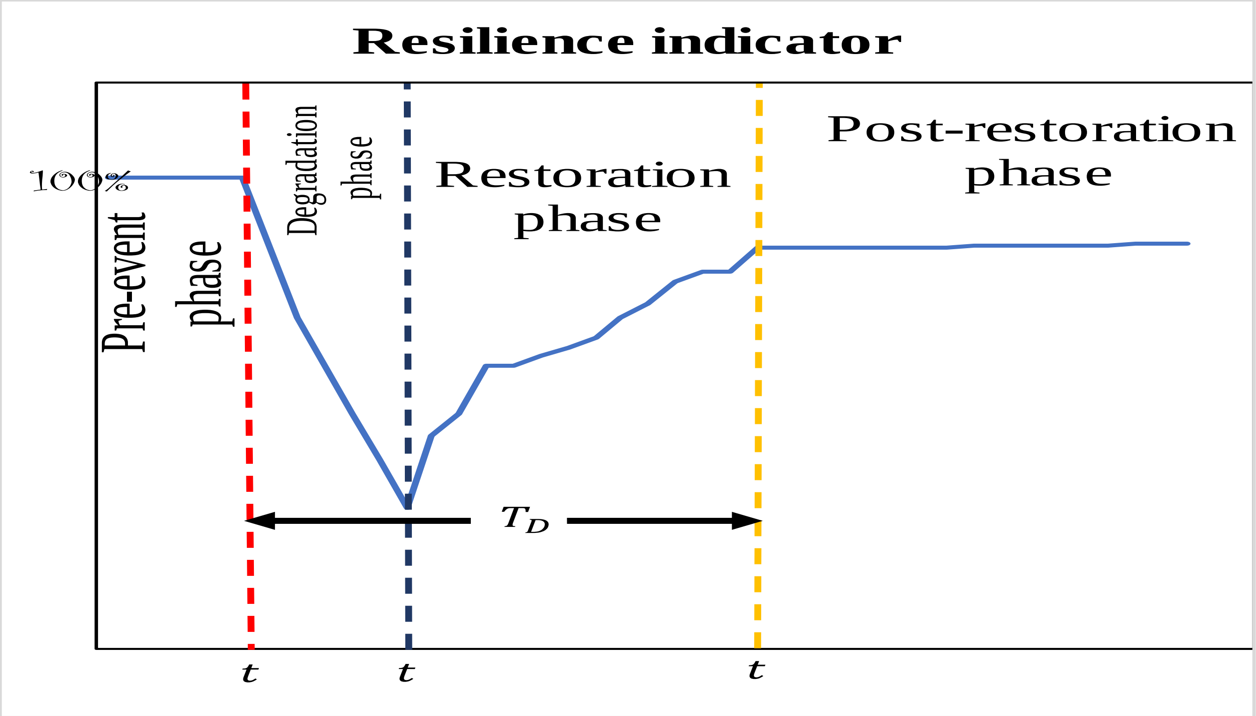

Figure 4. Graph of resilience versus time during natural disasters.

3.0 RENEWABLE ENERGY SOURCES AND TRANSIENT STABILITY STUDIES

Due to the recent interest in the integration of distributed energy resources (DER), there has been a significant change to the modelling and operation of power systems. Distributed energy resources constitute components whose behavior and responses can pose a significant change to the power system control. This chapter explores wind energy conversion and then discusses how the stability of the power system is affected by factors such as inertia typically a low value for wind energy systems, which is an input to be expected in the future when renewable penetration becomes enormous on the electrical grid.

3.1 LITERATURE SURVEY

Power infrastructures are readily subjected to system disturbances such as fault. Faults in power systems are low-impact high probability events; these can be described in terms of reliability. However, a difference between resilience and reliability is the fact that resilience is related to high – impact low probability events such as hurricanes, earthquakes and tornadoes. Hence, the adaptability and survivability of the system under these strenuous conditions is very important.

Microgrids have several issues ranging from power imbalance, frequency stability, voltage stability and protection coordination, which are contemporary challenges facing the deployment of renewables such as wind and solar [16]. However, MGs are very important aspect of the future power systems and smart grid. They are very essential to counter the blackout scenario due to cascade effects during natural disasters as investigated in [17]-[19]. Method of corrective actions and protection studies during cascading events due to extreme events are proposed in [20]-[21]. This method aims to reduce cascading failures that characterizes extreme events. It is important to note that resilience in microgrids depends on lifelines, hence, the lifeline dependencies of grid infrastructures on microgrid resiliency were investigated in [22], which detailed how resilience metric could be improved by the combination of diverse energy sources and energy storage during natural disasters. Irrespective of the attempt to maintain an acceptable level of system resilience for system survival and recovery during natural disasters, load balancing remains a key technique for keeping the system in a stable operating condition, as proposed in [23], where maximum power coefficient tracking method was deployed for such purpose and to further research into a more in-depth load balancing control with the aid of power electronic interface, a frequency trimming control strategy was proposed in [24]. This method involves the use of the control variables of the converter to realize demand-supply balance. However, this work aims to use energy storage as a reserve to prevent the shutdown of the ac microgrid during the low frequency response rate because of low system inertia whereby enhancing the system resilience and availability. [25] presents a framework for analyzing the resilience of an electric power grid with integrated microgrids under extreme conditions. It developed a concise framework for power system resilience analysis with networked microgrids whereas a cluster of microgrids was presented in [26], it proposes and energy management scheme that improves scalability and flexibility through decentralized control and co-ordination of microgrids. During natural disasters, some critical loads are necessary to be served. Hence, a service restoration model was proposed in [27], which puts into consideration, the stochastic energy variations arising from renewable sources in microgrids.

The role of microgrid in enhancing the resilience of the traditional power grid was previously examined in [4] and to this extent, we can be very convinced about the importance of microgrid to power system resilience. In [28], a predictive control-based algorithm was proposed to improve a power systems resilience through hierarchical outage management. In this method, the entire smart grid was considered as a system of multi-microgrids with distributed optimization and control. The optimal placement of microgrids in a power system for improving resilience was developed in [29] where a mixed-integer linear programming (MILP) program was formulated to account for multiple component outages and limited investment budget. An hourly-scheme was proposed to improve resiliency in [30]. This method exploits the market pricing capability of a microgrid for improving resilience. A resilience-constrained unit commitment (RCUC) was proposed in [31]. This method addresses the resiliency concerns, which are not often addressed during security-constrained unit commitment (SCUC) that most power operators rely on. However, since microgrids are fast becoming the agents of resilience improvement in the islanded mode, they become overloaded and this leads us to [32] where a self-healing strategy was proposed. The use of DGs and MGs for improving electric grid resilience with a focus on a sub-Saharan African country was reviewed in [33], this looks into a specific geographic location to validate the relevance of microgrids to the power system. The use of electric springs (ES) to enhance resiliency was proposed in [34]. This method develops a control strategy for the ES, based on a feasible operating region of the ES and the power-voltage curve of the bus connected to the ES. The voltage and frequency are then regulated to enhance the system resiliency. With the ever-increasing renewable penetration, impacts on system voltage is very much expected, hence, a research on the coordination of reactive power for voltage control due to high PV penetration was proposed in [35]-[38], whereas a Markov-based energy storage model was proposed in [39][40] for a microgrid with high wind and PV penetrations, whereby allowing us to assess the impact of energy storage on power system availability and resilience. In this dissertation, we propose the use of state controller, which updates its input parameters to regulate the system frequency and voltage at the specified operating point. This would be proven to further improve the power system resilience within the context of the microgrid.

4.0 POWER ELECTRONICS AND ELECTRIC GRID RESILIENCE

The role of power electronics in the emerging electric grid is very crucial to the stability, reliability, availability and resilience of the power system. In this section, emphasis will be paid to the characteristics of PV inverters and how they interact with the grid. Simulations were carried out in MATLAB/Simulink to explore the potential capabilities of inverter control in improving resilience during fault conditions.

In recent years, increasing attention have been paid to the protection coordination of PV inverters, owing to the large role it plays in the integration of renewables to the grid. According to IEEE 1547 standard, a PV inverter must disconnect from the grid within 2s of a fault [41]. This condition known as islanding is sought to protect the PV inverter and ensure safety, which is not guaranteed with a grid-tie solar PV. As renewable energy penetration increases, the adoption of power electronic interfaces also increases while this brings into question the behavioral studies of such devices during fault conditions. Not only are they considered for grid-tie applications, dc-dc bi-directional converters are also deployed in [42], for vehicle-to-grid application in electric vehicles. An in-depth study of power electronics models and how they can support the power system through its control features would likely guarantee the modernized electricity grid that we aim for [43][44]. This phenomenon is not far from literature such as in [45] where the use of emerging power electronics technology for the active power management of electric power system was discussed. A concise and clear details on how advanced power electronics can be deployed for power system architecture, operation & control was explored in [46].

In conventional generators, the short-circuit currents are abnormally high and hence could easily open a circuit breaker or blow-up a fuse indicating an abnormal condition. This phenomenon is not possible with inverters due to the limiting current capabilities which have left researchers with varying questions to answer. The current control of PV inverter for three-phase unbalanced fault was investigated in [47] using Lagrange multiplier. In [47], the 2nd order harmonics and overcurrent in PV inverters during unbalanced voltage in a three-phase system was controlled using the double-loop feed-forward decoupling control with the knowledge of symmetrical components. However, this method involves the use of some weighting factors, which are gradually increased to suppress the ripples in real and reactive power under fault scenarios. An accurate estimation cannot be verified in real time and can impose considerable time constraints on the proposed method. A control strategy for three-phase grid-connected PV inverters enabling current limitation under unbalanced faults was proposed in [48]. The condition in [48] was carried out without tracking the maximum power point, which deviates from practical scenarios in which the maximum power point (MPP) may vary depending on the time of the day and other conditions. A maximum power point tracking (MPPT) scenario was however considered in [48]. An optimized active power control method of two-stage grid-connected photovoltaic inverter under unbalanced grid faults was proposed in [49]. This method optimizes the active power delivered by the inverter during a single phase-to-ground fault by defining a safe operating region (SOR). This was achieved by defining the active power oscillation limits and then comparing it to the positive- and negative- sequence voltages. However, the strategy proposed herein which was not previously considered in the current literature uses current components rather than voltage as proposed in [50], because using voltage components may limit the practicability of the system operating under varying MPP. Several other discussions on the technological advancements of solar PV were examined in [51]-[55]. In this section, a strategy which put into consideration the MPPT was proposed and it proved efficient for detecting faults in PV inverters.

4.1 INVERTER CHARACTERISTICS FOR THE TEST SYSTEM

This section details the relevance of a PV inverter fault detection to the state controller. In order to enable a resilient power system, the system must be able to handle fault conditions without jeopardizing the ultimate goal of delivering power to the load. A fault detection strategy was proposed in this section, this strategy would enable the PV inverter to disconnect very quickly during fault conditions and as such, the state controller would sense a disconnection state and then request the required amount of energy storage that should be turned on to supply the stranded load. The advantage of this method is that it reduces downtimes for the load during such conditions.

Inverters behave as current sources when connected to the grid. Inverters have a limiting current, I_{lim} or in-rush current, I_{in}. This value is about 1.5 times the rated current, I_{rated} of the inverter. The solar PV characteristics and inverter parameters are shown in Table I below.

Table I. Parameters of the solar PV and inverter.

Parameters	**Values**
Solar panel power	215 W
Number of panels	400
Solar panel Open-circuit voltage	36.3 V
Solar panel short-circuit current	7.84 A
DC-Link voltage	500 V
Filter inductance	10 mH
Switching frequency	2.1 kHz
Grid voltage	7 kV
Grid frequency	60 Hz

In normal operating conditions, little or negligible reactive power is observed in inverters, however, during fault conditions, real power tends to decrease while the reactive power increases. This explains why modern inverters are designed with voltage- and frequency ride-through capabilities [56]. Research on low voltage ride through control of PV grid-connected inverter under unbalance fault was presented in [57]. The ride-through capability of the PV inverter allows it to inject reactive currents under voltage sag [58][59]. It also enables the limiting of current to the rated value. However, the inverter might continue operation with a power quality that is acceptable. The injected harmonics might lead to poor power delivery at the load end. Hence, a protection scheme that prevents damage to customers' load is highly desirable in any power delivery system, which is why a fault detection from the PV generation side is being considered in this section.

4.1.1 Harmonic Injection

In grid-tie inverters, emphasis is placed on the total harmonic distortion (THD) that is injected into the grid. The amount of harmonics injected into the electrical grid is limited by the IEEE 519 standard [60][61]. During fault conditions, this value is expected to increase beyond the limit, whereas the power quality of the system becomes compromised. In such cases, it might be necessary to execute an offline command on the inverter controller. While high-order filters are designed to block high-frequency harmonics in such systems, it might become difficult to filter out harmonics that result near the fundamental frequency during grid faults and an alternative is to establish a protection strategy as presented in this work to prevent the injection of the current harmonics arising from the grid voltage phase shifts under fault conditions. The inverter can however, be reconnected online once the fault is cleared.

4.1.2 Frequency-watt compensation

In order to ensure stability in the grid, there must be real power balance between generation sources and the load, such that the frequency maintains a steady state or falls within an acceptable grid limit. The challenge in modern power system is the influx of distributed generation (DG), which in some cases are renewable energy sources with intermittent supply and a corresponding low inertia. Intermittent sources source such as solar only produces power during a certain time of the day when the solar irradiance is reaching the panel, on the other hand, it produces near to zero power during the night. A passing cloud during the day could also result in a transient that can adversely affect the output voltage from the solar panel. Similarly, wind turbines will not produce power up to the rated value when the wind speed is below the cut-in speed value of the turbine. It should also be noted that during extreme events such as Hurricanes, where the air-mass has an abnormally high wind speed, the wind turbines will be forced to shutdown whereby reducing the amount of possible power generation during such circumstance. The recent approach that has been considered to solve these problems is an effective energy management system (EMS) with an inclusive distributed energy storage such as batteries or ultracapacitors [62]-[64]. Batteries are not only considered to improve the power system availability [65], they also contribute to the system resilience by reducing downtimes during extreme events such as hurricanes and earthquakes [66]. In addition, grid-tie inverters are designed with the capability to perform the frequency-watt function by supplying its own real power to the grid when the frequency reduces. This concept known as frequency ride-through is performed at the expense of the inverter's reactive power. In order to conveniently address this PQ trade-off, the ride-through is instantaneously performed during fault conditions after which the inverter disconnects from the electrical grid. The high likelihood of such connect/disconnect activity on the inverter brings into question why distributed energy resources require a more adequate and detailed study. The reliability of such vital system component could reduce, and hence the need for adequate protection scheme that would prevent further damage as proposed in this section.

4.2 CONTROL ARCHITECTURE AND PROTECTION SCHEME FOR ONLINE INVERTERS

This section explains the control and protection scheme that was designed for online inverters during extreme events. Consequently, this is to enable the state controller to take a decisive action for system stability during such events. The schematic describing the fault detection method and consisting of the voltage source inverter (VSI), generator bus, load bus and nodes is shown in Figure 5.

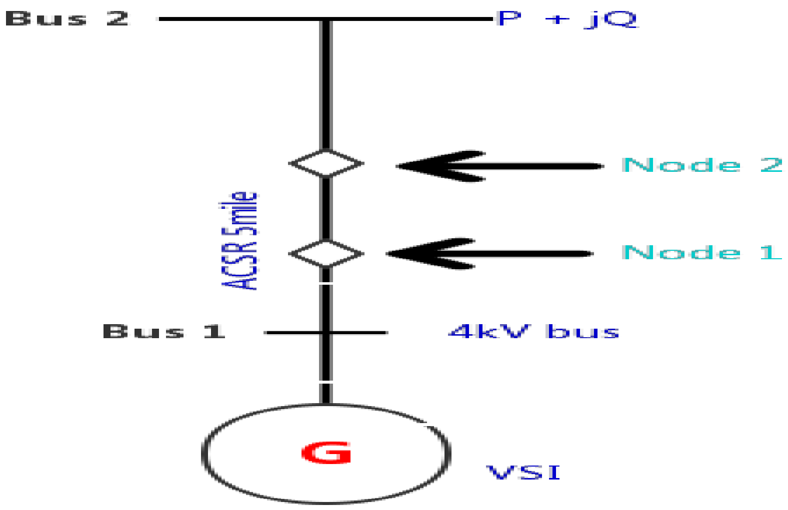

Figure 5. Schematic of the proposed method.

System state awareness is necessary to establish an effective control on the system. This control is based on a working feedback loop, which communicates with the output of the system and then establish an error difference that is used to stabilize the system. The decision made is based on the choice of operation of the designer and the implemented program. It is therefore necessary that the inverter system has some memory to recall the previous state of the system. The feedback control loop for the system and the flowchart for the control operation are given in Figures 6 & 7 respectively.

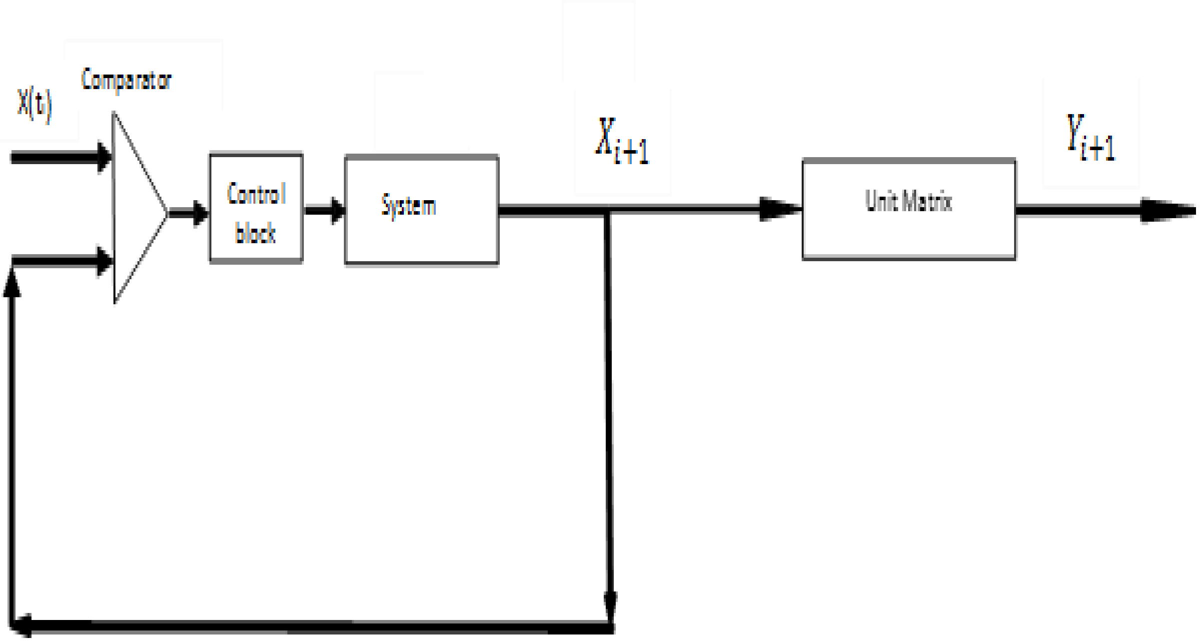

Figure 6. Feedback control loop for the PV inverter system.

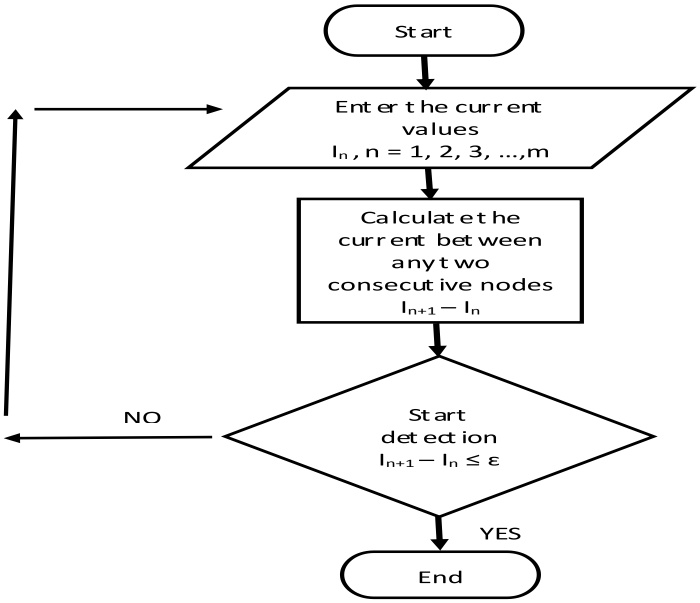

Figure 7. Flow chart for the start detection mechanism.

The algorithm for the PV inverter operation is detailed below:

1. Start program at $t_{i.}$

2. Enter the values of current at each node using the formula given in equation (23).

3. Compute the difference in values between two consecutive nodes.

$$I_n - I_{n-1}$$

4. Compare the value in step 3 to Ɛ.

5. Start detection mechanism

If $I_n - I_{n-1} > \varepsilon$

then stop inverter operation, disconnect and return to step 2.

else if $I_n - I_{n-1} < \varepsilon$

then continue inverter operation and end program until the next time step, t_{i+1}.

A PV array was synchronized to a 7kV grid via a three-phase inverter and a step-up transformer as shown in Figure 8. The simulation for the test circuit was carried out in MATLAB/Simulink and a short-circuit fault was applied on phase c, at t = 2 s. The voltage and currents signals on phase c under normal operating conditions, fault and controlled conditions are shown in Figure 8 to 11 below. The proposed strategy is then used to determine the current between different nodes as shown by the controller in the test circuit in Figure 8 to determine if there is a fault. In order to determine the presence of a fault, the three-phase currents are measured and then compared to a rated value which has been pre-set by the central controller using a relational operator. The relational operator produces a '0' output then the measured currents are less than or equal to rated value. However, it produced a "1" output if the measured value is greater or equal to the rated value. The resulting output is then used to toggle the switch to ON or OFF position, if OFF, the value is less than the rated current, if ON, it means that the measured current in any of the phase is more than the rated value and an over-current might have been established, which could then trigger a PI controller to set the current value to a tracked reference via the current limiter. Large deviations from ε indicates a fault condition and would trigger the clock-controlled switch to an OFF position, resulting from the command it received from the AND logical operator. The system remains in this '0' state until the fault is cleared for the inverter to resume operations. This protection method gives a timeframe to differentiate a fault from an increasing PV current output, hence, making it more suitable for use than the traditional protection schemes. In the performed test, once the protection scheme detects a fault condition which occurs as a short-circuit in the test case, the inverter is disconnected within 0.6 s, that is, at t = 2.6 s as shown in Figure 12. At *t* = 2.6 s, the state controller receives a signal that a disconnection has happened from a PV source and will then use this to process an output that reads the required level of energy storage needed to supply the stranded load.

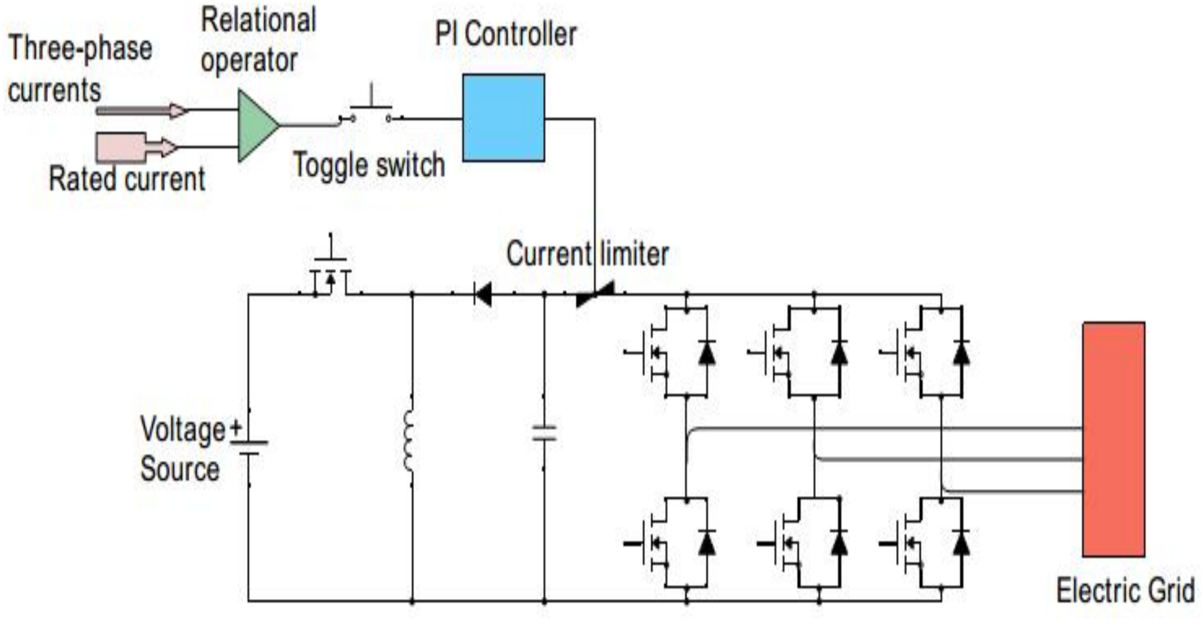

Figure 8. The action of the proposed controller in the test circuit.

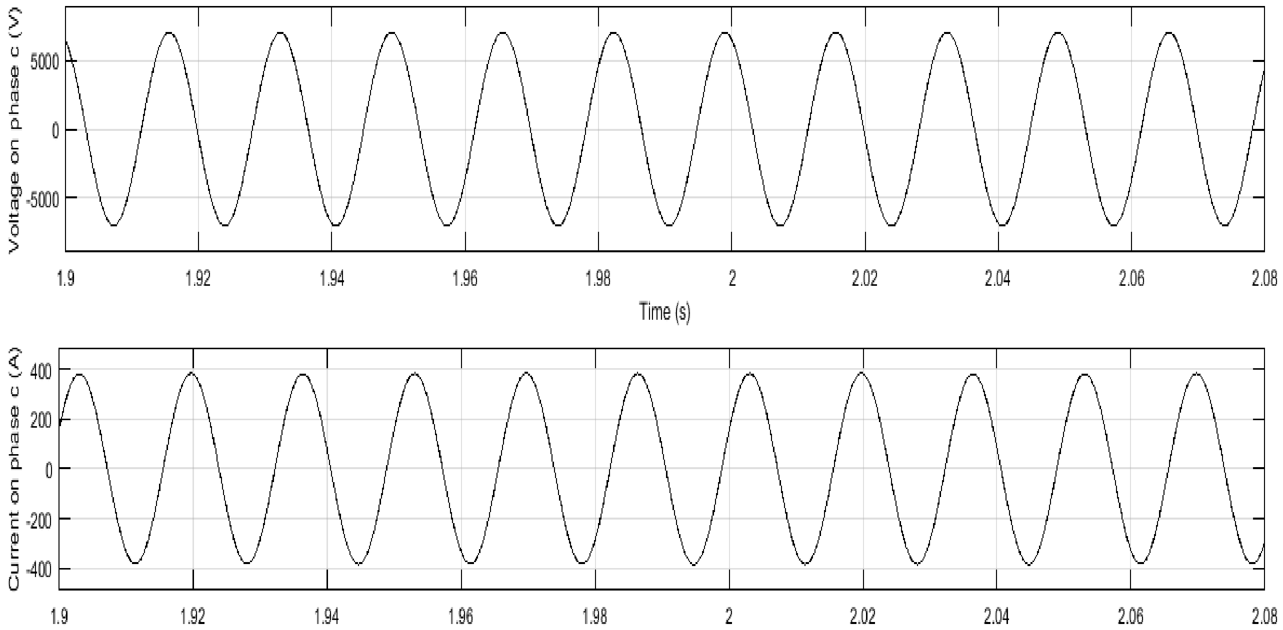

Figure 9. Graph of voltage (top) and current (bottom) on phase c under normal operating condition.

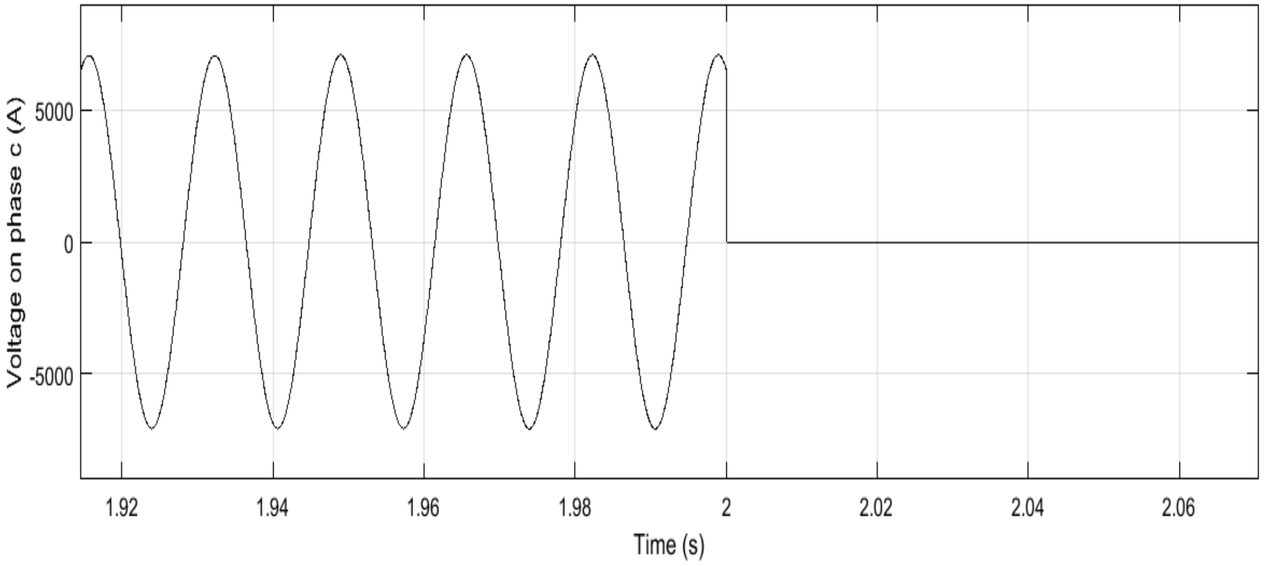

Figure 10. Graph of voltage on phase c versus time under fault conditions.

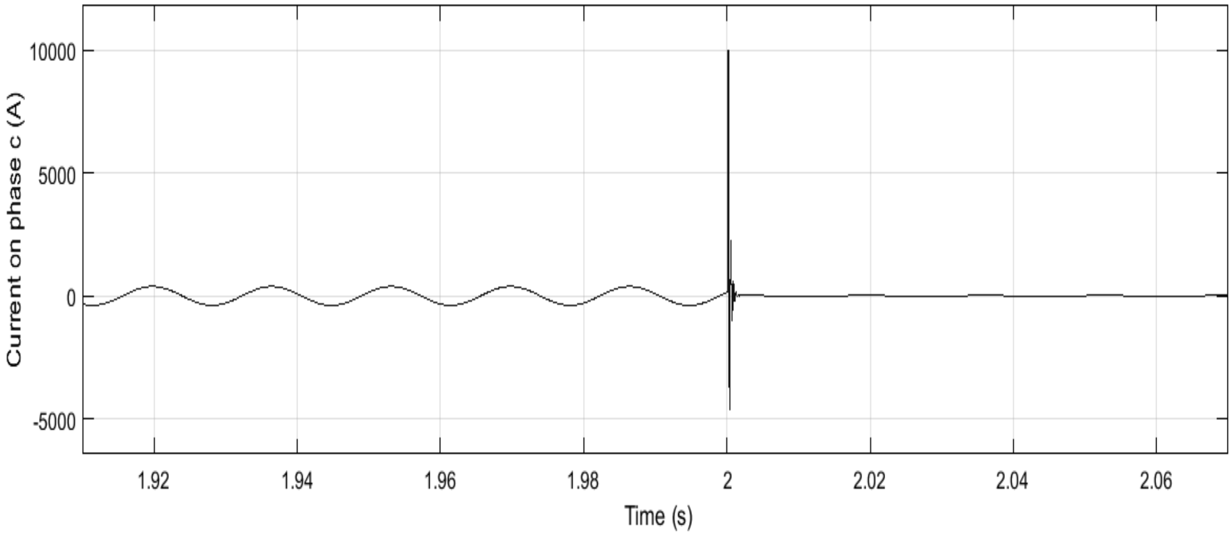

Figure 11. Graph of current on phase c versus time under fault conditions.

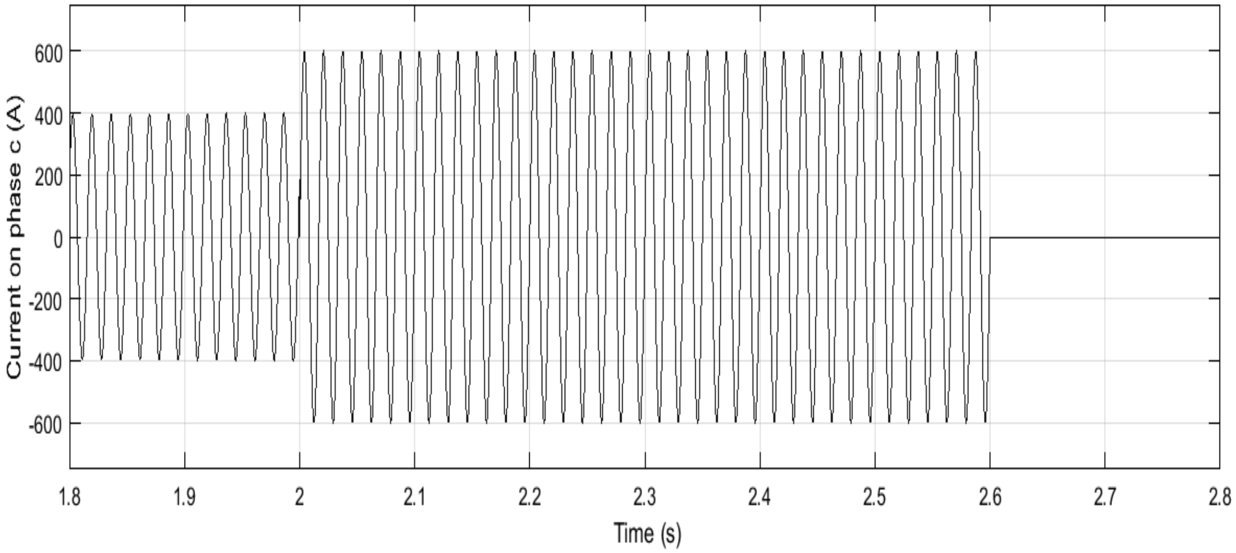

Figure 12. Graph of current on phase c versus time (controlled).

4.3 EXPERIMENTAL DETERMINATION OF PV INVERTER RESPONSE TO GRID PHASE SHIFT EVENTS

With the continued growth of renewable energy resources which interface to the electric grid via inverters, the understanding of such devices becomes ever more important to the safe and reliable operation of the bulk power system with respect to the system resilience. This section investigates the specific response of a utility-scale PV inverter to grid voltage phase shift-type disturbances which sometimes occur during grid fault events and hence use such response characteristics to design the state controller in a way to enhance power system resilience during natural disasters. The role of the PV inverter's phase-locked-loop (PLL) is identified as important to modeling the response. The PLL can also assist with making the state controller as fast as possible during its loop process. This is achieved by embedding the controller and the PLL together, which will make the controller to send a faster signal to the energy storage system so that the connected load can receive power for a certain period of time within the storage capacity and hence, reducing downtimes or outages to the load. Switching-level simulations of a utility-scale PV inverter with a modeled PLL show a characteristic response when phase shift disturbances require the PLL to track what appears as fast frequency changes that often occur during cascading failure. Additionally, in this section a full-scale laboratory testing was carried out using the Opal real time (RT) OP5142 real time simulator and a large grid simulator to create phase shift disturbances with a high degree of repeatability. A photovoltaic (PV) inverter was connected to a grid simulator, and phase shifts were instantaneously implemented on the simulated grid, the results of the currents were then obtained. The experimental results obtained were validated with simulation results obtained from MATLAB/Simulink. It goes further to prove that the adequate modelling of such vital grid component would further enhance the resilience of power systems during disturbances.

The safe and reliable integration of renewable energy sources within the bulk electricity system is becoming ever more important as such sources continue to grow substantially every year. It is widely believed that the integration of renewables such as wind and solar can enable clean and reliable energy for human use both in developed and developing regions [67]-[69] while improving the resilience of power systems as they are considered to be a distributed form of power generation.

As the amount of wind and PV energy increases in an electric grid it becomes ever more important to fully understand the expected response of such devices to abnormal voltage and frequency conditions which may be present on an electrical grid from time to time due to faults and other abnormal operating conditions that arises from system attackers such as extreme events. One existing uncertainty is how PV inverters respond to grid events whose dominating characteristic is a near instantaneous shift in the phase relationship of the grid voltages. This section focuses on the results of an investigation into exactly such responses by first developing models to understand the most important factors relating to such phase shift responses and secondly, by completing laboratory testing to see how a commercially available PV inverter actually responds to phase shift disturbances and finally to address how such responses influences the state controller.

4.3.1 PV Inverter Modelling and Grid Synchronization

PV inverters are generally represented as constant PQ generators in current bulk system-level dynamic models, but during transient fault conditions they act as power-limited current sources. In addition to fundamental differences in fault current capability compared to traditional synchronous generators, PV inverters characteristic response to abnormal conditions is a strong function of the inverter controls implemented to protect the PV inverter itself but also to safely integrate to the interconnected grid. For example, a distribution-connected PV inverter would likely implement the requirements of the IEEE 1547-2003 standard which requires a PV inverter to disconnect within 2 s of grid fault or if a utility island is created [70]. Most currently distribution-connected PV was interconnected under IEEE 1547-2003 thus the existing PV fleets response to phase shifts should be characteristic of tests completed with IEEE 1547-2003 settings. Grid-tied PV inverters also have the characteristics of tripping under grid events due to its settings. Disconnection or a dramatic reduction of real power delivered to the grid can occur during grid overvoltages and undervoltages, also during over/under frequencies [71]. As power systems experience rapidly changing frequency and voltage during faulted conditions or due to the loss or demand or generation, there is a growing expectation and additional grid requirements that a PV inverter is not expected to trip under these types of events to avoid exacerbating current bulk system contingencies and as to not reduce bulk system reliability. Hence, most PV inverters are designed to have voltage and frequency ride-through capabilities within a specified voltage and frequency range [72]. This sub-section focuses on phase shift response originates from the fact that such phase shifts impact both the measured frequency and voltage and yet are characteristic of many real world faulted operation conditions (a phase-to-phase fault for instance) Grid-tied inverters (operating as current sources) must comply with certain requirements before they can be synchronized to the grid. These are:

1. The phase of the grid-tie inverter must be the same as the grid phase.
2. The frequency of the inverter must be the same as the grid.

The response of an inverter to grid events is potentially influenced by many factors such as frequency and voltage measurement methods, inverter current limiting protection circuitry and control, dc bus voltage control, and, of course, the specific design of the inverter including the design of the output filter. Often an inverter is synchronized to the grid using a PLL. The PLL also plays an important role in frequency measurement as the oscillator inherent in a PLL would make a reliable grid frequency measurement source for supervisory functions like frequency ride-through control logic. Modeling efforts for this work have focused on accurate modeling of a PLL in the PV inverter model as to elucidate the role such circuitry/code play in PV inverters response to phase shifts.

Three-phase systems are synchronized to the grid using the PLLs. The three-phase voltage signal is transformed to two-axis d-q components using park's transformation, and the frequency, ω and phase, ϕ components are utilized as reference signals in the PLL. A phase-locked loop consists of a voltage-controlled oscillator (VCO), phase detector (PD), and a low-pass filter as shown in Figure 13.

Previous research regarding PLLs in power systems is vast but few, if any, work characterizing and modeling the PLLs response specifically for PV inverter. Still, a number of previous works show the importance of PLL design and performance for grid synchronization. PLLs have also been employed in rectifier circuits in [73], where a novel digital PLL was proposed to realize a faster convergence of the system using the ratio of d-q voltages as the parameter of interest. However, synchronous reference frame PLL (SRF-PLL) are normally being adopted for the interconnection of three-phase systems [74][75]. They were used to detect system islanding in [76] based on virtual impedance that was added to the circuit. The virtual impedance provided a sufficient frequency deviation that was needed to detect islanding when the frequency of the resonant tank matches the grid frequency. An analysis of the middle frequency resonance in doubly fed induction generator (DFIG) considering PLL was investigated in [77]. However, this section presents the characteristic response of grid-tied PLL-based PV inverters to grid disturbances using laboratory evaluation of utility scale (500 kW) hardware components. It becomes very advantageous to this dissertation because the state controller can be embedded in the PLL to enable it to detect changes in system parameters especially when the inverter loses synchronism with the grid. These properties can then be used by the state controller to request the amount of energy storage that would serve the loads that could be affected by the inverter that is about to go offline.

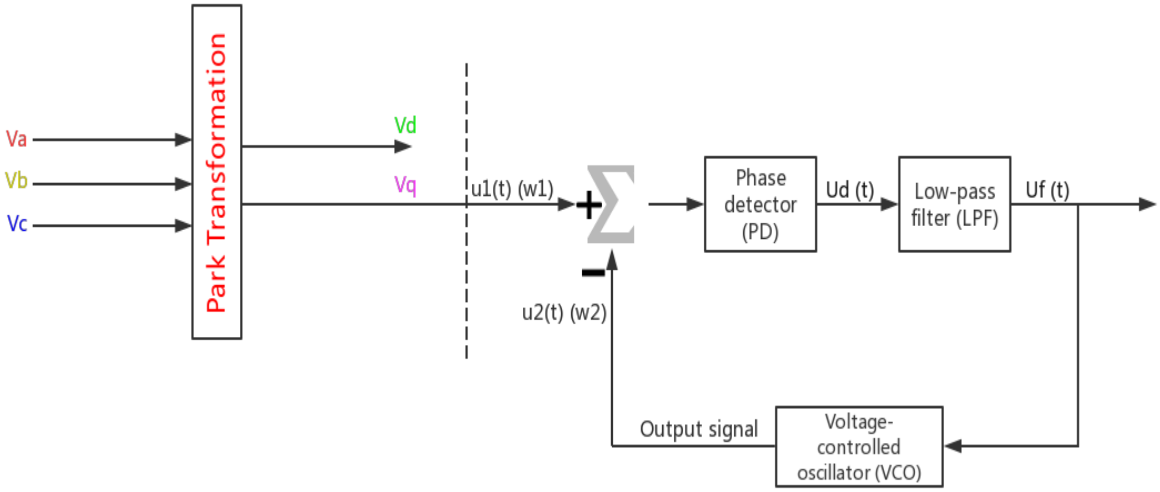

Figure 13. Block diagram of the PLL.

The output signal, U_f (shown in Figure 13), of the loop filter determines the angular frequency, ω_2, at which the VCO oscillates. The angular frequency, ω_2 is given by;

$$\omega_2\,(t) = \omega_o + K_o u_f(t) \tag{7}$$

where ω_o is the center angular frequency of the VCO and K_o is the VCO gain in rads^{-1}v^{-1}.

The output of the PD is proportional to the phase error, ϕ_e and is given as

$$u_f\ (t) = K_d \phi_e \tag{8}$$

where K_o represents the gain of the PD in V/rad.

The phase signal, ϕ_1 (t) can be a constant, linear or quadratic function of time depending on the signal at which it is excited [78].

As shown in Figure 13, the three-phase ac signals are transformed to a two-axis vector using the park transformation technique. This produced the direct-axis component, v_d and the quadrature-axis component, v_d in the form of dc quantities. The quadrature-axis component, v_q, is used as the reference signal, $u_1(t)$ with an angular frequency of $\omega_1(t)$.

The phase signals carried by the input of the PLL can be represented as;

$$u_1\ (t) = U_{10} \sin\,[\omega_1(t) + \phi_1(t)] \tag{9}$$

The output is represented as a square wave signal written as;

$$u_2\ (t) = U_{20} \sin\,[\omega_2(t) + \phi_2(t)] \tag{10}$$

where U_{10} and U_{20} are the amplitudes, ω_1 and ω_2 are the angular frequencies, ϕ_1 and ϕ_2 are the phases.

Replacing equation (11) by its Fourier series gives,

$$u_2(t) = U_{20}[\ \sin(\omega_2 t + \phi_2) + \frac{4}{3\pi}\sin(3\omega_2 t + \phi_2) + \cdots] \tag{11}$$

For the PD output, we have

$$u_d\ (\boldsymbol{t}) = u_1\ (\boldsymbol{t})\ .\ u_2\ (\boldsymbol{t}) = \ U_{10}\ U_{20}\ \sin(\omega_1\ t + \phi_1)$$
$$.\ [\frac{4}{\pi}\cos(\omega_2 t + \phi_2) + \frac{4}{3\pi}\cos 3\omega_2 t + \phi_2) + \cdots] \tag{12}$$

When the PLL is locked, the frequencies ω_1 and ω_2 are identical, and $u_d\ (\boldsymbol{t})$ becomes,

$$u_d\ (\boldsymbol{t})\ = U_{10}\ U_{20}\ [\ \frac{2}{\pi}\sin\phi_e \ldots] \tag{13}$$

The higher order terms have been filtered out.

By setting $K_d\ = \frac{2U_{10}\ U_{20}}{\pi}$

$$u_d\ (\boldsymbol{t}) \approx\ K_d\ \sin\ \phi_e \tag{14}$$

When the phase error is very small, the sine function can be replaced by its argument, and we have

$$u_d\ (\boldsymbol{t}) \approx K_d\ \phi_e \tag{15}$$

This equation represents the linearized model of the phase detector. The above equations were used to design a PLL for simulation of a three-phase PV inverter. The phase detector output of equation (15) can then form one of the states to the state controller in equation (25).

4.3.2 Simulation Methods and Results

Simulations were carried out in MATLAB/Simulink to determine the expected response of a utility-scale PV inverter to grid voltage phase shift disturbances. In the model, an array of 40 parallel by 10 series 1Soltech 1Sth-215-P 215 W PV panels with an irradiance level of 1000 Wm^{-}

^{2} and a temperature of 25^{o}C were connected to the grid using a switching-level model of a three-phase inverter which included a detailed model of a PLL for PV inverter grid synchronization. The PV inverter model used in shown in Figure 14. A maximum power point tracking (MPPT) perturb & observe (P&O) algorithm was implemented on the dc-dc interface between the PV and the inverter to model the realistic behavior of PV inverters as they continuously track the MPPT. The inverter was driven by a sinusoidal pulse width modulated (SPWM) signal at a switching frequency of 2.1 kHz. The simulation was executed, and instantaneous grid voltage phase shifts of 15°, 30°, and 60° were injected 1.5 s after the start of the simulation (which began in steady-state). The results obtained are presented in Figures 15 through 20 for phase shifts of 15°, 30°, and 60°. Whenever a phase shift occurs, there is a significant reduction of the three-phase voltages, as well as reduction of current supplied to the grid in all the phases. It was observed that the impact of phase shift on the voltages and currents increased as the phase shift value increases. Figure 19 shows a situation of nearly complete voltage collapse a couple of cycles after the phase shift event; similar result was also observed with the phase currents in Figure 20. The simulated results were tested under resistive load conditions (i.e. no stiff grid connection) thus there is a very predictable relationship between each phase voltage and current.

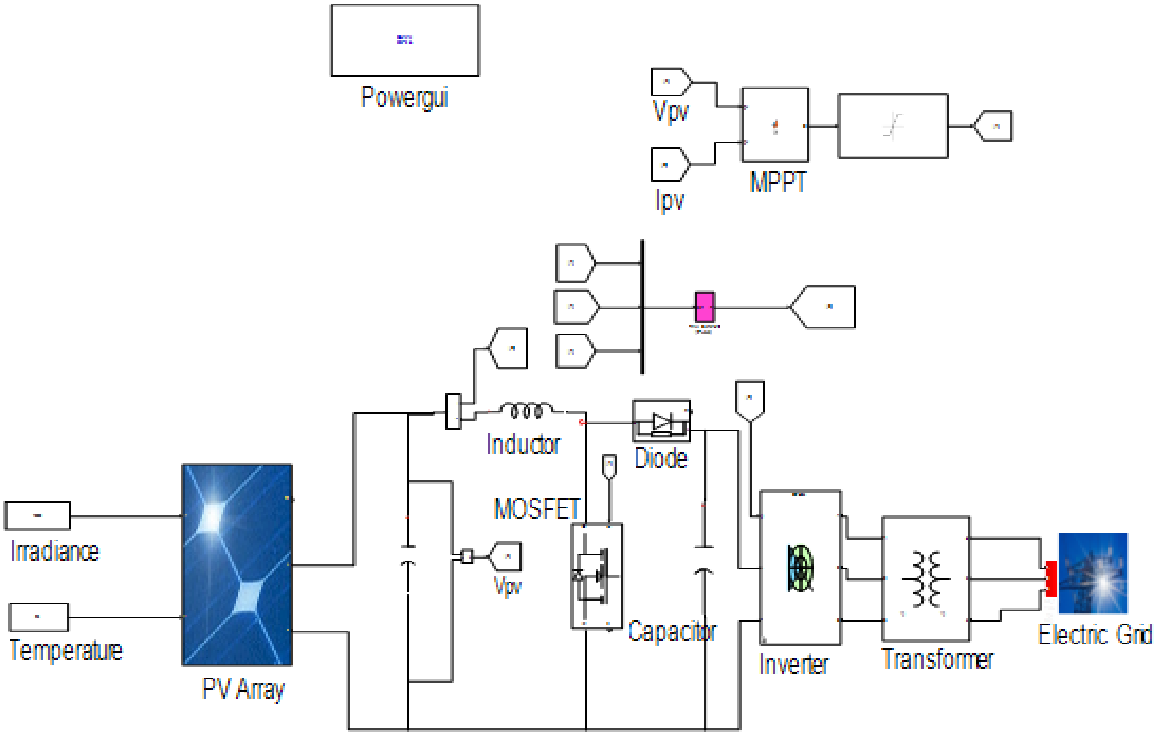

Figure 14. PV inverter model.

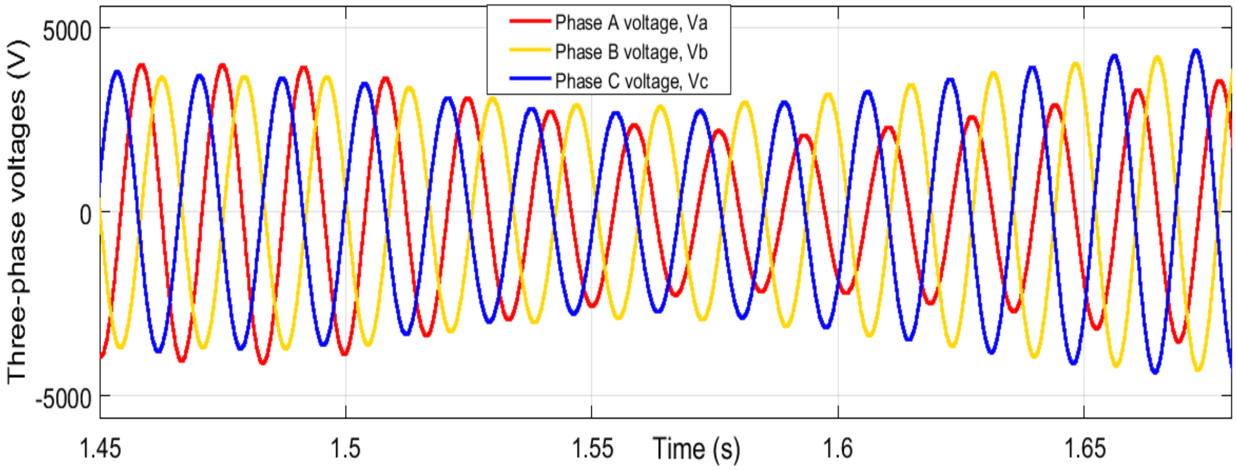

Figure 15. Three-phase voltages, $\boldsymbol{V_a}, \boldsymbol{V_b}, \boldsymbol{V_c}$, when the phase shift is 15°.

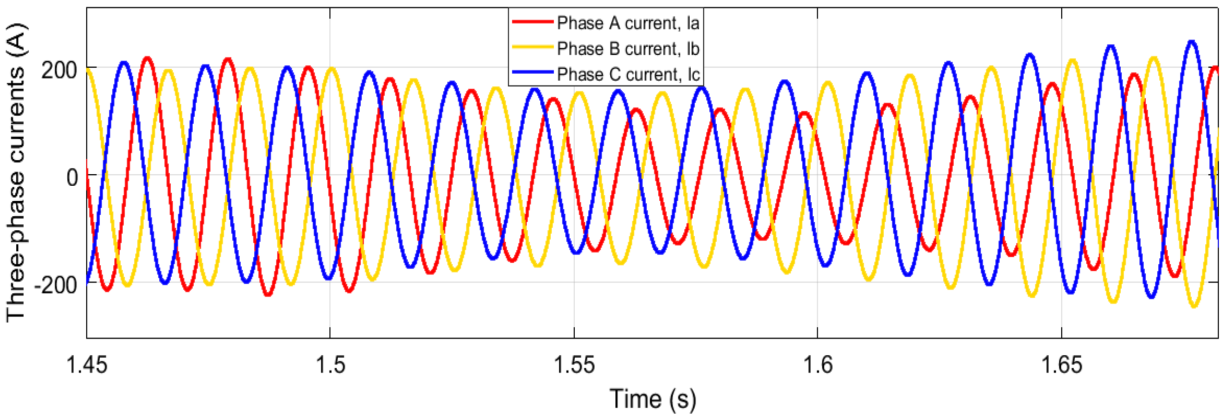

Figure 16. Three-phase currents, $\boldsymbol{I_a}, \boldsymbol{I_b}, \boldsymbol{I_c}$, when the phase shift is 15^0.

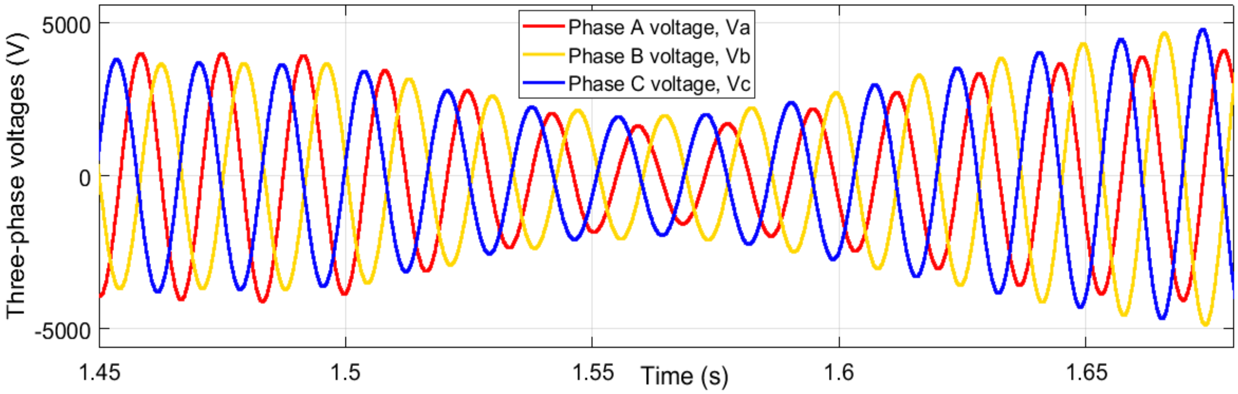

Figure 17. Three-phase voltages, $\boldsymbol{V_a}, \boldsymbol{V_b}, \boldsymbol{V_c}$, when the phase shift is 30°.

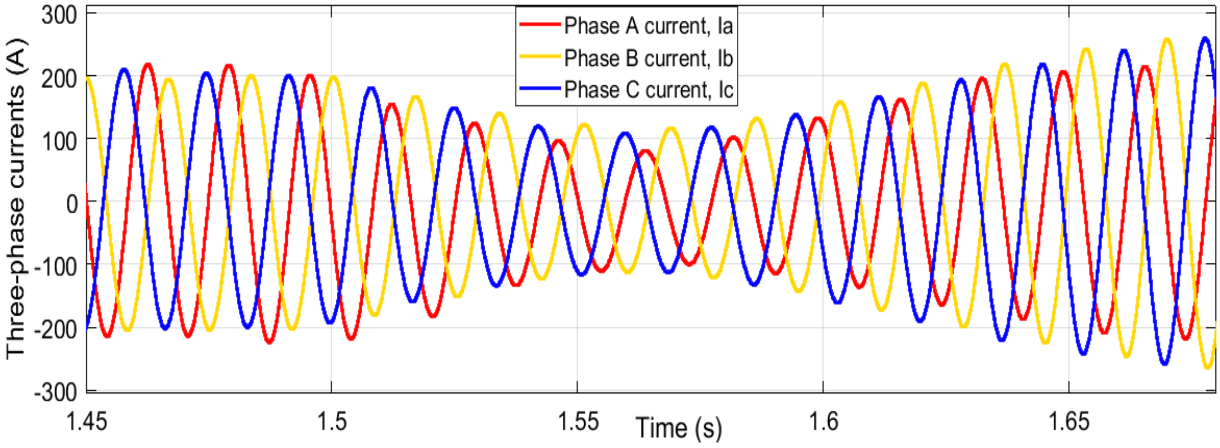

Figure 18. Three-phase currents, $\boldsymbol{I_a}, \boldsymbol{I_b}, \boldsymbol{I_c}$, when the phase shift is 30°.

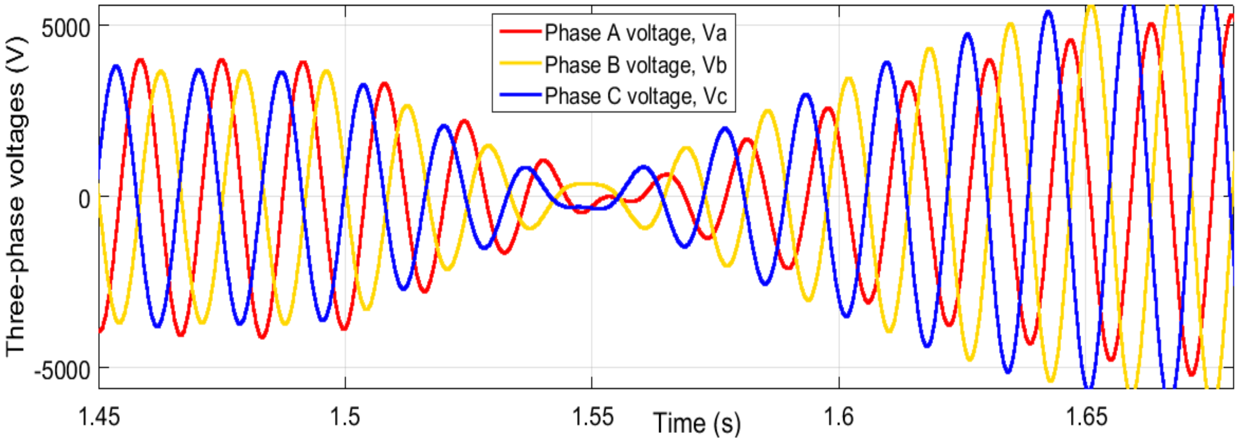

Figure 19. Three-phase voltages, $\boldsymbol{V_a}, \boldsymbol{V_b}$, $\boldsymbol{V_c}$, when the phase shift is 60°.

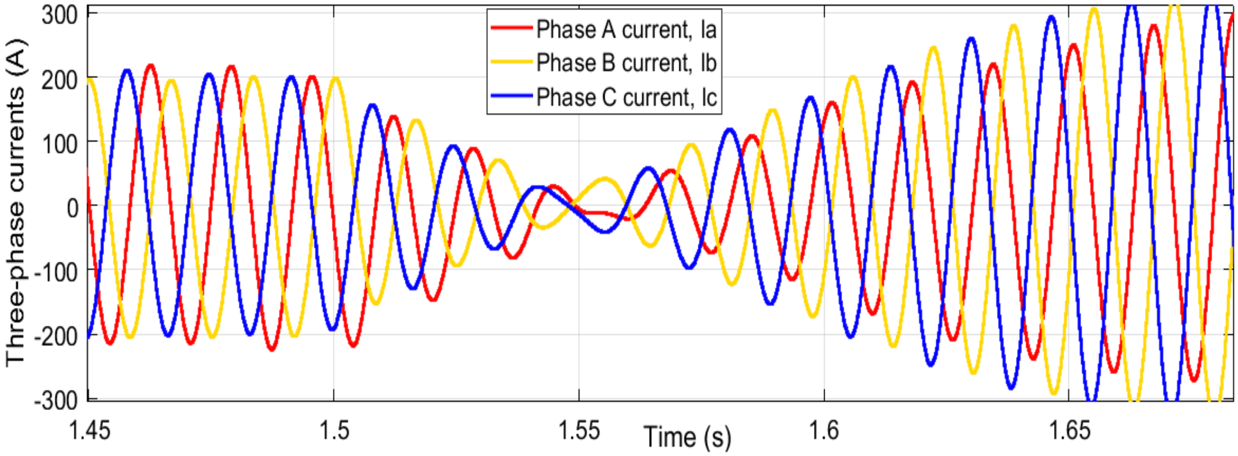

Figure 20. Three-phase currents, $\boldsymbol{I_a}, \boldsymbol{I_b}$, $\boldsymbol{I_c}$, when the phase shift is 60°.

4.3.3 Experimental Methods and Results

The experiment was set-up using a grid simulator, 500 kW utility-scale PV inverter, PV simulator, connecting cables, current sensors, oscilloscope, computer, and the OpalRT real-time simulator. The OpalRT is a Simulink-compatible real-time simulator. Phase shifts were implemented using the transport delay block, clock, and switch blocks in the Simulink library. The current sensors were used to measure the current flowing from the inverter to the grid via the oscilloscope. The grid reference voltages, generated by the OpalRT – effectively being used as a highly configurable signal generator – and the resulting grid voltages, supplied by the grid simulator, were also measured on the oscilloscope. Phase shifts of 15°, 30°, and 60° were subjected to the grid voltage (all three phases) after a period of normal grid operation sufficient to startup the PV inverter and have the system settle to a steady-state operating point equivalent to the conditions shown in Table II. The OpalRT was also used to supply a trigger signal to the oscilloscope to capture the PV inverters response to the phase shifts.

The grid operational model used for this experiment was built using Simulink and RT lab blocks such as the OpComm, OpCtrl and the OP5142 EX Analog Out blocks. As mentioned above the OpalRT system was used as a configurable signal generator in a open loop fashion. The grid conditions (voltage and frequency) were normal at all times with the exception of the phase shifts subjected during the laboratory experiments. The grid model was compiled, loaded, and built in the RT lab before hardware execution at a sample rate of 200 μs. Figure 21 shows the basics of the OpalRT and oscilloscope setup. All laboratory testing was completed at NREL’s Energy System Integration Facility (ESIF) in Golden, CO.

Table II. Parameters of the experimental PV inverter and the grid simulator.

Parameters	**Values**
PV inverter dc power	176 kW
Grid simulator phase voltages	277 V
Grid frequency	60 Hz
Sample rate	200 μs

Figure 21. A view of the laboratory experimental set-up.

The outcomes of the experiments are presented in the figures below. A screenshot of the results obtained from the oscilloscope are presented in Figures 22 through 25. The three-phase voltages are at the top, while the three-phase currents are at the bottom. Phase A (V_a), phase B (V_b), and phase C (V_c) voltages are the purple, red and yellow lines respectively. The first three channels, and the next three channels are the same as expected, and they represent the reference phase voltages measured from the OpalRT analog output and the actual grid voltages supplied by the grid simulator respectively. Phase A (I_a), phase B (I_b), and phase C (I_c) currents are the pink, green and purple lines respectively on the last three channels.

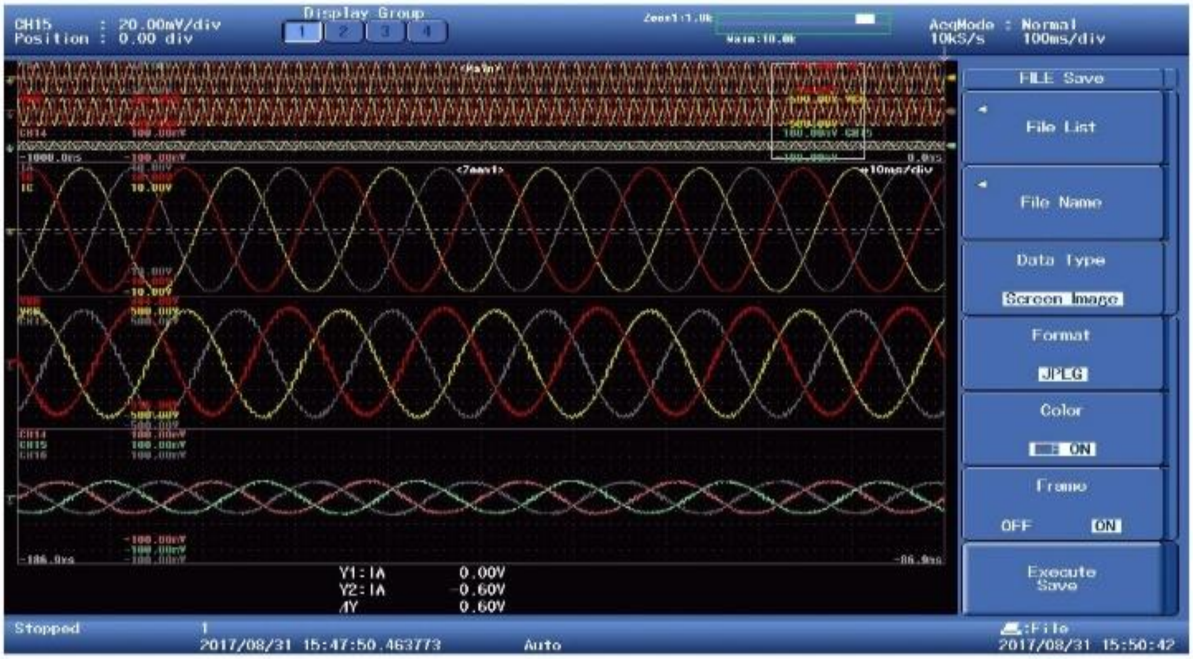

Figure 22. Three-phase voltages and currents at zero phase shift.

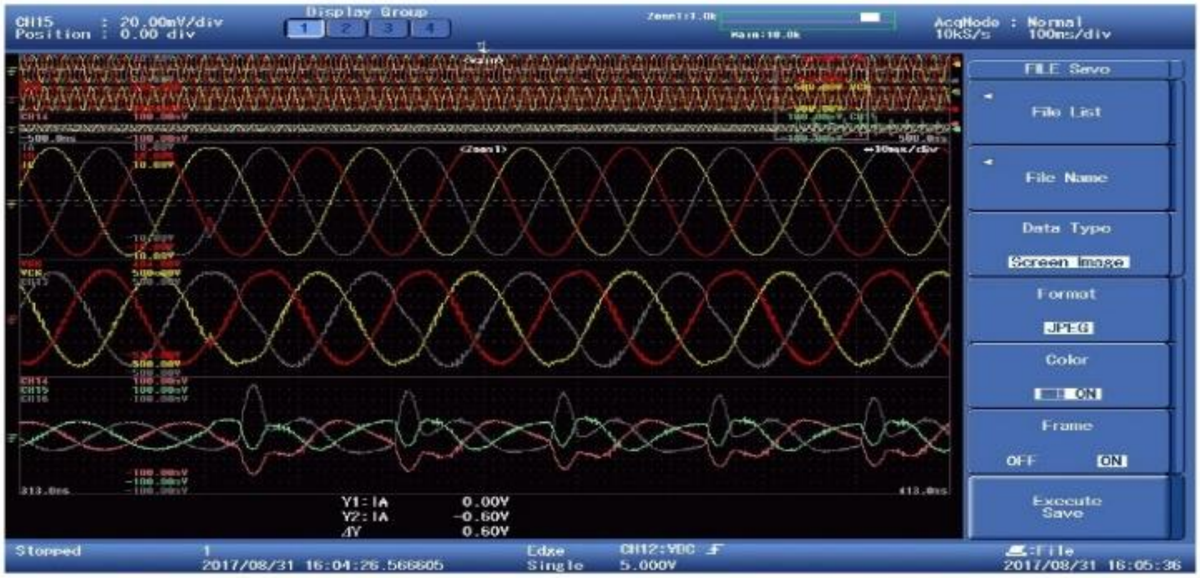
CH15 : 20.00mV/div
Position : 0.00 div
AcqMode : Normal
10kS/s 100ms/div
Data Type: Screen Image
Format: JPEG
Color: ON
Frame: ON
Y1: IA 0.00V
Y2: IA −0.60V
ΔY 0.60V
Stopped 1 2017/08/31 16:04:26.566605
Edge Single CH12:VDC 5.000V
File 2017/08/31 16:05:36

Figure 23. Three phase voltages and currents when phase shift is 15°.

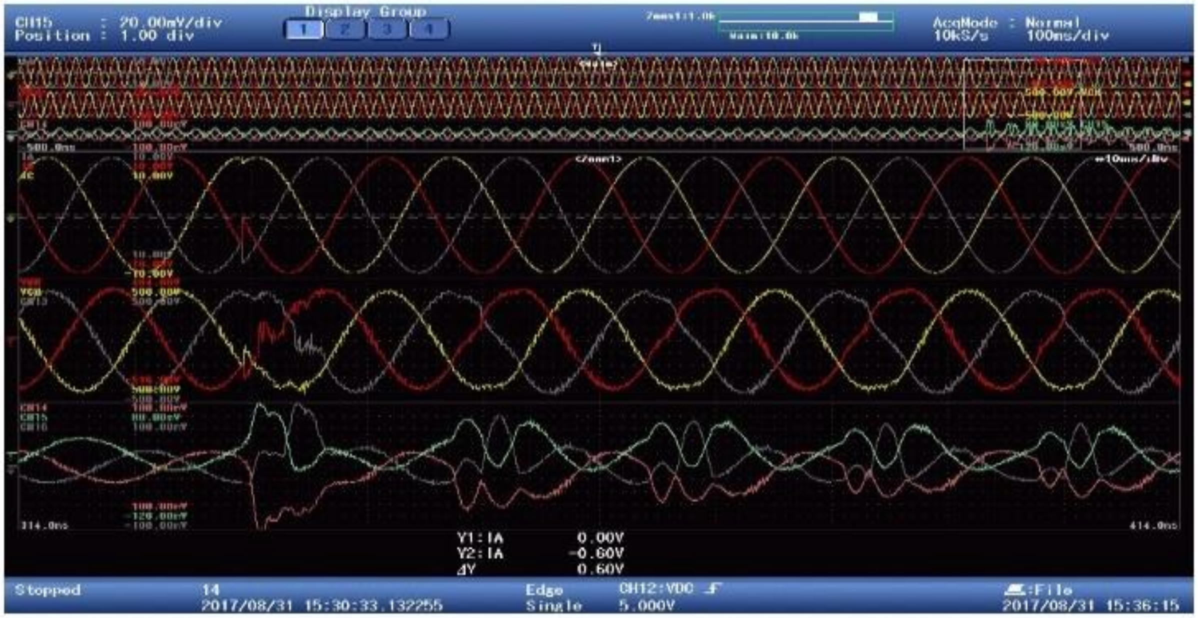
CH15 : 20.00mV/div
Position : 1.00 div
AcqMode : Normal
10kS/s 100ms/div
Y1: IA 0.00V
Y2: IA −0.60V
ΔY 0.60V
Stopped 14 2017/08/31 15:30:33.132255
Edge Single CH12:VDC 5.000V
File 2017/08/31 15:36:15

Figure 24. Three phase voltages and currents when phase shift is 30°.

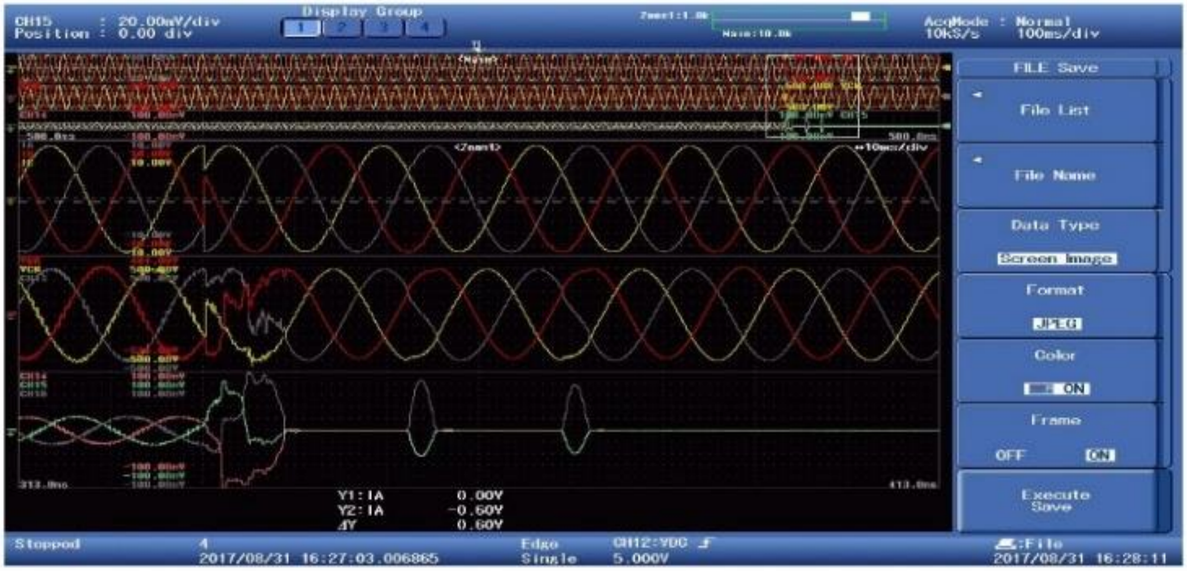

Figure 25. Three phase voltages and currents when phase shift is 60°.

Figures 22 through 25 are the laboratory results under a normal operating condition, and phase shifts of 15°, 30°, and 60° respectively. Whenever a phase shift occurs, there is an instantaneous collapse of the three-phase voltages, and a reduction of current supplied to the grid in all the phases. This is also the same for the simulation results except that the voltages maintained a nearly constant voltage with little distortions after the event due to the low impedance (stiff) grid connection in the experimental setup. For the experimental cases, the values of the three-phase currents in Figures 23 and 24 shows a tracking of the current magnitude and phase mainly with the action of the PV inverter controllers and PLL, but this is characterized with periodic current spikes and distortions. In both the simulation and experimental cases, the distortion was minimal at 15°, and stability was quickly achieved after a few seconds. A case of inverter tripping was observed in the laboratory as shown in Figure 25. The inverter went offline and the output current went to zero shortly after the phase shift of 60°. This is validated by the simulation results of Figure 20, where the output current collapses to near zero immediately after the phase shift event. The results of these simulations and experiments can then inform the operation of the state controller during fault conditions that often occur during natural disasters.

4.4 LABORATORY TESTING OF A UTILITY-SCALE PV INVERTER'S OPERATIONAL RESPONSE TO GRID DISTURBANCES

As DER penetration continues to gain relevant attention; the behavior of such system within the existing power delivery system need to be adequately understood. Since the characteristic response of such devices under fault condition remains largely unknown, this test was carried out with the aim of analyzing a PV inverter behavior during faults that usually happen during an extreme event. This would enable us to incorporate such model to the proposed state controller so that a stable equilibrium can be achieved during extreme events. This section provides experimental results of a commercial size (500kW) solar PV inverter during simulated grid disturbances. This device was tested using simulations of three different disturbances; distribution, transmission, and an event collected during the Blue Cut Fire Event. The methods used for testing the three different scenarios of grid disturbances are detailed and the test setup is described. Additionally, the test results for each of the grid events are provided and an analysis of the test results is given. The test results show that the tested PV inverters response to grid disturbances depends on the characteristic of the disturbance itself and not on the frequency ride-through settings implemented. The information provided by this work can inform utilities, manufacturers, developers, and system planners of the potential performance of solar PV inverters during grid events.

The response of the electric grid is, at its most general, largely a function of the dynamic responses of all the interconnected generators and loads. The relatively recent sizeable inclusion of large amounts of renewable energy in electric power systems around the world has focused research interests into how such renewable systems affect the dynamic response of these systems. A large study from the bulk system perspective of the US's Western Interconnect concluded that large shares of renewable energy could be integrated while maintaining system-wide transient stability [79]. However, the report also emphasized the need to good power system planning and engineering practices and specifically concluded that the accurate modeling of solar photovoltaics (PV) and wind were necessary to complete accurate studies and system analysis. The same recommendations were given in a report focusing on the bulk system reliability impacts of distributed energy resources (DERs) [80]. The Western Electricity Coordinating Council (WECC) developed the composite load model [81] and PVD1 [82], which include simplified aggregate models of distribution systems and the expected response of PV systems respectively for modeling DERs impact within a dynamic bulk system model. Tuning of these models for specific distribution characteristics was demonstrated by [83] and [84]. Still, such models assumed that PV inverters would trip off-line according to their programed voltage and frequency trip settings.

This section focuses on experimental efforts to determine if such assumptions are valid. Additionally, this work aims to inform utilities, manufacturers, developers and system planners of the potential performance of current solar PV inverters during grid transient stability events. Frequency ride-through capability refers to the ability of a generator to continue operation during off-nominal frequency periods generally caused by contingencies on the bulk electric system. For bulk system generators of all types a standard, NERC PRC-024-2 [85] has been developed specifying the required relay settings for generators with the intent of providing frequency ride-through capability to avoid cascading generator trips due to worst case planned contingencies. A generator may trip for other reasons such as equipment protection but generally PRC-024-2 required settings should provide frequency ride-through for most generators. For DER systems, the de facto standard specifying ride-through has been IEEE 1547-2003 [86] which required much less frequency ride-through as DER, and specifically PV, deployment when the standard was developed was negligible compared to the bulk system generators. Now, with the growth of PV at both the transmission and distribution scales there has been much discussion regarding the frequency ride-through capabilities necessary from PV systems (comprised of one or more inverters). An update of IEEE 1547, currently nearing completion, is likely to require significant frequency ride-through capability to address reliability concerns of DERs response to system-wide frequency events. On August 16th, 2016 a fire in Southern California caused multiple faults on high-voltage transmission lines over a 4-hour period. Some of these faults led to the immediate loss of up to 1200 MW of PV generation located in the Southern California Region. Analysis of the event, known as the Blue Cut Fire Event, cited that PV systems tripped off due to a miscalculation of frequency during the fault events [87]. Modeling of the event, including the momentary cessation of active power output of some of the PV plants, and additional details and recommendations were provided in [88]. In October, 2017 another similar event was also reported. These events highlight the potential availability impacts of PV systems when the PV systems respond to abnormal conditions.

4.5 LABORATORY TESTING METHOD

Laboratory testing of a PV inverter’s response to typical abnormal grid conditions resulting from system faults was focused on evaluation of a 500 kW utility-scale PV inverter. These inverters are effectively the power electronic building blocks used in both distribution-connected and transmission-connected PV power plants (500 kW to 100’s of MW). The inverter tested was not the newest model available and had limited capability regarding the setting of high and low voltage settings. All laboratory testing was completed at NREL’s Energy System Integration Facility (ESIF) in Golden, CO. The number of possible transient-level abnormal conditions characteristic of an electrical grid’s, or a portion of an electrical grid’s operation is vast. In order to elucidate representative PV inverter responses via a limited number of possible laboratory tests six specific scenarios were developed. Each scenario is defined by the grid disturbance waveforms presented at PV inverter’s point of interconnection and the high and low voltage ride-through capability required of the inverter via programmatic settings within the PV inverter controller.

Three grid disturbance waveforms were prepared for the test and were designed to be representative of different types of voltage waveforms prevailing from different types of faults and different fault locations within the power system. 26 shows the three grid disturbance waveforms used in laboratory experiments. These waveforms are data obtained under actual conditions from the electricity grid in Southern California during a wild fire event. These are the typical waveforms that could be expected during natural disasters such as the 2016 blue-cut wild fire event in Southern California that led to a widespread blackout. Two waveforms, denoted as “Dist. Timing” and “Trans. Timing” are nearly identical but the duration of the disturbance is different, typical for distribution and transmission protection performance. In both cases the grid disturbance results in high-harmonic content on all three phases but the voltage magnitude and fundamental frequency are relatively normal.

- The “Dist. Timing” disturbance is present for about 9 cycles and was chosen as being representative of a voltage disturbance caused by a fault on at the distribution-system-level and thus the fault is cleared by relatively slow acting distribution protection equipment.
- The “Trans. Timing” disturbance only occurs for 2 cycles before the voltage waveforms return to normal thus representing a disturbance due to a fault cleared at the transmission-system-level.
- The third disturbance waveform was collected during one of the fault events which occurred during the Blue Cut Fire. It is characteristic of a phase-to-phase fault where the disturbance only affects two of the three phases. This disturbance lasts only 2.5 cycles before the system returns to normal operation following the presumed fast response of transmission-level protection equipment. As can be seen in 26 the phase-to-phase disturbance generates considerable phase shift between the normal 120° phase relation of the three-phase voltages.

These three disturbance waveforms were chosen as to investigate the PV inverter’s response to faults occurring in different parts of at different distances from the PV system.

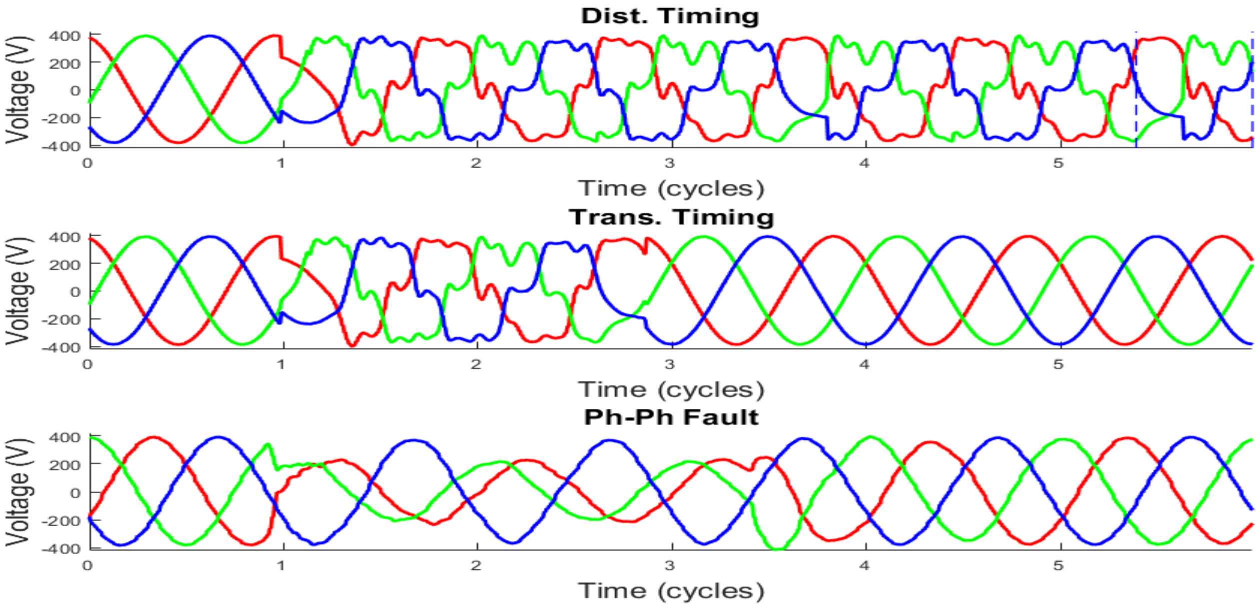

Figure 26. Grid disturbance three-phase voltage waveforms used for testing and representing different types and durations of characteristic faulted system conditions.

Two different frequency ride-through settings were evaluated during laboratory testing. Figure 26 shows the frequency/time envelopes used in these tests. Note that the time scales in the two plots are different.

I. Distribution Protective Settings: Frequency trip settings that are compliant with IEEE 1547-2003 [85] were developed and used to simulate typical settings that most distribution-connected PV systems currently use. IEEE P1547 compliant settings were not developed because the standard has not yet been finalized or published as of the date of this publication. Regardless, a large amount of PV is currently interconnected under the IEEE 1547-2003 standard and thus it was useful to investigate the expected response of these DERs.

II. Transmission Protective Settings: Frequency trip settings were developed that are in alignment with the minimum ride through requirement defined by PRC-024-2 [85]. The PRC-024-2 compliant settings provide more extensive frequency ride-through capability than the IEEE 1547-2003 settings.

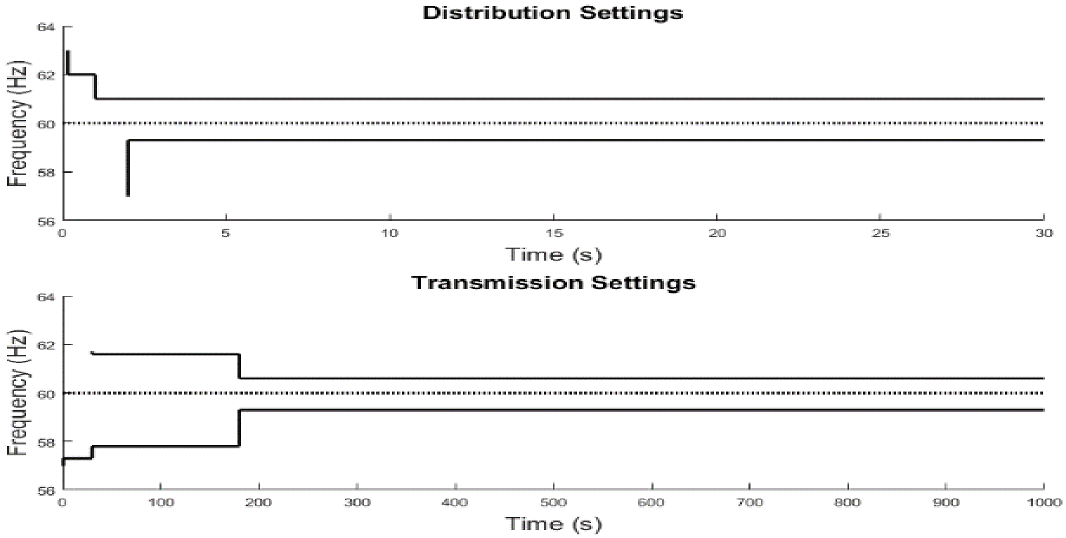

Figure 27. Frequency and time envelopes of frequency ride-through capabilities for Distribution and Transmission protective settings.

The voltage ride-through setting programmed in the PV inverter for all tests required zero-voltage-ride-through for a minimum of 300 ms, and required continuous operation within 1.1 and .75 per unit voltage for a minimum of 500 ms.

The basic experimental setup of equipment used for laboratory testing is shown in Figure 28.

- Photovoltaic (PV) Simulator: a 500 kW PV simulator was used to provide DC power to the PV inverter. A relatively basic I-V curve, describing the current and voltage relationship of the PV array being simulated, was employed as testing did not include any variability of the solar resource.

- Equipment under Test (EUT): a 500 kW PV inverter was used. The frequency ride-through protective settings were modified based on both the IEEE 1547-2003 and PRC-024 compliant settings.

- Grid simulator: a bi-directional 500 kW grid simulator was connected to the PV inverter. The grid voltages which the grid simulator generated were driven by analog inputs (one per phase) derived from an OpalRT real-time simulator.

- Signal Generator: OpalRT was used as a configurable signal generator and was programed using Simulink. The reference waveforms from the OpalRT were configured to provide normal grid conditions for a period of time sufficient to allow the PV inverter to start-up and assume steady-state operation prior to the introduction of each of the grid disturbance waveforms shown in Figure 28 . The OpalRT update rate of the grid voltage reference signals was 200 µs. While this experimental setup used the OpalRT, the testing completed is not power-hardware-in-the-loop (PHIL) testing as there was no intentionally modeled change in the grid simulator voltage due to changes in PV inverter current output.

- Data acquisition: an oscilloscope was configured to measure and record the grid reference voltages supplied by the OpalRT model ($V_{A,ref}$…), the simulated grid voltage (V_A…) and the current supplied to the grid by the PV inverter (I_A…). A signal to trigger the oscilloscope at an appropriate time was also provided by the OpalRT model.

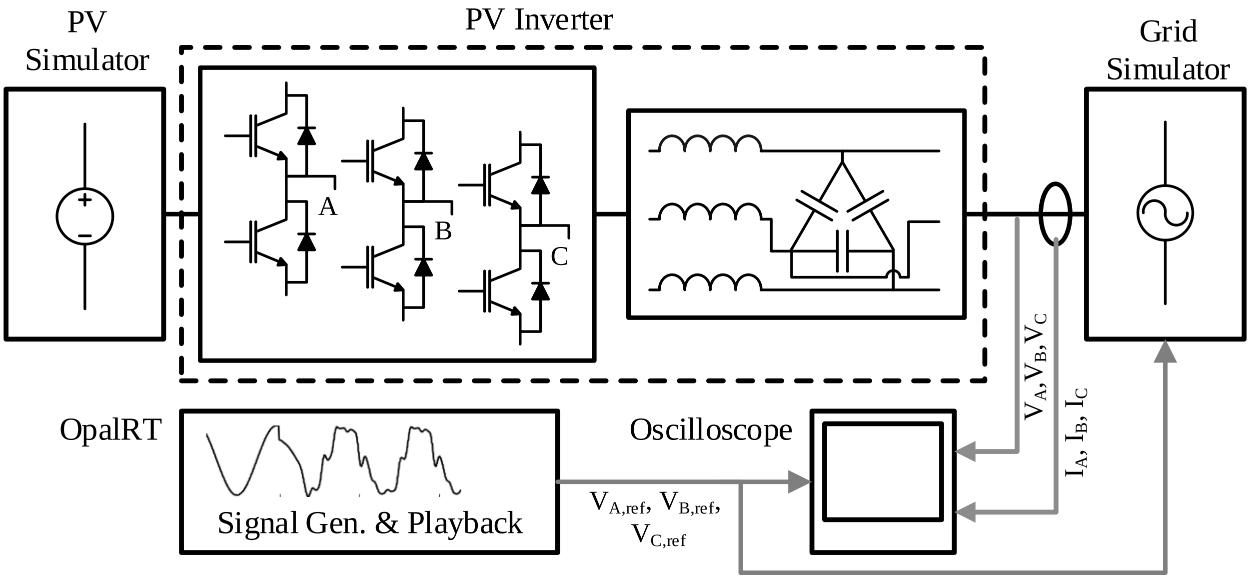

Figure 28. Diagram of the experimental setup of the 500 kW PV inverter under test including OpalRT operating as a signal generator and an oscilloscope for data capture.

As the OpalRT system was being used as a reference signal generator for the grid simulator it was of interest to first test the ability of the grid simulator to accurately track the rapidly changing disturbance waveforms. These waveforms also show close agreement indicating that the simulated grid waveforms do accurately produce the grid voltage reference waveforms.

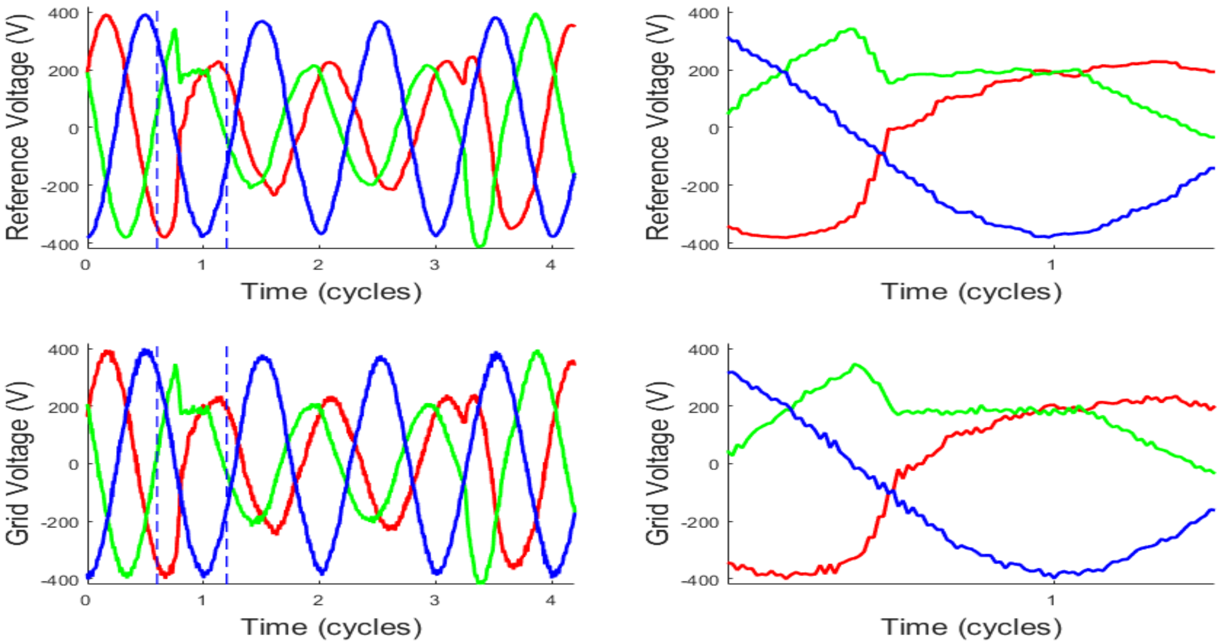

Figure 29. Grid reference voltages and simulated grid voltages produced during the phase-to-phase fault scenario.

4.5.1 Experimental Results

For all the results shown in this section the PV inverter was operated at approximately 250 kW or half the rated power of the inverter. A few tests were completed at higher and lower power output, but no significant change in the PV inverter response was seen.

Laboratory testing was performed for each of the three disturbances pair with one of the two ride-through settings for a total of six testing scenarios. Many scenarios were evaluated more than once but all repeated tests provided identical results. As a result, no statistical analysis of the results was warranted. Figure 30 shows the experimentally collected data for the PV inverter's response to the "Dist. Timing" grid disturbance waveform with the Distribution Protective Settings defined in section III. The PV inverter clearly ceased operation about ½ cycle after the beginning of the abnormal voltage waveforms. The PV inverter indicated that the PV inverter tripped off-line due to grid frequency being out of the range of the frequency requirements. The cause of the inverter trip was determined both by reviewing fault codes that were indicated on the user interface of the inverter and by reviewing inverter fault logs.

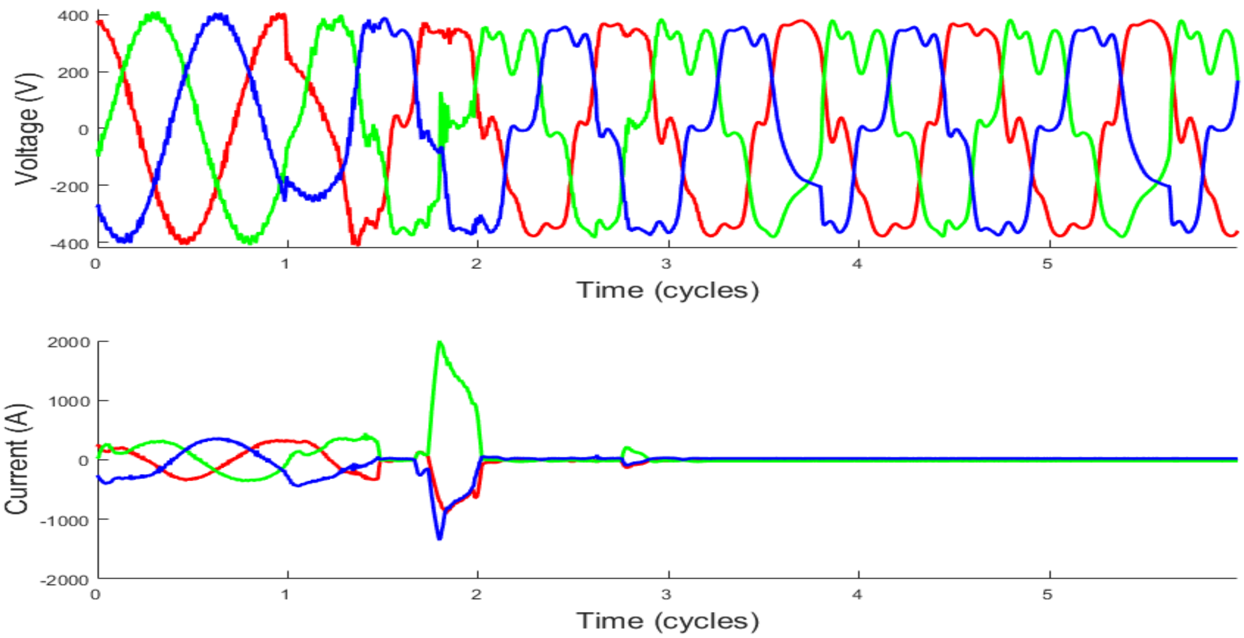

Figure 30. PV inverter response to characteristic distribution-level grid disturbance (slow clearing of fault) with Distribution frequency ride-through settings.

Figure 31 shows the experimentally collected data from the PV inverter's response to the "Trans. Timing" grid disturbance waveform with the Transmission Protective Settings. Much like the distribution-level grid disturbance the PV inverter ceases to produce power following the start of the voltage disturbance and two attempts to resynchronize are evident. Again, the PV inverter reported that the trip was due to frequency ride-through parameters.

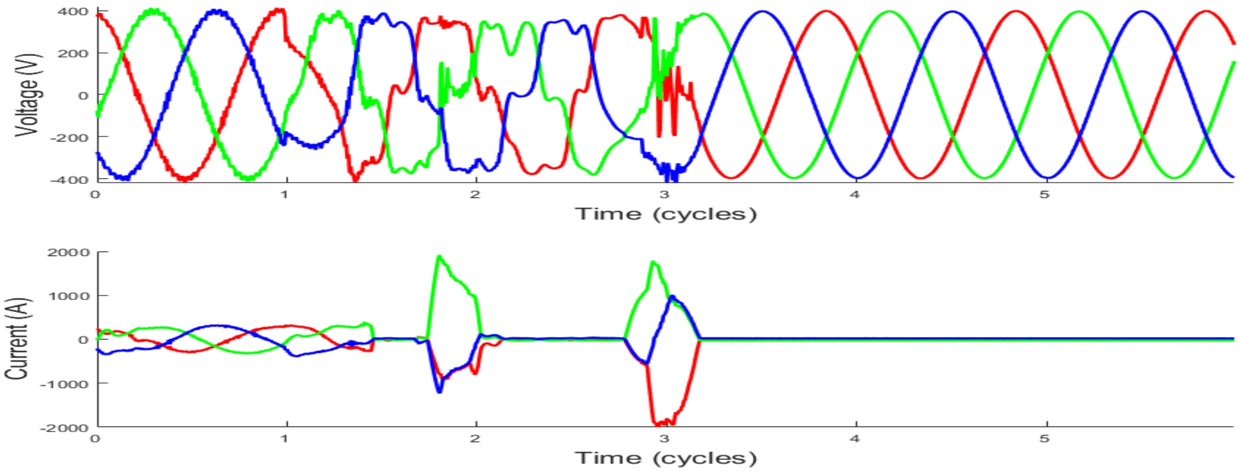

Figure 31. PV inverter response to characteristic transmission-level grid disturbance (fast clearing of fault) with Transmission frequency ride-through settings.

Figure 32 shows the results for the PV inverter response for the characteristic phase-to-phase fault grid disturbance, again with the Transmission Protective Settings. In this case the PV inverter maintains operation during the entire fault period. Small variations in the inverter phase currents are visible, particularly at the onset of the grid disturbance, but such variations are relatively small.

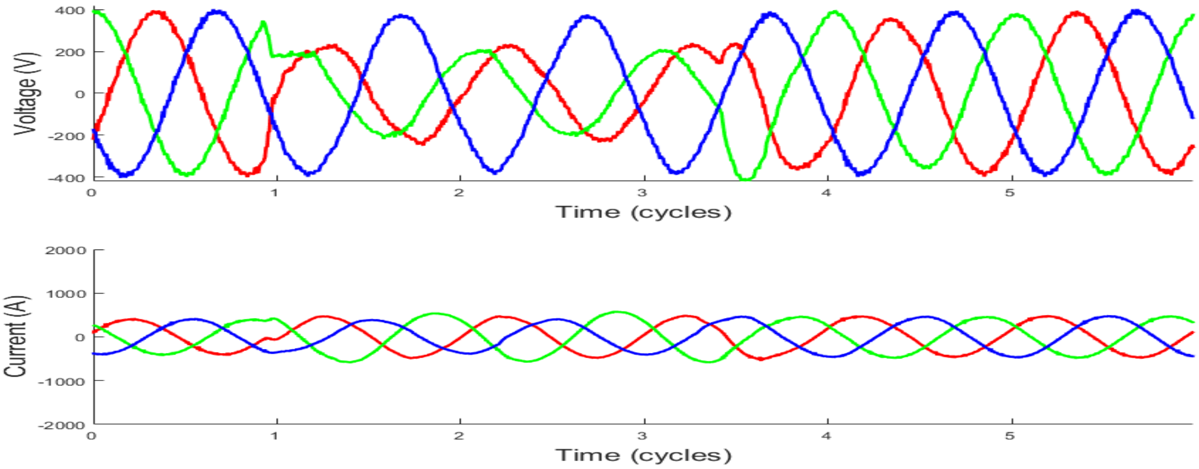

Figure 32. PV inverter response to characteristic transmission-level phase-to-phase fault disturbance (fast clearing of fault) with Transmission frequency ride-through settings.

Table III gives a summary of all the PV inverter operational responses to the six scenarios tested. Examination of the table shows that the laboratory tests revealed that responses depended solely on the voltage disturbance waveform and not on the implemented frequency protective settings.

Table III. Summary of PV inverter response to all tested scenarios.

	Voltage Disturbance Waveform		
FRT Capability	Dist. Timing	Trans. Timing	Ph-Ph Fault
Distribution	Tripped on frequency	Tripped on frequency	Did not trip
Transmission	Tripped on frequency	Tripped on frequency	Did not trip

4.5.2 Results and Discussions

The insensitivity of the frequency ride-through or frequency tripping capabilities that were tested would indicate that the frequency calculated by the PV inverter for both the distribution-level and transmission-level grid disturbance waveforms is far from the nominal expected operating frequency of 60 Hz, despite the fact that no frequency shift was present in the input waveforms. However, it is hard to determine what is causing the PV inverter to trip so quickly even if the calculated grid frequency is vastly different from the assumed grid frequency. Specifically, for the tests using Transmission Protective Settings, even a large deviation in frequency is expected to be tolerated for short periods of time but the inverter clearly determines that the grid frequency is out of range within about ½ a cycle.

There also appears to be some evidence that the inverter is implementing a zero-crossing detection -based frequency measurement which, on a cycle-by-cycle basis (or half-cycle), could explain the very fast measurement of a considerably low or high grid frequency leading to the frequency ride-through capability insensitive behavior discussed above. Close inspection of 30 shows that the PV inverter trips offline very close to the zero-crossing of phase C (shown in blue). If frequency measurement was by zero-crossing detection on phase C such an immediate shutdown of the inverter would be expected as phase C is phase shifted by the disturbance resulting in a potentially very high frequency measurement. Both of the above findings are aligned with the Blue Cut Fire Event report findings, which is a wildfire and a very common type of extreme event in this part of the country [87].

This section reports on laboratory-based experiments which were completed to inform the expected operational characteristics of utility-scale PV inverters to various grid disturbances as would be seen on the electrical grid during faulted conditions. The main reason why we investigate PV systems is because they do not depend on lifelines, which is an important feature during natural disasters. Multiple characteristic grid disturbance waveforms including high-harmonic voltage waveforms, long and short fault clearing, and a specific phase-to-phase fault condition were investigated. Additionally, two levels of frequency ride-through capability of the PV inverter were also tested. The results show evidence that the PV inverter’s frequency ride-through and tripping characteristic is dependent on the specific grid disturbance and seems insensitive to the implemented frequency ride-through settings. This indicates that a mis-measurement of grid frequency is likely leading to presumed very high or low grid frequency effectively defeating ride-through capability. Hence, the likely behavior of the inverter during such event can then be used to inform the state controller in order to maintain to improve the grid resilience to such disturbances.

4.6 PROPOSED STATE CONTROLLER

The availability of power systems is the goal of major electricity networks; however, this availability and reliability has been under constant attack by natural disasters, which in many cases result into black-outs. During these extreme events, revenues and power transmission are lost, and the power system needs to be rescued from the instability that may arise from this. Therefore, resilience is being discussed as a subject of focus in the contemporary modern power systems. This dissertation proposes a microgrid robust control model that improves the power system resilience by reducing the downtimes in the V-shaped region of the resilience curve. This control method offers the additional opportunity of controlling the microgrid by exploring the time-dependent resilience index of the microgrid. The proposed approach has been studied considering the 2008 Hurricane Ike event in the Matagorda area of Texas to ascertain its effectiveness. The impact of natural disasters on telecommunication and power infrastructures, including the 2010 Chile and 2011 Japan earthquakes were discussed in [89]-[91]. In this case, it was observed that the communication infrastructure depends on the power system as much as the power system depends on it.

The state controller measures the state of the system, compares it to a set of system requirements and then feeds them into the microgrid energy management system (EMS). The EMS then enables the energy storage device to support the microgrid while rejecting disturbances and perturbations. The state of the system can be considered as the nominal voltage and frequency of the system. Under these conditions, the system is said to be in steady state. Faults, wind speed variation, fluctuating load demand or natural disasters may however affect the operation of the system and cause the value to deviate from its operating point.

Current designs for improving resilience include the interconnection of microgrid, batteries and renewable energy sources. However, this combination may not be sufficient to withstand the perturbations that arise during natural disasters. Hence, this paper proposes an additional state control method, which helps to increase the resilience of the power system by exploring its state parameters. Natural disasters affect the operation of the power system and cause it to deviate from its operating point. The state controller explores the parameters of the system to adjust it to a defined set point. The state controller measures the state of the system, compares it to a set of system requirements and then feeds them into the microgrid energy management system (MEMS). The MEMS then enables the energy storage devices to support the microgrid while rejecting disturbances and perturbations that could be observed during natural disasters.

The state of an ac microgrid system can be given by its buses voltage and frequency. The action of the state controller can be mathematically defined as follows:

Given a set of extreme events, *K,* the error in the state estimate is defined as:

$$\Delta x_i = x_i - \mathbf{x}; \; i = 1, 2,.., \mathrm{N} \tag{16}$$

$$\hat{\boldsymbol{x}}_{\boldsymbol{i}} = k_P \, \Delta x_i + k_i \int_0^{\tau} \Delta x_i dt + k_d \frac{d\Delta x_i}{dt} \tag{17}$$

$$\hat{\boldsymbol{x}}_{\boldsymbol{i}} - \mathbf{x} \rightarrow \mathbf{0} \text{ (during and after event)} \tag{18}$$

where; N is the number of state estimates, **x** is the reference state, x_i is the estimated state measured and $\hat{\boldsymbol{x}}_{\boldsymbol{i}}$ is the output state of the controller. k_P, k_i and k_d are the proportional gain, integral gain and derivative gain respectively.

The output of equation (17) is used to send a command to the controller and the MEMS, which then communicates to commanded energy storage devices to an appropriate level by either injecting or absorbing real power. The tracking error, simply known as the control term, is designed to be close to zero at any time, t. The hierarchical control architecture is depicted in Figure 33. Resilience is time-dependent and can be enhanced by reducing the area of the V-shape in Figure 4. The V-shaped region is approximated as the space between t_1 *and* t_3. Prior to time, t_1, is known as the pre-event state, after time, t_3 is known as the post-restorative state. Between t_1 *and* t_2 is the degradation state that depends on the ability of the system to withstand the extreme event. Improving resilience between this region is important and can be achieved through a combination of both operational and infrastructural resilience.

Among all the phases, the most important region is the time between t_1 *and* t_2, known as the recovery or restoration state. This state constitutes a larger part of the system downtimes, which could be mitigated through operational resilience. A higher resilience (shorter downtimes) can be achieved by shifting the entire part of the curve where $t > t_3$ to the right of t_2 and also shifting the section where $t < t_1$ to the left of t_2, and would be achieved through the incorporation of a fast state controller as proposed in this paper.

The area of the V-shape can be defined in terms of the controller design as an "energy" function, defined as:

$$V \approx -\boldsymbol{\delta} \cdot \mathbf{t} \tag{19}$$

where δ is hereby called the resilience momentum indicating the impulse action of natural disasters on the power system and t is the time vector when the resilience values are being measured. When considering energy storage as a buffer that can be used to enhance resilience, we can assume a battery energy storage system (BESS) delivering power to the load with an autonomy, T_{bank}

$$V \approx \frac{}{2} \delta_{av} T_{bank} \tag{20}$$

where the average (moving) resilience momentum δ_{av} is given as:

$$\delta_{av} = \int_{t}^{t+\delta t} |\boldsymbol{\delta}| \, dt \tag{21}$$

Combining Equations (4) and (20) then becomes:

$$V \approx - \frac{}{2\mu} \delta_{av} \, \text{In} \left(\frac{1- \rho_L}{1- \rho_B}\right) \tag{22}$$

Equation (22) shows that as resilience increases, the downtime decreases. Additionally, a positive correlation exists between the autonomy of the energy storage, T_{bank} and uptime, T_U given by equation (23) as:

$$T_U = \text{g} \, (T_{bank}) \tag{23}$$

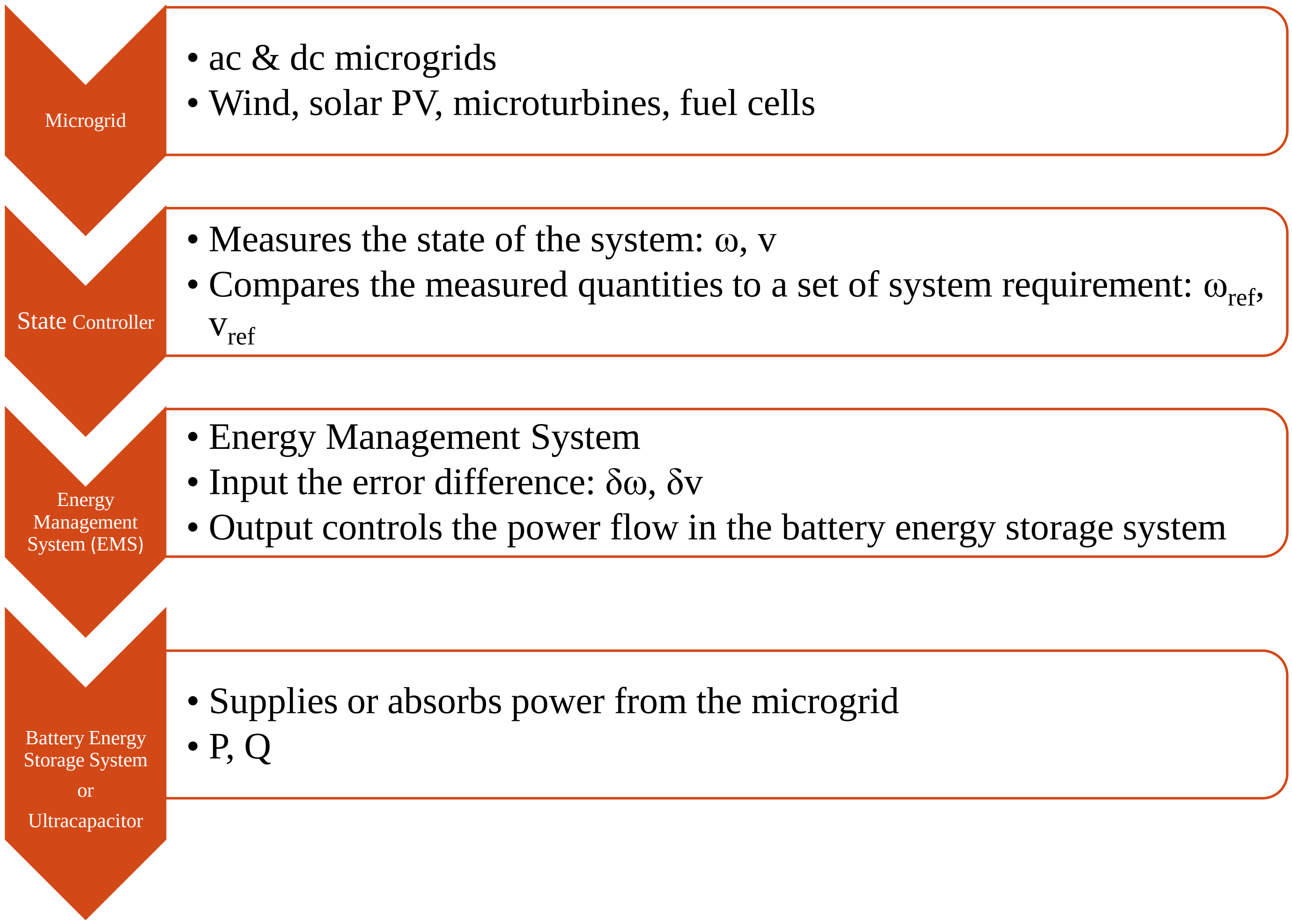

Figure 33. Hierarchical control architecture.

4.6.1 Analysis of the Microgrid Controllable Resilience during Extreme Events

State controllers provide fast response because of their direct action to the internal states of the system. In this sub-section, the stability of a power system is evaluated based on loss of load frequency (LOLF) and the operational frequency and voltage of the system during disturbances are studied using MATLAB simulations. The system was simulated under very high wind speeds (40-60 m/s), that are known to occur during hurricanes and the effectiveness of the proposed approach was validated. The non-linear dynamics of the microgrid system can be generally represented as:

$$\dot{x} = f(x, t\ ) \text{ and } \ x(t_o) = x_0 \qquad x \in \mathbb{R}^n \tag{24}$$

$$x = [w \quad v \quad \phi \quad u_d]^T \tag{25}$$

where, *x* is the state, *w* is the angular frequency, v is the voltage and ϕ is the phase angle. Hence, the Lyapunov function in equation (20) can be alternatively written as:

$$V = -a\,J\,w^2 + -b\,C\,v^2 + k\ \phi \tag{26}$$

where *J* is the inertia, C is the capacitance; a, b, and k are constants.

A fundamental lemma used in the design of the state controller can be found in theorem 4.4 [92], which states that:

Let D be a region of size ϵ *around the origin,*

$$D = \{x \in \mathbb{R}^n : ||x|| < \epsilon\} \tag{27}$$

$V(0, t) = 0$ *and* $V(x, t) \geq \alpha\,(||z||^p)$ $\quad p \geq 2,\ \forall z \in D,\ \ \forall t \geq 0.$

It is also positive definite because $\alpha\,(||z||^p) \rightarrow \infty$ *as* $z \rightarrow \infty$

$V(x, t) \leq \beta(||z||^p)$ $\quad p \geq 2,\ \forall x \in D,\ \forall t \geq 0$ *makes it a decrescent function under the same condition.* Hence, it is now possible to investigate the stability of the system using the energy function in equation (28).

$$\dot{V} = a\,J\,w\,\dot{w} + b\,C\,v\,\dot{v} + \ k\phi^q, \tag{28}$$

$$i = C\,\dot{v} \tag{29}$$

$$\tau = J\,\dot{w} \tag{30}$$

When the microgrid is delivering power to the load, it is possible to assume that the current, i and torque, τ are both positive

$$\dot{V} = a\,\tau\,w\ + b\,i\,v\ +\ k\phi^{q} \tag{31}$$

By letting $a, b, k < 0,\ q = 2,\quad \dot{V} < 0$, and the origin is globally asymptotically stable according to Barbashin-Krasovskii Theorem [93].

4.6.2 Case Study: 2008 Hurricane Ike in the Matagorda Area of Texas

As shown in Figure 34, a decrease in downtime and increase in resilience was achieved after the incorporation of a state controller. The initial dependent resilience values were obtained from Table I of [94], shown in Table IV below, based on the 2008 Hurricane Ike event in the Matagorda area of Texas. These resilience values were calculated from actual data during this event and were obtained from the first time the disaster was noticed to the time when the restoration work was completed. The average up and downtimes were also presented in Table I of [94]. Time-dependent resilience values were interpolated at regular periods between the degradation and restorative phases. An incorporation of the state controller commands a meaningful level of storage, which leads to an increase in uptime as shown by equation (32), this increase in uptime results in a decrease in downtime and a corresponding increase in the resilience values were obtained from (22). The resulting graph is shown in Figure 34.

The result of applying the proposed control is to decrease microgrid downtimes during the degradation and restoration phases, which implies a corresponding increase in resilience between these phases. The size of the approximated V-shaped region reduces. The total decrease in downtime can be expressed as:

$$\xi = (t_{1s} - t_1) + (t_2 - t_{2s}) \tag{32}$$

It is expected that a decrease in downtime is ultimately a gain in the system resilience and a quick recovery from blackout. This can also reduce the revenue loss by connecting the load back online very quickly.

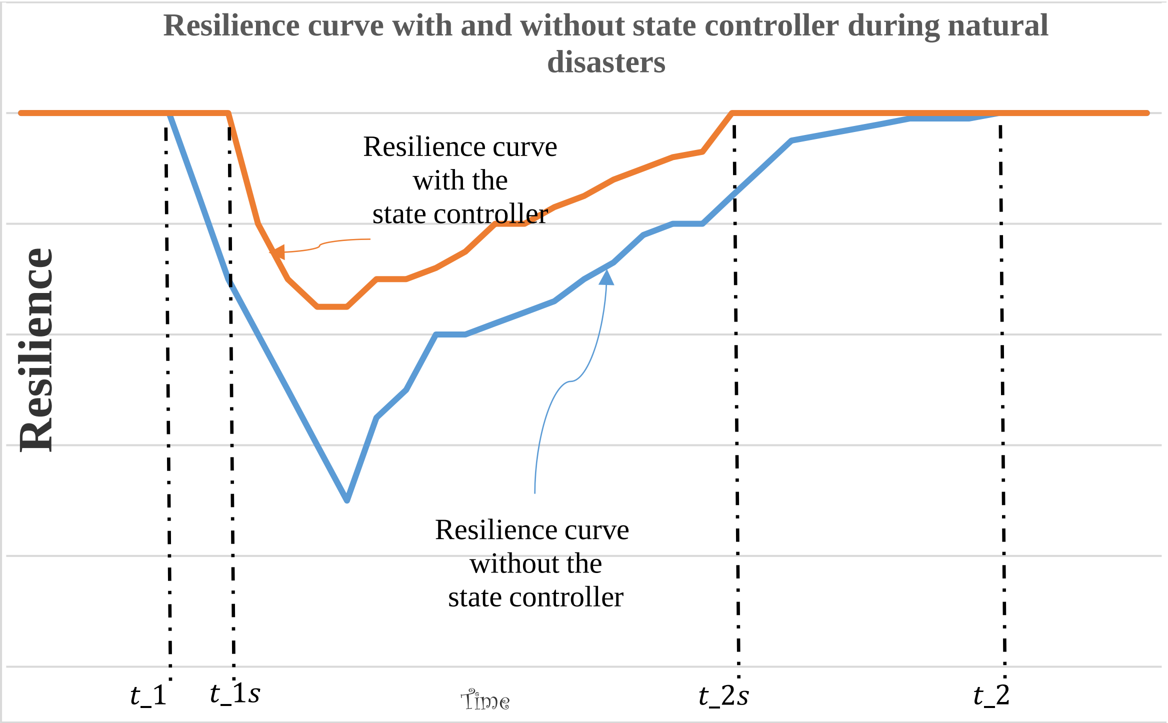

Figure 34. Resilience curve with and without the state controller during extreme events.

Table IV. Table of resilience values, uptime and downtime [94]

Resilience value without energy storage	0.99
Resilience value with 1-day autonomy of energy storage	1.00
Average uptime (days)	25.78
Average downtime (days)	0.16

4.7 ONLINE IMPLEMENTATION OF COORDINATIVE REAL-TIME SUB TRANSMISSION VOLT-VAR CONTROL (CREST-VCT) UNDER HIGH PHOTOVOLTAIC PENETRATION

This section details the determination of the reactive power that the controller commands in order to keep the system voltage under control both in normal conditions and during an extreme event. The analyses were carried out in a research team at the Pacific Northwest National Laboratory (PNNL), a laboratory of the U.S. Department of Energy (DOE). With the rapid penetration of the solar photovoltaic (PV) and other distributed energy resources (DER) into the grid, it is prudent to leverage these resources to provide ancillary services to the grid, such as voltage regulation. Recent literature shows how smart inverter-based DERs can participate in reactive power dispatch and thus improve voltage regulation. However, most of the reactive power dispatch algorithms are based on quasi-static assumptions of the traditional power flow methods. Therefore, these algorithms may not represent the dynamic behavior of the power systems, especially when the grid is rapidly losing its inertia due to power electronics interfaced renewables, giving rise to faster dynamics. Moreover, various delays due to computation and communication all pose challenges to the real-world adaptation of real-time control algorithms. In this section, the challenges and feasibility of a coordinated real-time sub transmission volt-var control algorithm (CReST-VCT) for voltage regulation by a hardware in the loop implementation was investigated. The dynamic behavior of a IEEE 118 bus system is simulated in real-time using the Opal-RT ePHASORsim tool. An AC-OPF based reactive power optimization is performed using the General Algebraic Modeling System (GAMS) to solve for coordinated reactive power dispatch of PV inverters and shunt devices in the system along with controllable load resources such as demand response. The results are reported and demonstrate significant improvement in system-wide voltage profiles.

The fast-evolving electric grid has many new features; bidirectional distribution power flows, vehicle-to-grid integration, and DER requiring effective coordination and control among the resources. Under such changing scenarios the existing operation needs to be re-validated to ensure that these new resources are optimally utilized to improve grid performance. For example, with ever increasing penetration of inverter-based renewable energy sources such as solar PV and wind, the future grid will have lower inertia, giving rise to faster dynamics and uncertainty in market operation [95]. This calls for an investigation of the feasibility of various quasi-static assumption-based control algorithms. The role of DER in improving grid performance by providing grid supports such as voltage regulation are investigated [96]–[98]. It is necessary to reevaluate the traditional assumptions in steady state and quasi-static analysis due to the changing nature of power systems, particularly those with a higher penetration of inverter-based DER such as solar PV.

Unregulated solar generation can cause significant voltage deviations while coordinated control of grid scale PV inverters can improve voltage profiles which would not otherwise have been achieved. Our team at Pacific Northwest National Laboratory (PNNL) has developed a Coordinated Real time Sub-Transmission Volt-var Control (CReST-VCT) algorithm [97], which provides optimal set points for shunt devices and virtual power plants to minimize: (i) voltage deviations from desirable levels at load buses, (ii) system losses, (iii) solar curtailment, (iv) demand response (DR) usage, and (v) mechanical switching of shunt elements [97]. Previously, the algorithm was tested using a quasi-static simulation which assumes: no dynamics of the power system, synchronized action of all controlled devices, no communication of computation delays etc. Across different domains of engineering, Hardware-in-the-loop simulations (HIL) are proven to be an effective way of carrying out real-life validation of algorithms without utilizing the actual system, thereby avoiding any potential damage to the systems [99]–[101].

This section provides details of HIL testing of the CReSTVCT algorithm using the Opal-RT real-time simulator. The power system model is simulated in Opal-RT ePHASORsim [102][103], which emulates dynamic grid behavior. The CReSTVCT algorithm is represented as a control action that is performed by an energy management system (EMS) and acts based on measurements extracted from the grid. The methodology has been tested on an IEEE 118-bus system for a long duration simulation of the grid with PV and load profiles taken for every load bus and appropriate dispatch and commitment schedules being performed by the EMS.

4.8 HIL SETUP AND TEST SYSTEM

The goal of this section is to evaluate if CReST-VCT's performance on real-time, phasor mode, and electro-mechanical transient simulations using ePHASORsim from Opal-RT will bridge the gap in the algorithm's real-world adaptation.

The method presented here is generic and therefore can be adopted to test any quasi-static controller on a dynamic real-time system with a state controller.

4.8.1 Modified IEEE 118-bus test system

A transmission power system that is modified from the IEEE 118-bus system was simulated. The following modifications are considered: a) photovoltaic units are installed as certain 54 load buses and b) switched shunt. Solar PVs in this simulation are modeled as a negative load at the load buses. The net individual real and reactive power consumption is given by:

$$\boldsymbol{P}_l' = \boldsymbol{P}_l + (-\boldsymbol{P}_{pv})$$

$$\boldsymbol{Q}_l' = \boldsymbol{Q}_l + (-\boldsymbol{Q}_{pv}) \tag{33}$$

where $\mathbf{P}_l$ and $\mathbf{Q}_l$ are the load at the bus.

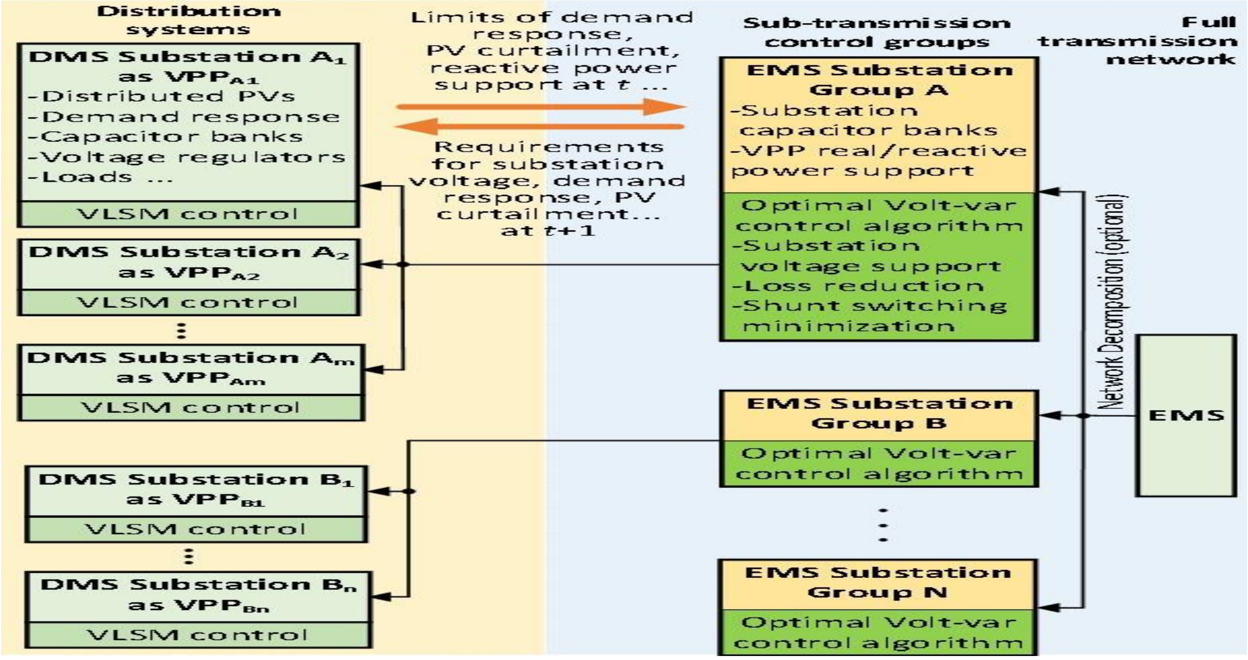

Figure 35. CReST-VCT control architecture.

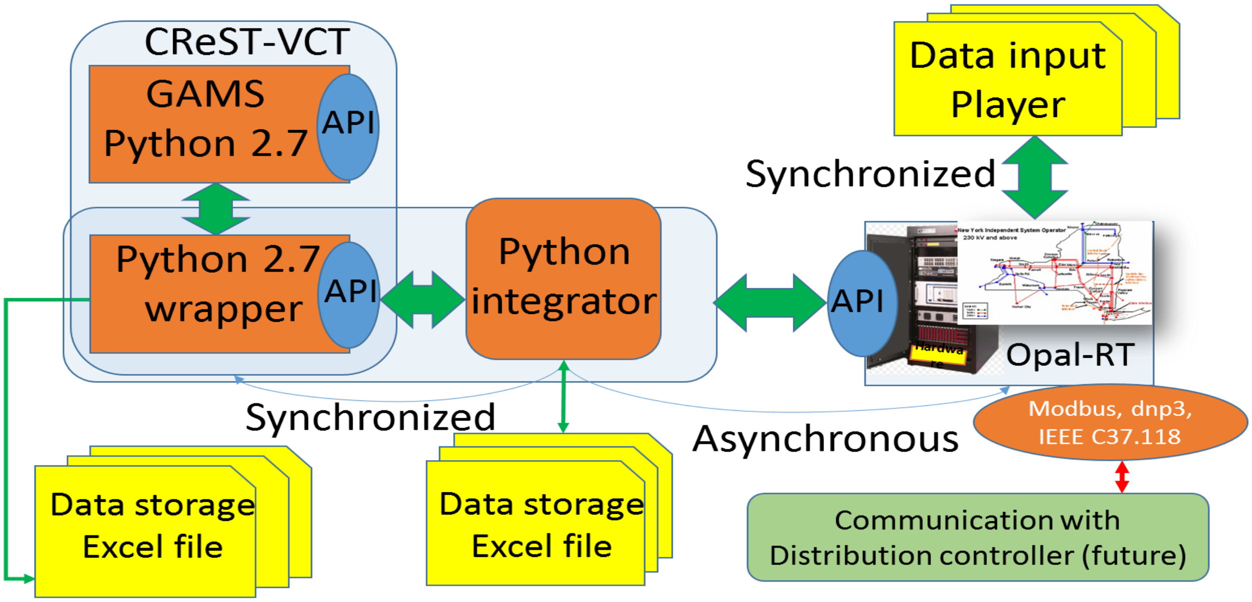

Figure 36. Framework for HIL integration.

Previously, PV inverters are only required to supply real power at a unity power factor. However, standards have been recently revised to ensure that PVs dispatch their reactive power while participating in bus voltage control and regulation [104]. The optimal set points $\mathbf{Q}_{shunt}$ and $\mathbf{Q}_{pv}$ are obtained by running CReST-VCT every 5 minutes. A basic assumption of the model is that all loads at a distribution bus are aggregated as a single lumped load at each *PQ* bus.

4.8.2 Simulation in ePHASORsim

Simulations were performed for the modified IEEE 118-bus transmission system in ePHASORsim developed by Opal-RT. The ePHASORsim dynamic simulation tool is chosen over other platforms like PS/SE for Opal-RT’s real-time and hardware-in-the-loop simulation capabilities. Having a simulation time-step of 110ms, ePHASORsim is suitable for simulation of the electromechanical transient described by the dynamic algebraic equations of the following form [105],

$$\dot{\boldsymbol{x}} = \mathbf{f}(\mathbf{x},\mathbf{u},\mathbf{t}),\mathbf{0} = \mathbf{g}(\mathbf{x},\mathbf{u},\mathbf{t}),$$

where the systems states $\mathbf{x} \in \mathrm{R}^{n}$ are the system states, $\mathbf{f} \in \mathrm{R}^{n\times 1} \rightarrow \mathrm{R}^{n\times 1}$ are the nonlinear function describing the differential equations, and $\mathbf{g} \in \mathrm{R}^{n\times 1} \rightarrow \mathrm{R}^{m\times 1}$ is the function describing the algebraic, nonlinear network constraints. In its most basic form, it consists of a 'master' block and a 'console' block. The master houses the nonlinear ordinary differential equation solver. Only several allowable incoming and outgoing signals which could be dynamically changed during the simulation should be specified in the PIN structure in the form of an Excel spreadsheet [102], [105].

Since there are no dedicated space-holders for solar PVs in ePHASORsim, we modeled the PVs as negative load. There are space-holders for the switched shunts, where the values should be specified as negative reactive power.

A PSS/E dynamic simulation model [106] can be directly incorporated into ePHASORsim by specifying the PSS/E file's dynamic data file (.dyr file) and steady state parameter file (.raw files). However not all component-level models are supported in Opal-RT. From the raw file only the information related to the generator, load, line, and 2-winding transformers are selected. For the .dyr files: only 'GENROU', 'TGOV' 'EXAC4', and 'STAB1' models are supported. Anything other than these supported models should either be converted into supported modules or are developed in Modelica [107].

4.8.3 Input Signals

The load forecasts and dispatch signals are updated every five minutes. To emulate the continuously changing load in the power system and avoid abrupt step-changes, first-order-hold is used between values of input signals at two consecutive time-steps. This feature is automatically incorporated when these signals are loaded into the solver through a 'mat' file using the 'From File' block.

It is important to note that the load value in dispatch signals uses a constant power load model, whereas in the dynamic simulation, the loads should be specified in constant impedance. The constant power load value $\overline{P}_l$ were also converted to constant impedance load value $\mathbf{P}_l$. Another point of consideration is the mapping of the set points provided by GAMS and the $\overline{\boldsymbol{Q}}_{pv}^{*}$ into corresponding load buses, since there is no separate place-holder for $\overline{\boldsymbol{Q}}_{pv}^{*}$ in the ePHASORsim simulation.

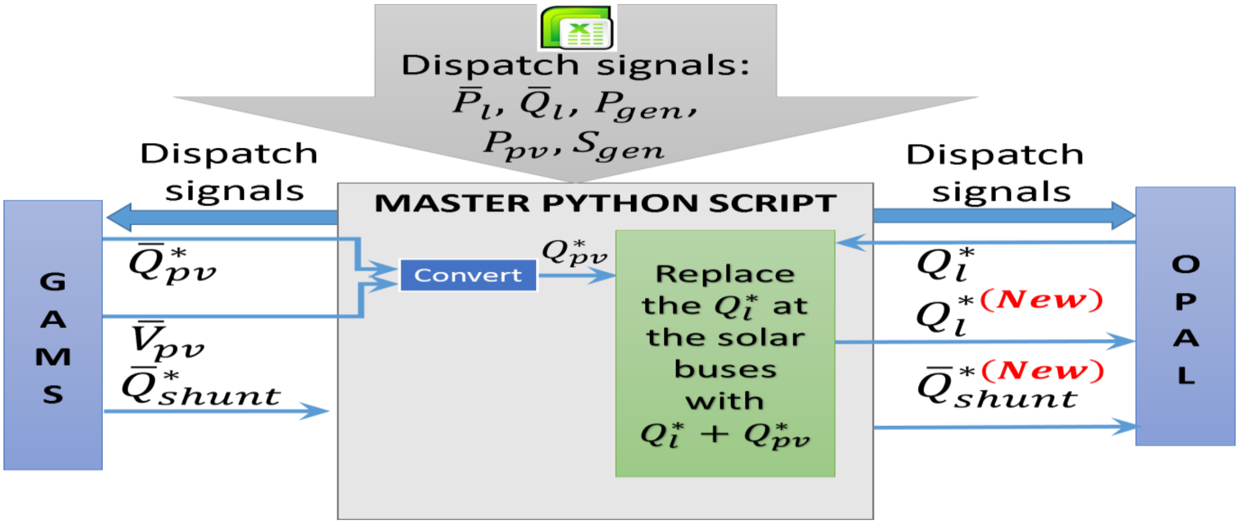

Figure 37. Data exchange.

First, the model is developed in simulation only mode, without connecting any external hardware. The simulation will run as-fast-as-possible for the given computational constraints. The scope of the present work is limited to the preliminary results obtained in the simulation mode. Once tested and verified, the simulation will run in the real-time in hardware synchronized mode. To simulate the communication and processing delays, the following sequence is followed. These time instants are described below.

- **t_0**: dispatch signals are read into the master python script. These signals are sent to both GAMS to run the CReSTVCTand and to Opal-RT simulation.
- **t_x**: After x seconds, GAMS solves the AC-OPF and generates the $\overline{\boldsymbol{Q}}^*_{pv}$ and $\overline{\boldsymbol{Q}}^*_{shunt}$ settings. Then execution of Opal-RT simulation was started.
- **$t_{x+\delta 1}$**: Opal-RT simulation is paused after δ_1 seconds.

  $\overline{\boldsymbol{Q}}^*_{pv}$ is converted to constant impedance values $\overline{\boldsymbol{Q}}^*_{pv}$. System control for the Opal simulation is obtained and the values of $\overline{\boldsymbol{Q}}^*_{pv}$ and $\overline{\boldsymbol{Q}}^*_{shunt}$ are passed.
- **$t_{x+\delta 1+\delta 2}$**: Execution is started and run for δ_2 seconds. Voltage values are read to obtain the steady-state values of the voltages. Here, both δ_1 and δ_2 are chosen to be 20s to account for a conservative estimation of the delays.
- **t_{x+300}**: The execution is resumed until it reaches 300s.

4.8.4 Demonstration and Results

Since one of the major goals of this section is to study the feasibility of implementing a control algorithm based on a quasi-static assumption on a real-world-like dynamical system having high PV penetration, therefore, the voltage profile at various time-instants are plotted to compare the

GAMS-only and Opal-RT simulation voltage with the online implementation of CReSTVCT. As shown in Figure 38, the bus voltages coming from these two simulations are similar. This explains a correlation between the bus voltage values obtained by solving the power flow in GAMS optimization software and by using the Opal-RT real time software. The estimate of the appropriate *Qsolar* from this analysis can then be sent to the state controller in order to achieve a reactive power balance for voltage regulation.

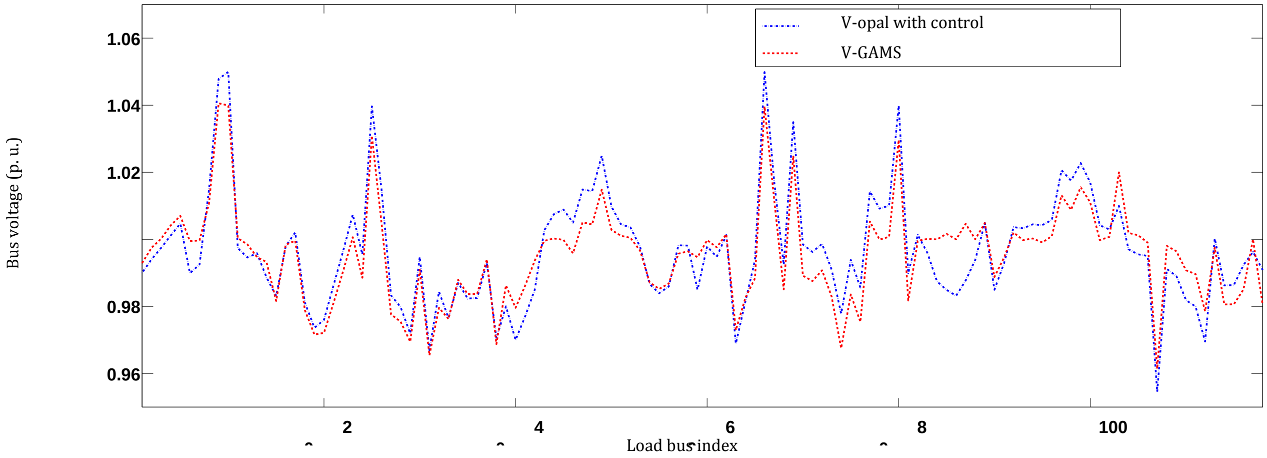

Figure 38. Bus voltages at *time* = 50*s* from GAMS-only and Opal with controller simulation.

The goal is to improve voltage regulation using the online implementation of the control algorithm. In the following Figures, the voltage profile at a couple of chosen load buses are plotted for both the cases with and without the CReST-VCT. As observed in Figure 39, with the control implemented, the voltage profile stays closer to the reference voltage (1p.u) which shows a fine control of the voltage. During an extreme event, this voltage regulation can then keep the system at a stable equilibrium point due to the action of the state controller.

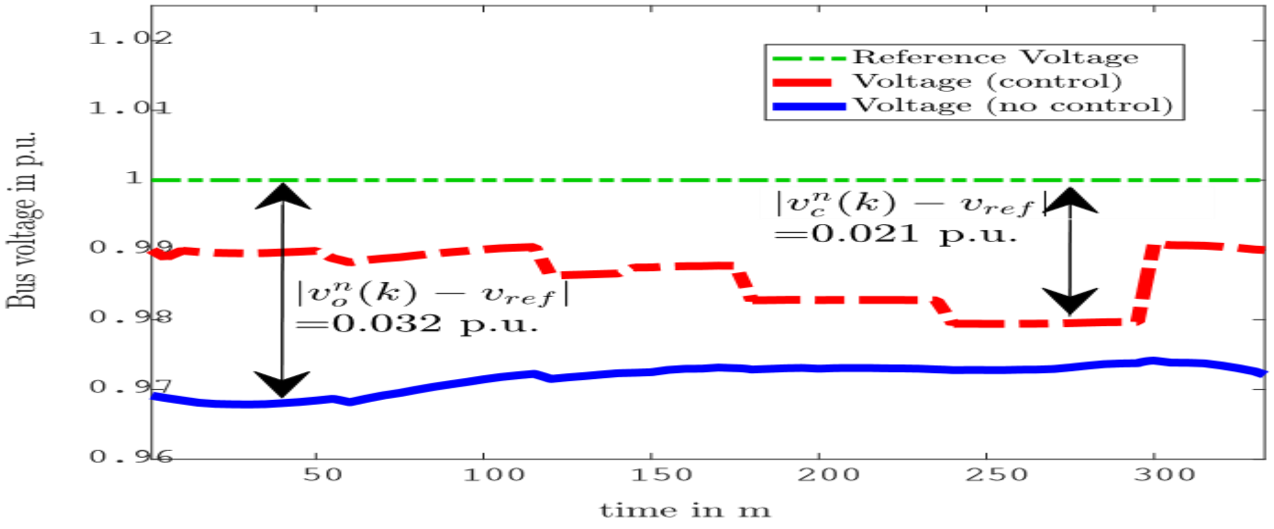

(a) Bus-1 (load bus)

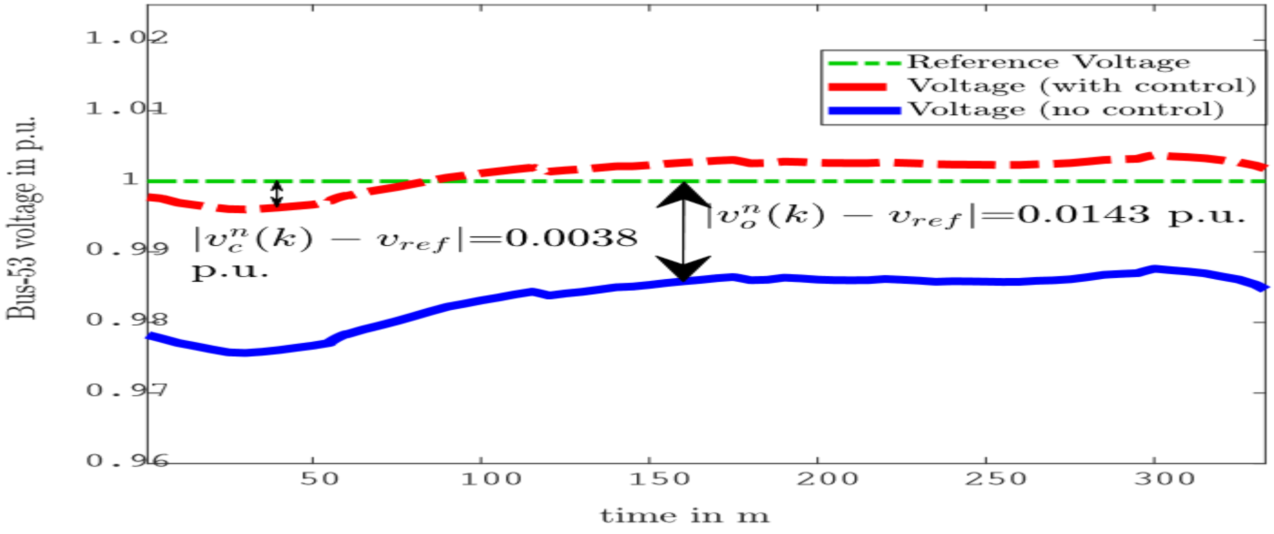

(b) Bus-53 (load bus)

Figure 39. Specific bus voltages from GAMS-only and Opal with controller simulation.

5.0 SIMULATIONS FOR SYSTEM STABILITY

The purpose of this section is to ascertain the effectiveness of the state controller on an ac microgrid when the system experiences a disturbance as it is expected particularly during extreme events. In this section, an ac microgrid was considered using a wind turbine. The generator is a three – phase, 1.5MVA, 575kV, 60Hz, 6- pole DFIG wind turbine. The selected power rating is 1.5MVA, which is typical for largest wind turbines, and it is an acceptable power level for a microgrid. The generator is connected to a resistive 1kV transmission line via a 1kV BUS. The voltage is stepped down to 208 V line-line via a three phase two winding 1/0.208 kV step-down transformer while it serves a local load. A 1.5 MVA generator with a power factor of 0.8 produces a real (active) power of 1.2 MW as shown below.

Real power = 1.5 X 0.8 = 1.2 MW

The slip for induction machines is usually rated about ±0.3. In this study, a slip of -0.25 was selected for it to operate in the generator mode as expected; which makes the machine to operate as sub-synchronous. A positive slip value indicates a motor if otherwise. The simulation was carried out in MATLAB/Simulink by using phasor simulation. We also assume that the thermal limit on the transmission line is higher than the machine rated power.

Transmission line parameters: Line voltage = 1 kV

Line length = 0.5 km

R/X ≈ 1

frequency = 60 Hz

The relationship between inertia and inertia constant is given by equation (34) below;

$$J = \frac{2HS_{rated}}{\omega^2} \quad (34)$$

where:

- J is the inertia in kg.m^2
- H is the inertia constant in s
- S_{rated} is the machine rated apparent power in VA
- ω is the machine rated electrical angular frequency in rad/s
- N is the number of machine pole pairs.

Since the machine rated apparent power and machine electrical angular frequency are fairly constant at steady state, we can conclude that the inertia is directly proportional to the inertia constant as shown in equation (35).

$$J \, \alpha \, H \quad (35)$$

The microgrid operates in islanded mode; which is good for power system resiliency and reliability, and being supported by the power system decentralization policy, it enables integration of renewables such as wind and solar PV. For it to be grid connected, it must satisfy the IEEE 1547 standards on voltage and frequency limits.

The open – loop system frequency changes as the load changes. However, the load is expected to follow the generation to maintain a frequency stability of the system. Hence, a controller has been introduced, this controller compares the frequency of the system to a nominal value of 60 Hz via a comparator or a sum block. The difference between these two frequencies is termed an error output. This error term is then fed in to the input of the PID controller and then connected to the machine. Frequency changes as the wind conditions are not certain, load variations also affect frequency. In practice, the concept of the controller is to ensure that the rotor speed and torque is properly controlled so that the generation matches the load irrespective of those stochastic variables. Hence, the closed – loop control as shown in Figure 40 below gave a steady -state frequency of 60 Hz. However, there are some transients, which persists in the system. Even though these happen within a very few seconds, it still has the capability of either damaging the machine rotor or shutting down the microgrid entirely. This leads us to employing ultracapacitors or battery energy storage system as a solution to the transient challenge. The entire transient is removed but has the capacity of keeping the magnitude of the transient within an acceptable range.

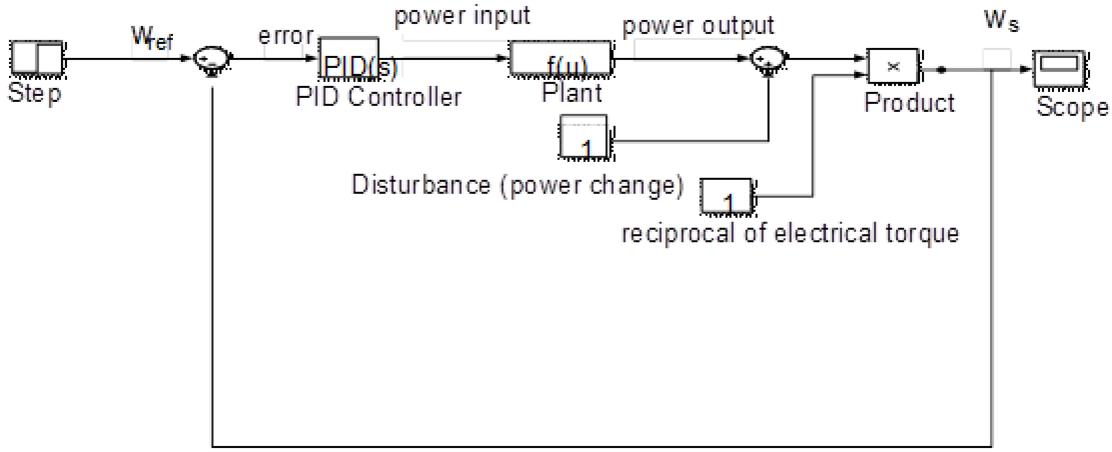

Figure 40. Closed-loop control system.

The simulation was carried out in MATLAB/Simulink using a phasor simulation. The simulation diagram is shown in Figure 41 below.

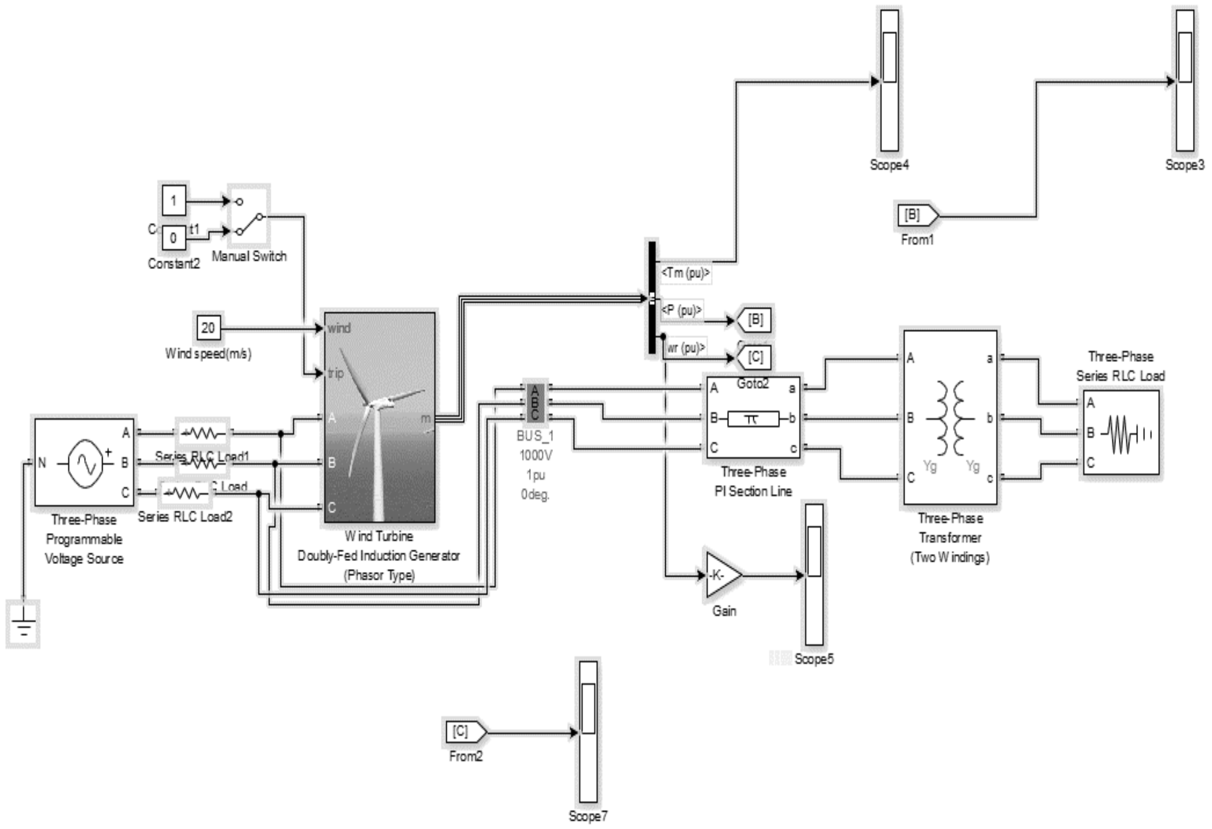

Figure 41. Open-loop simulation model in MATLAB/Simulink.

The open – loop microgrid system in Figure 41 above was simulated and the output load demand is varied to determine the variation in the system frequency. It was observed that the frequency increased to 60. 08 Hz under a light load of 0.6 MW as shown in Figure 42. Similarly, the frequency was observed to increase to 60.24 Hz under a heavy load drop to 0.01 MW in Figure 43. In contrast, the frequency was observed to drop to 59.9 Hz when the load increased to 2 MW as shown in Figure 44. However, the mechanical power output and the mechanical torque output goes to zero as the load demanded had exceeded the maximum power output of the turbine as shown in Figures 45 and 46.

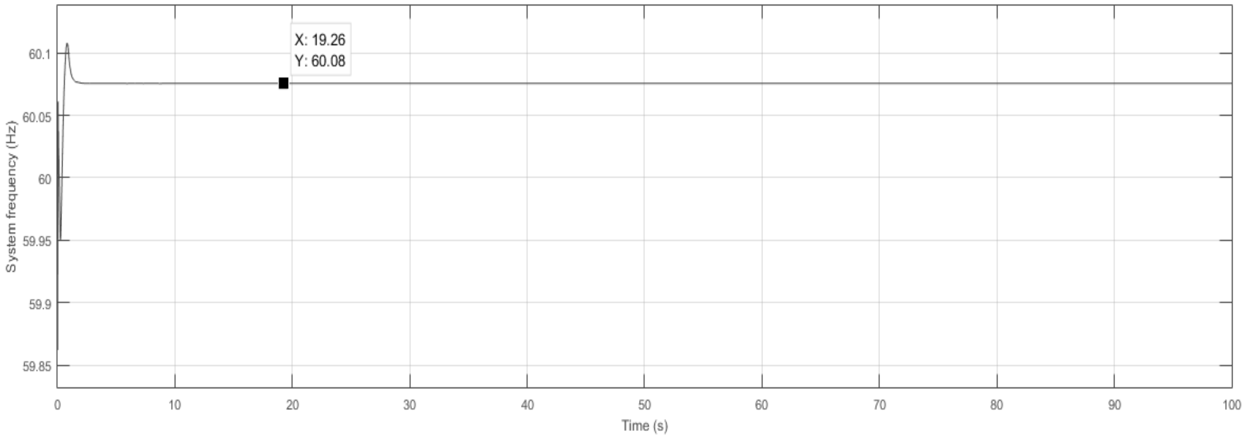

Figure 42. Graph of system frequency versus time under a light load of 0.6 MW.

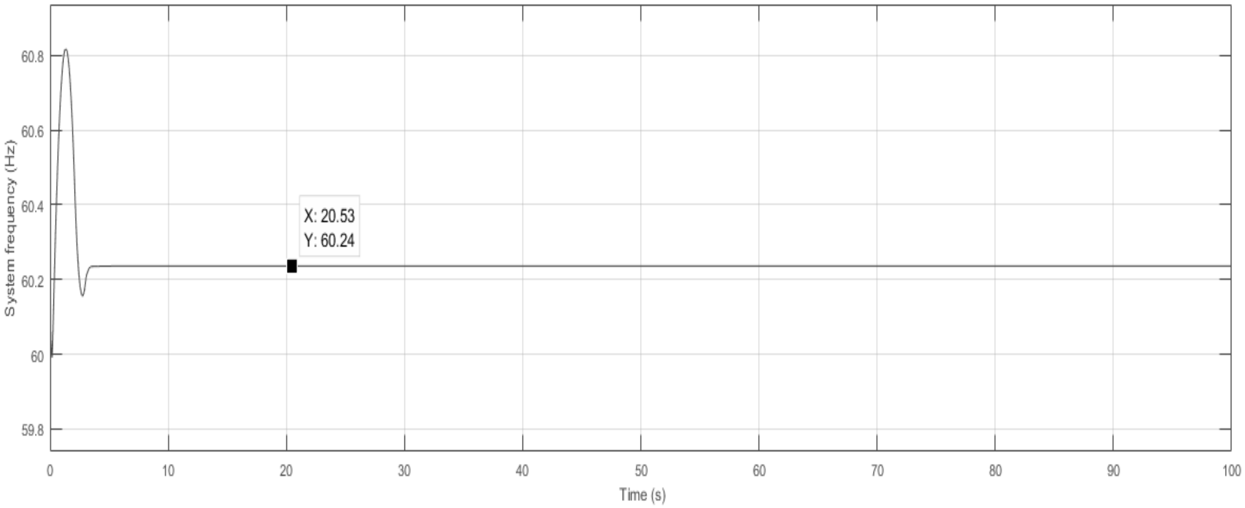

Figure 43. Graph of system frequency versus time under a very light load of 10 kW.

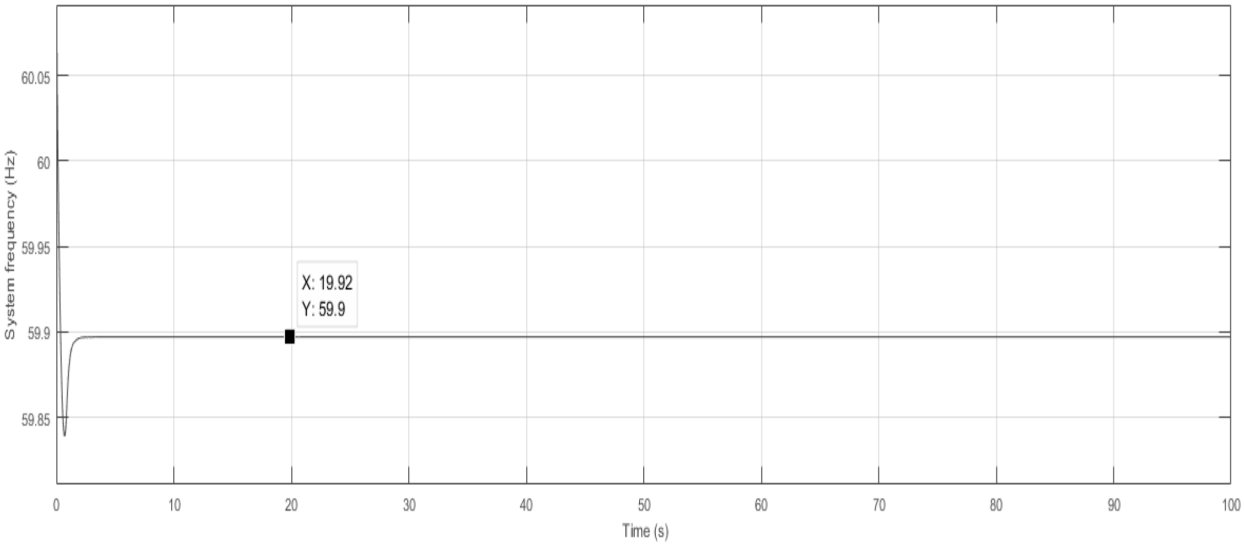

Figure 44. Graph of system frequency versus time when the load is increased to 2 MW.

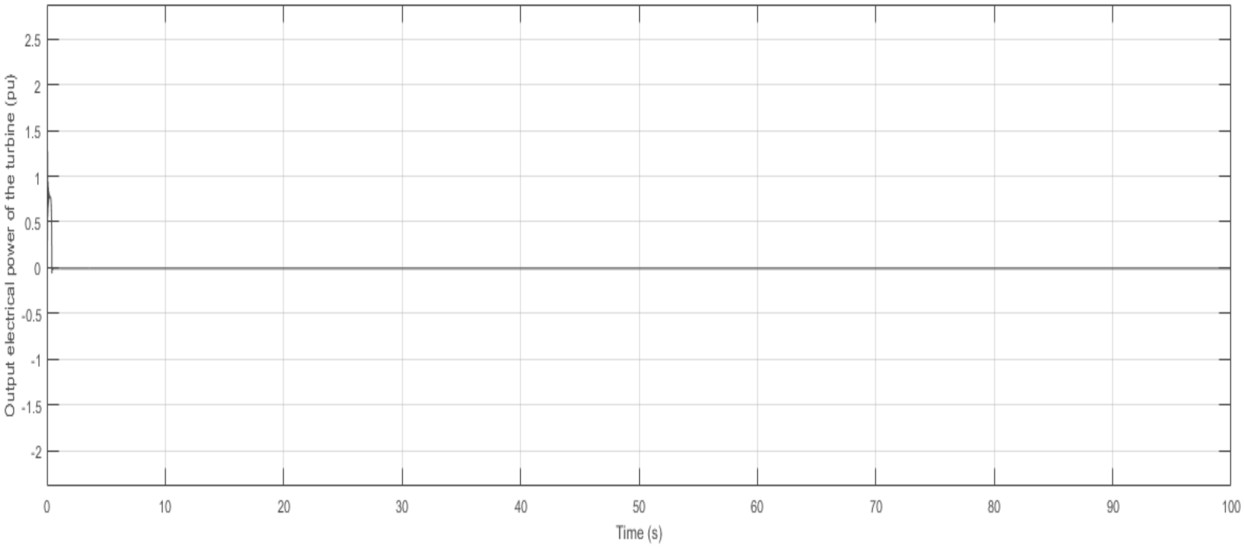

Figure 45. Graph of output electrical power versus time when load = 2 MW.

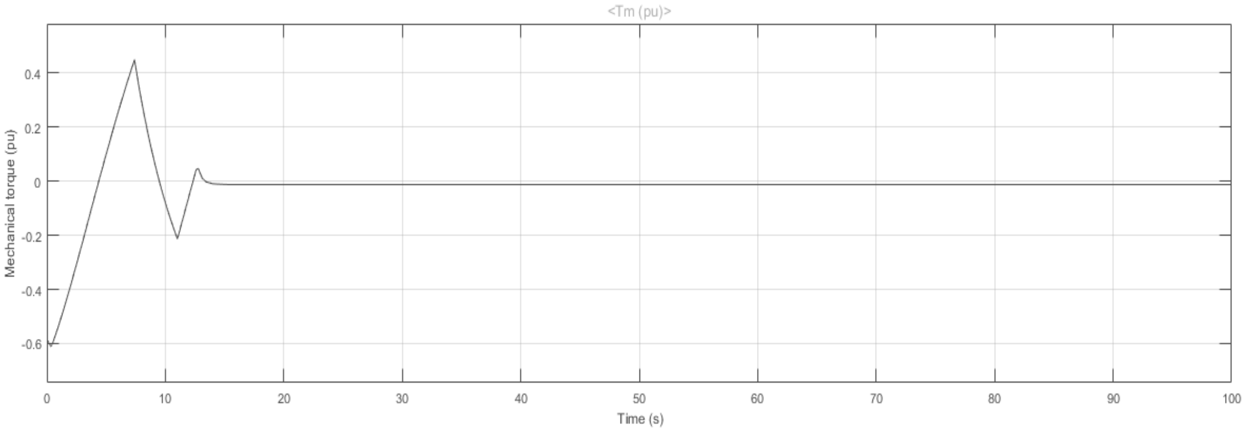

Figure 46. Graph of torque versus time when load = 2 MW.

The turbine power characteristic that is used for the model is shown in Figure 47 below [108].

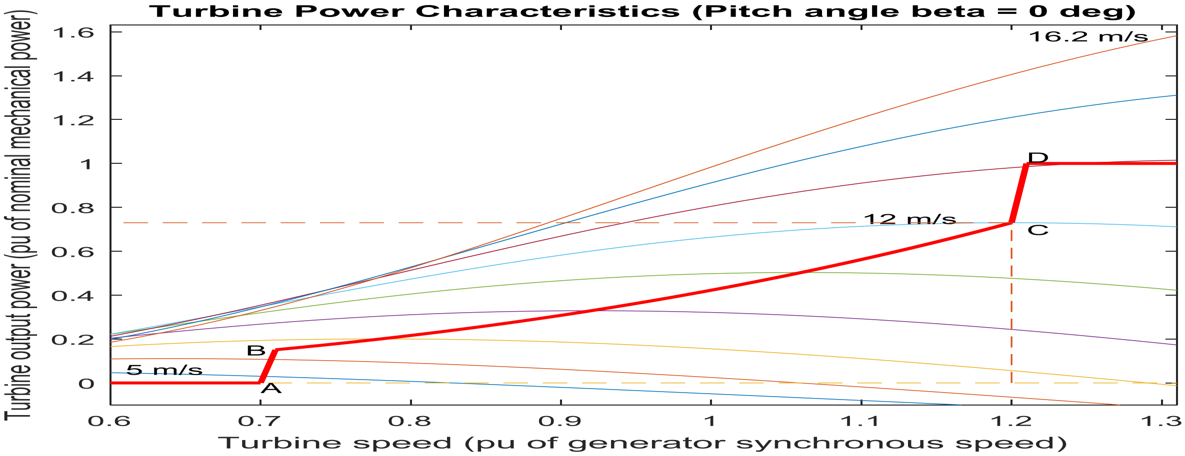

Figure 47. Turbine output power versus speed characteristic.

The Figure above is a clear indication that the turbines produces higher power at higher wind speeds. This is validated by the graph of power output versus time as shown in Figure 48 through 50 under a constant load. It is observed that the output power increased when the speed was increased from 12m/s to 20m/s.

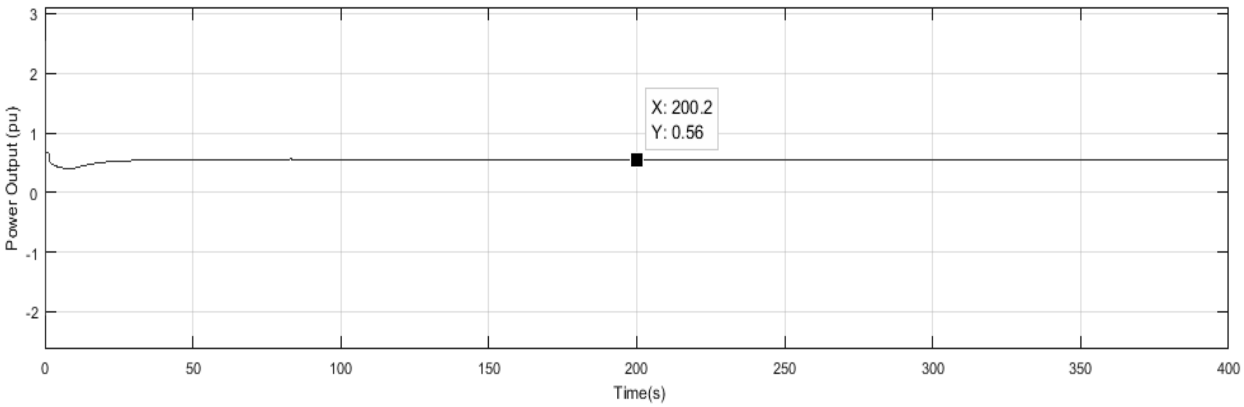

Figure 48. Graph of power output versus time when wind speed = 12m/s.

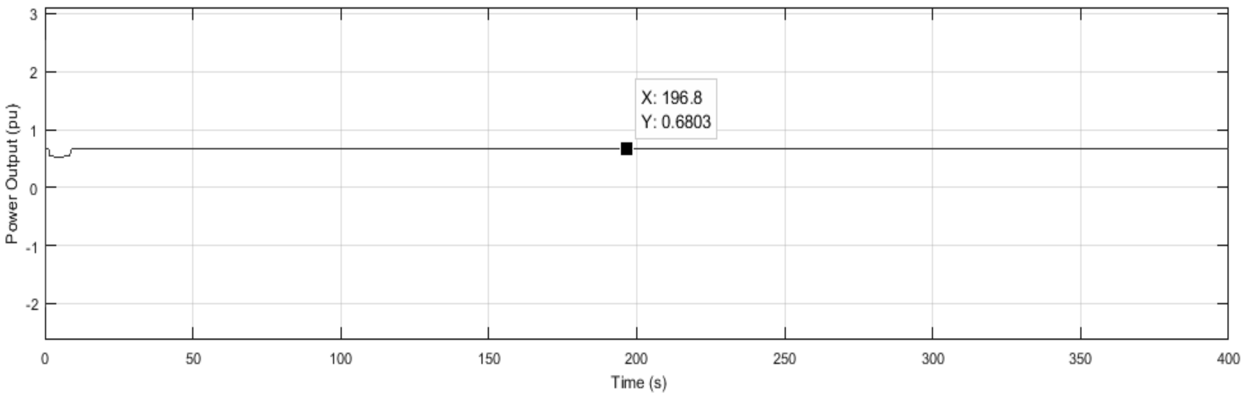

Figure 49. Graph of power output versus time when wind speed =15m/s.

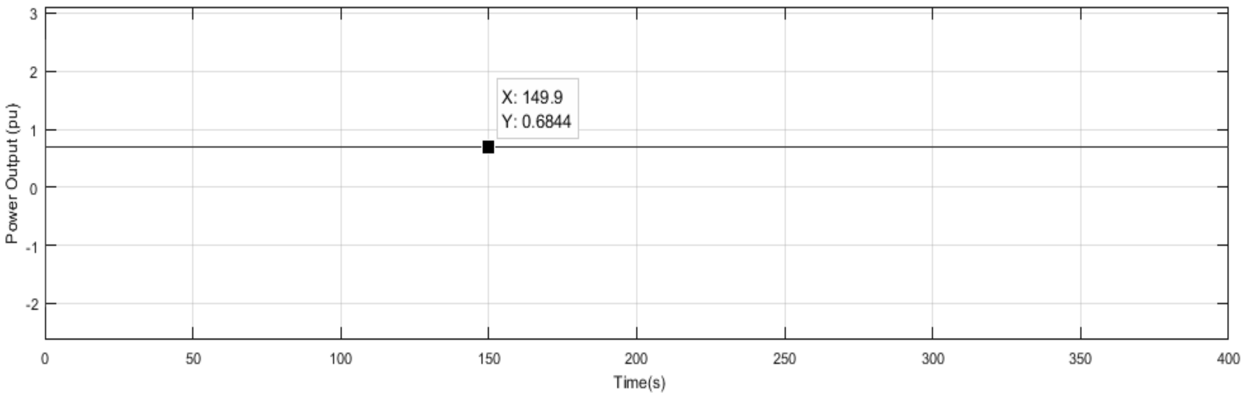

Figure 50. Graph of power output versus time when wind speed = 20m/s.

The simulation diagram in Figure 51 below shows the closed – loop system used to control the frequency of the system.

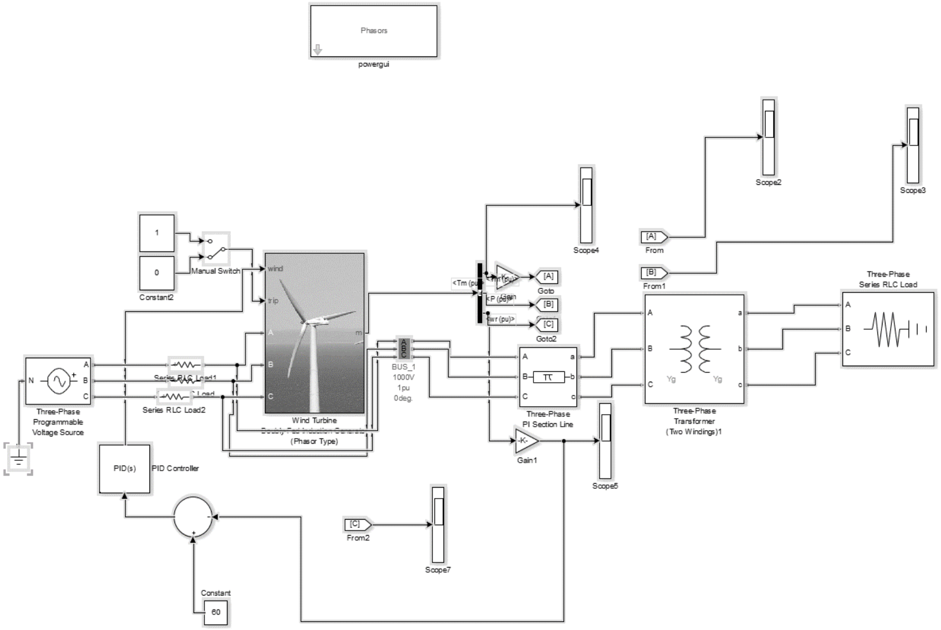

Figure 51. Closed - loop system of the model in MATLAB/Simulink.

5.1 RESULTS AND DISCUSSION

Figures 52 to 69 shows the system frequency, mechanical torque, and turbine mechanical power output versus time when $P_L = 0.85$ MW.

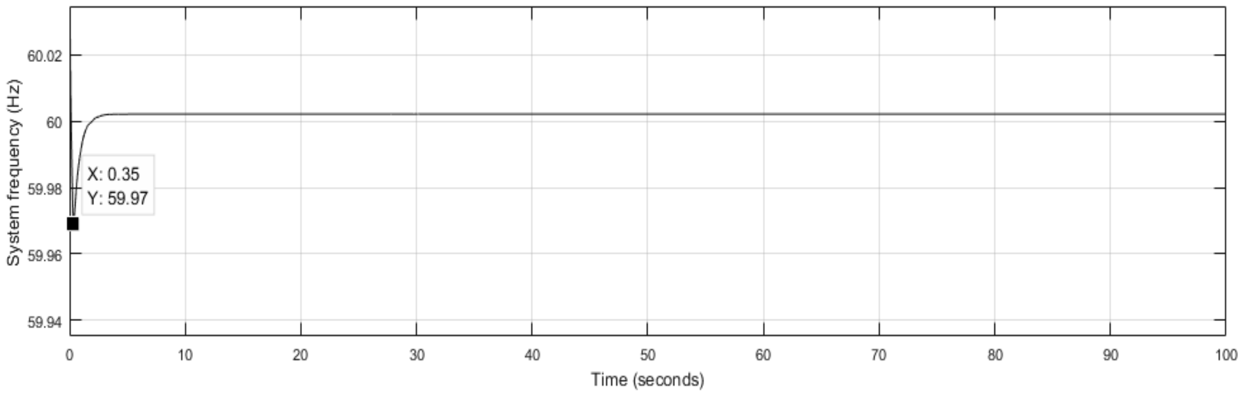

Figure 52. Graph of system frequency versus time when H = 5 s.

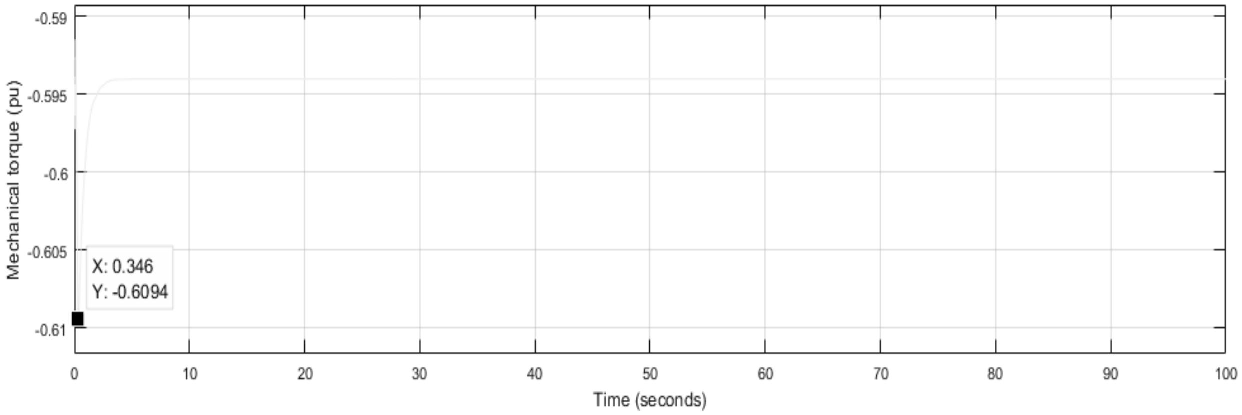

Figure 53. Graph of mechanical torque versus time when H = 5 s.

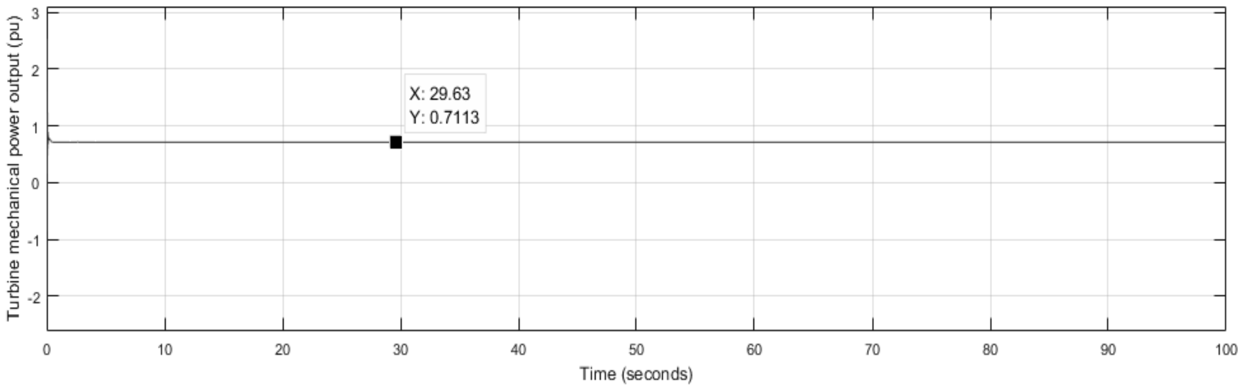

Figure 54. Graph of mechanical power versus time when H = 5 s.

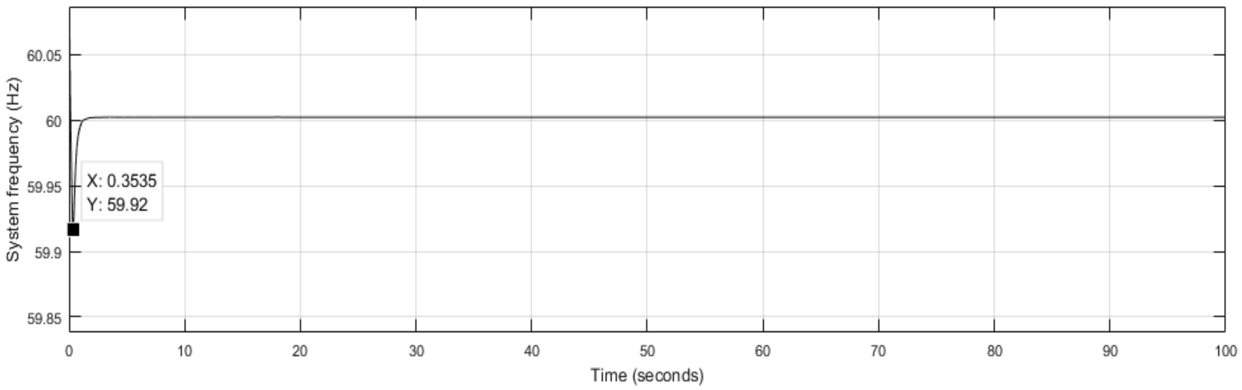

Figure 55. Graph of system frequency versus time when H = 2 s.

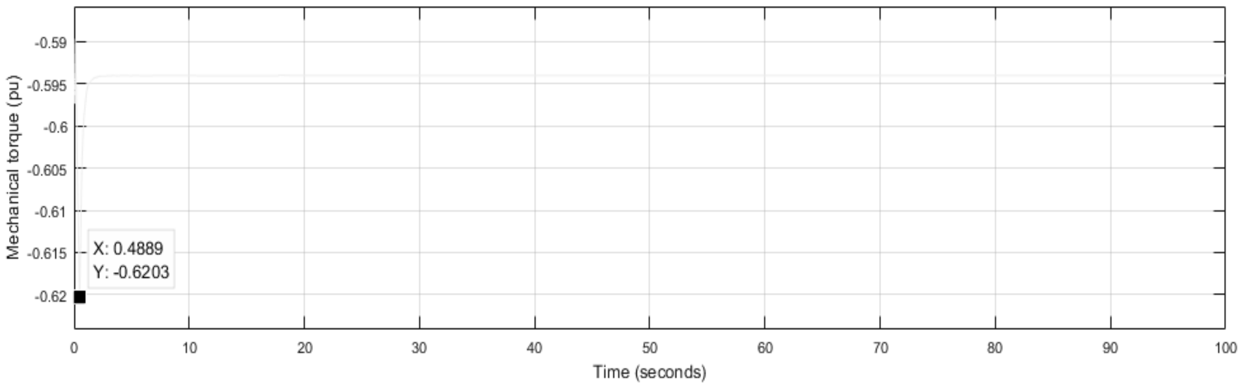

Figure 56. Graph of mechanical torque versus time when H = 2 s.

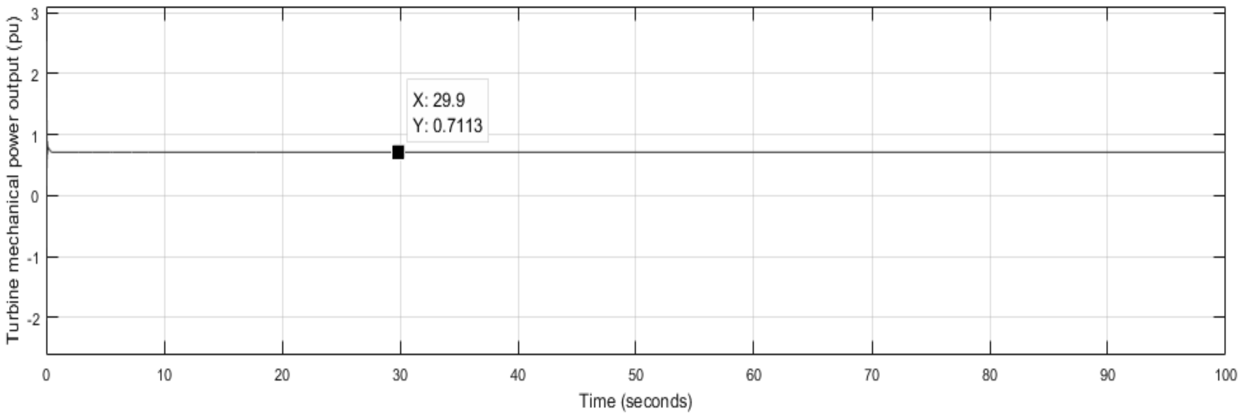

Figure 57. Graph of mechanical power versus time when H = 2 s.

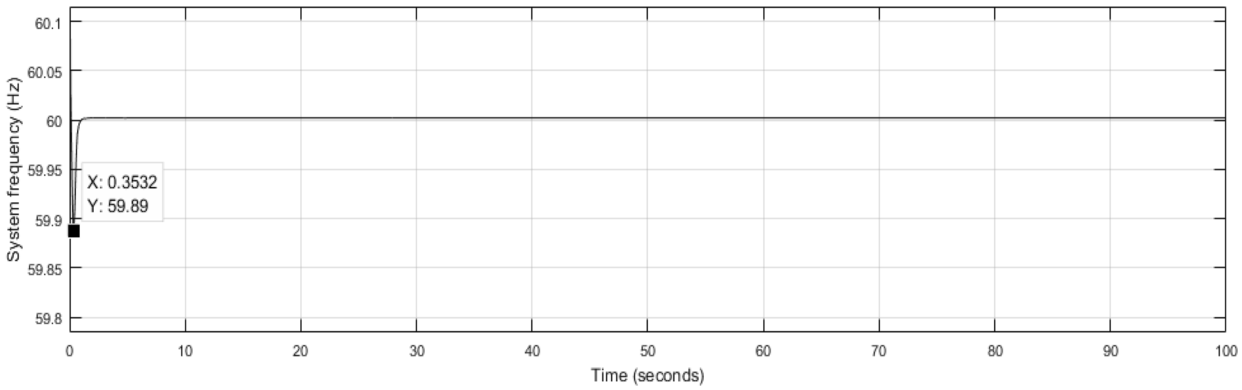

Figure 58. Graph of system frequency versus time when H = 1.5 s.

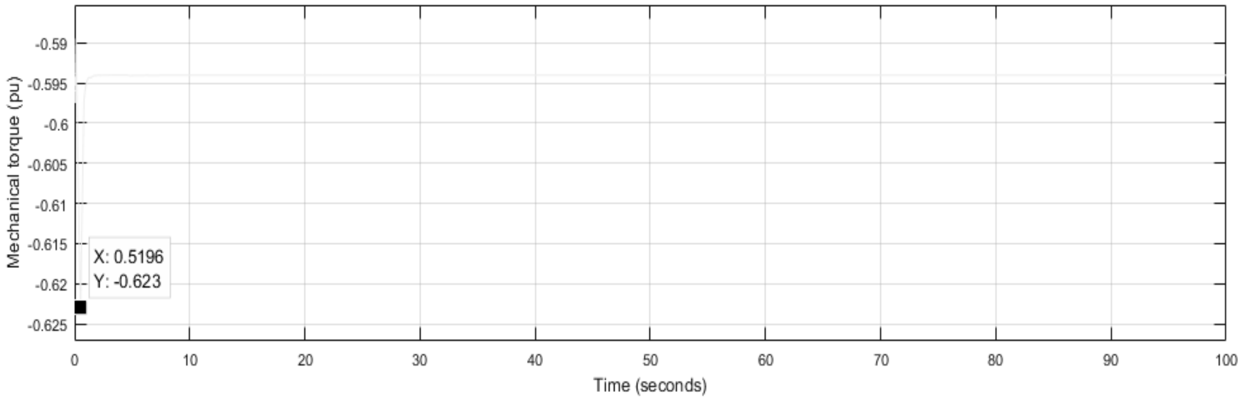

Figure 59. Graph of mechanical torque versus time when H = 1.5 s.

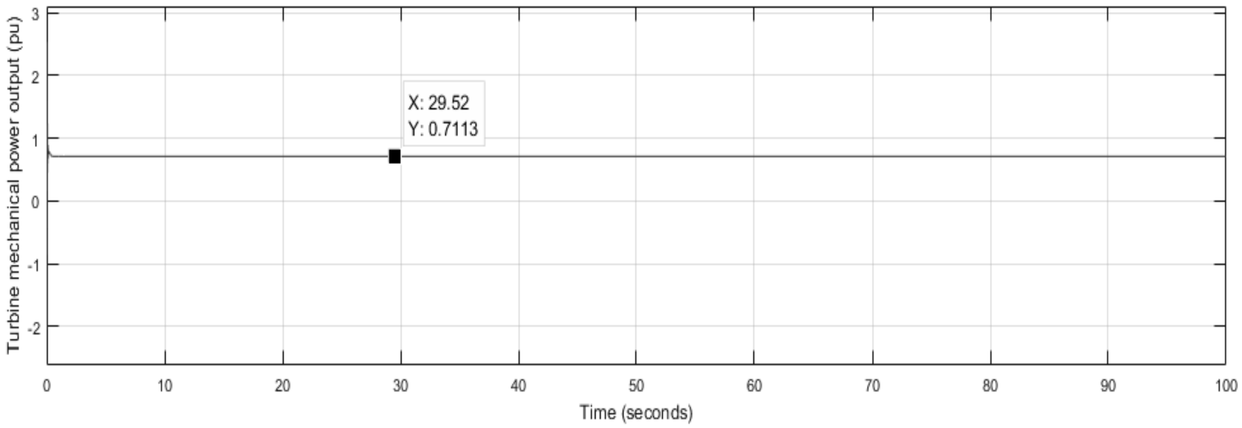

Figure 60. Graph of torque versus mechanical power when H = 1.5 s.

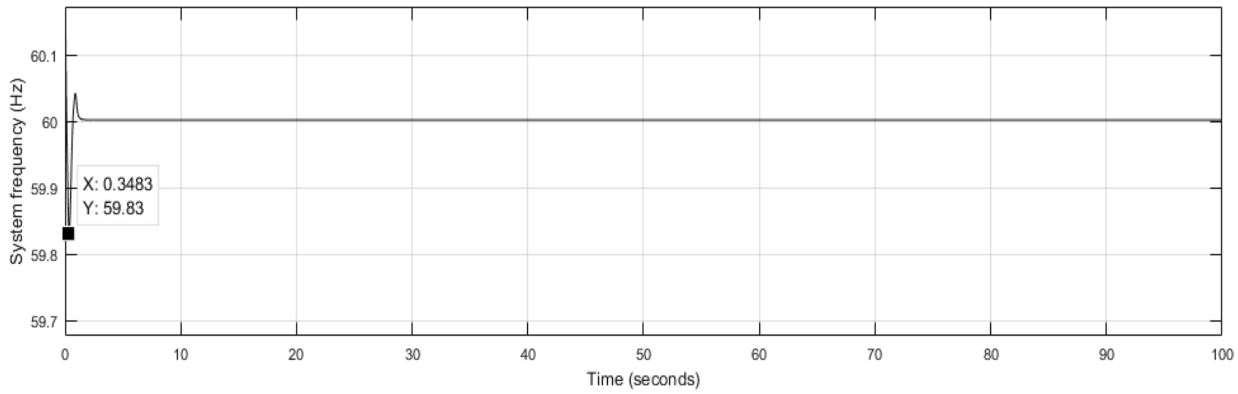

Figure 61. Graph of system frequency versus time when H = 1.0 s.

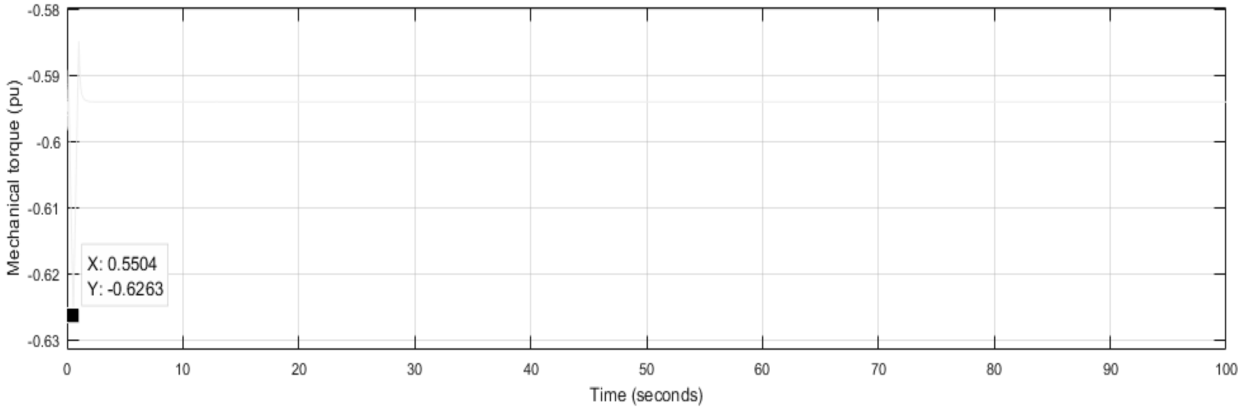

Figure 62. Graph of mechanical torque versus time when H = 1.0 s.

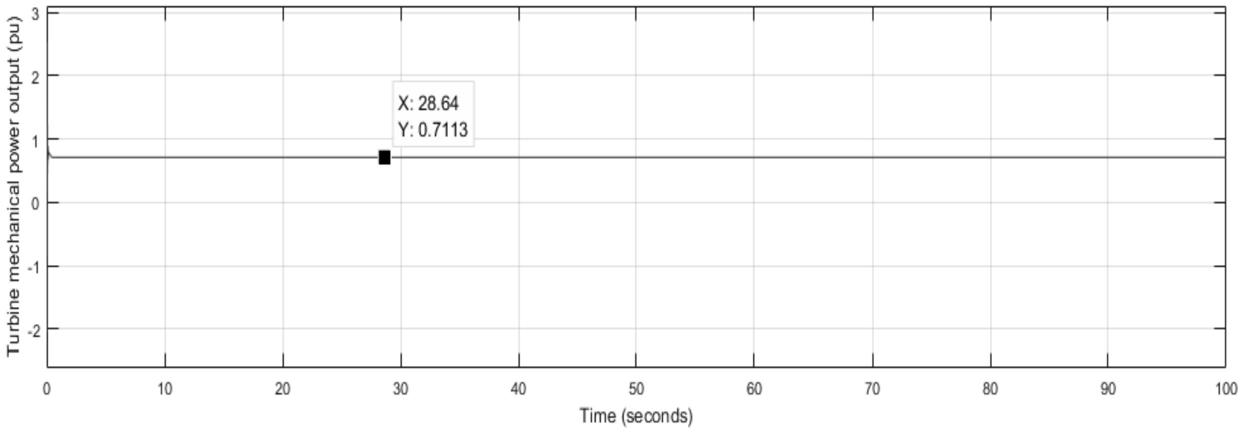

Figure 63. Graph of mechanical power versus time when H = 1.0 s.

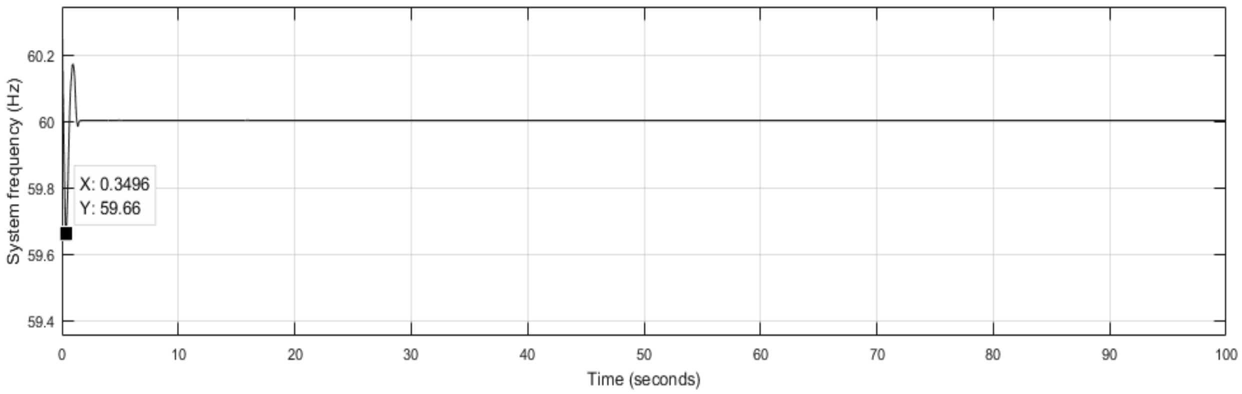

Figure 64. Graph of system frequency versus time when H = 0.5 s.

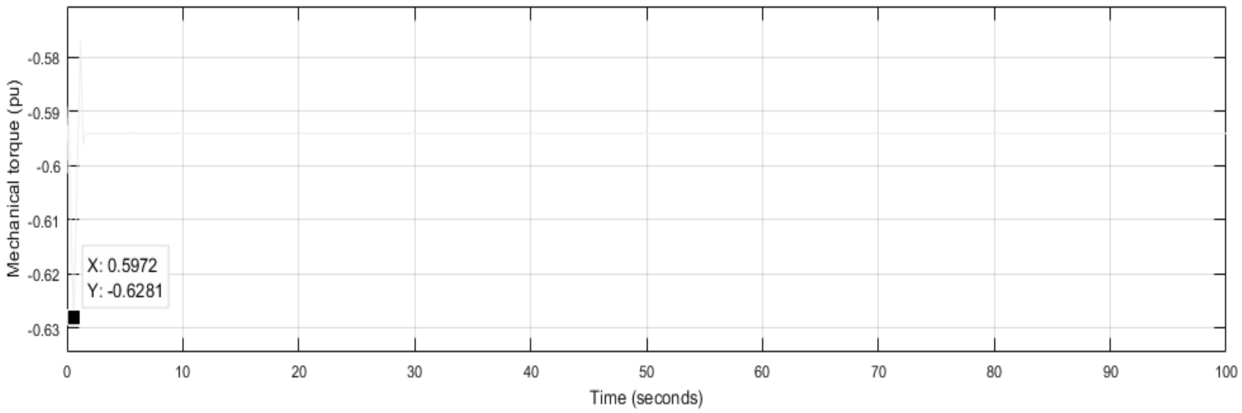

Figure 65. Graph of mechanical torque versus time when H = 0.5 s.

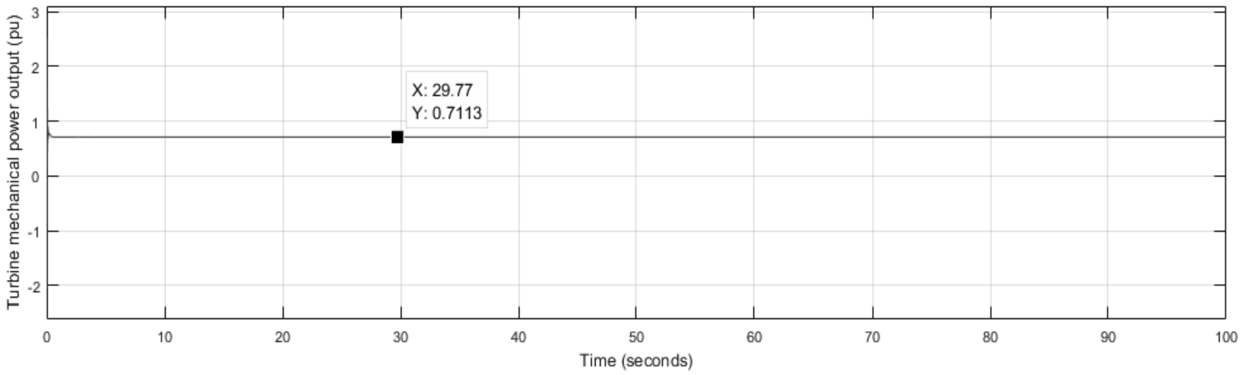

Figure 66. Graph of mechanical power versus time when H = 0.5 s.

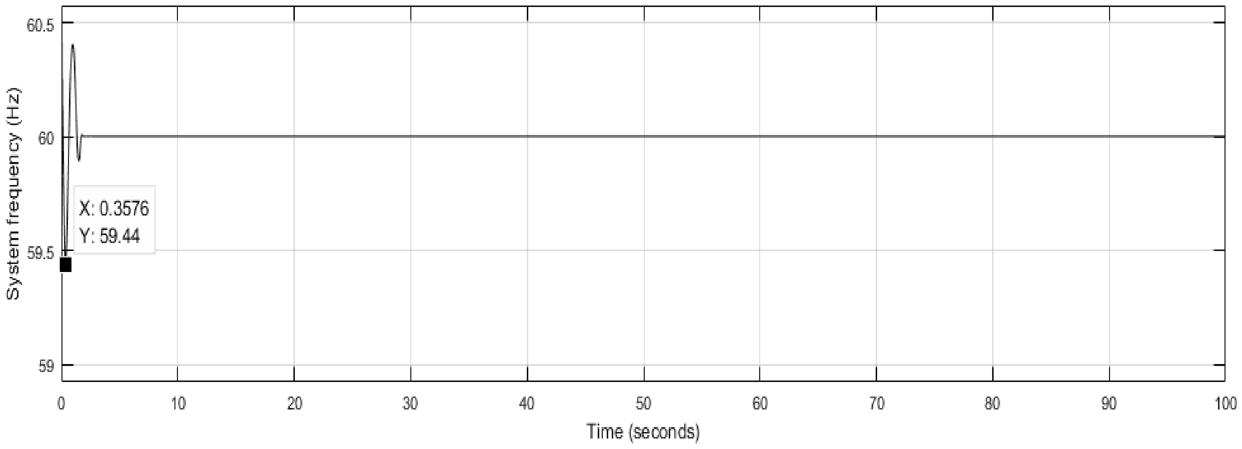

Figure 67. Graph of system frequency versus time when H = 0.3 s.

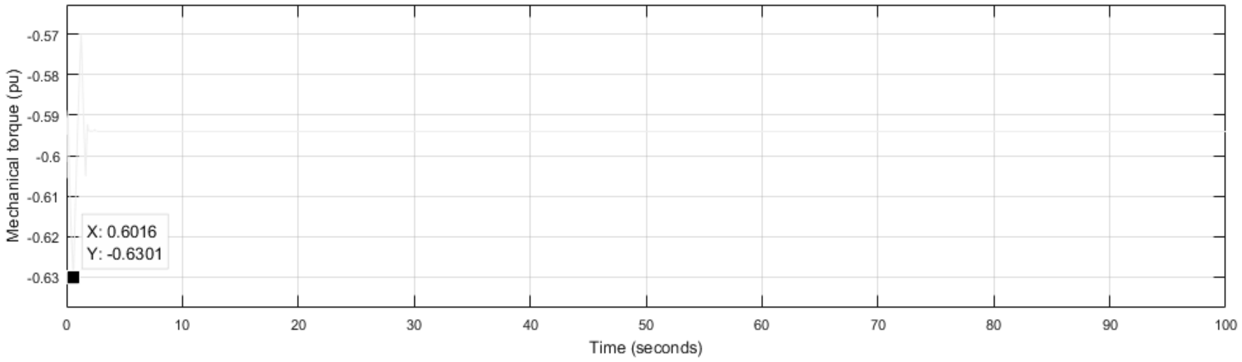

Figure 68. Graph of mechanical torque versus time when H = 0.3 s.

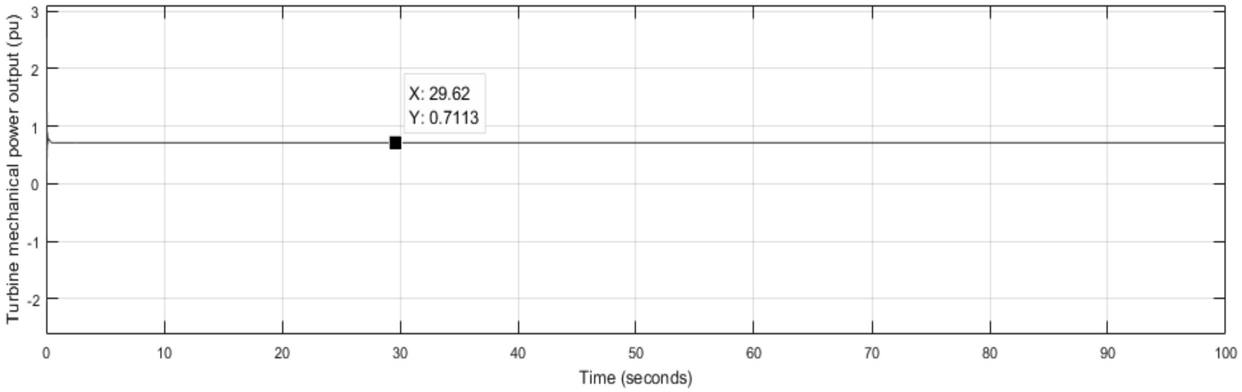

Figure 69. Graph of mechanical power versus time when H = 0.3 s.

Figures 52 through 69 respectively shows that the transient response attains a much larger value and hence lower frequency as the inertia constant decreases. In Figure 52, the system frequency is 59.44 Hz at 0.3576 s. This typical response could shut down a power system within the shortest time possible. The frequency band is expected to be within the ±0.5 Hz limit that is the lower limit should be at 59.5 Hz; any frequency below this can be viewed as non-compliant and could lead to dangerous instability in the system.

Figures 52 through 69 also shows the changes in the mechanical output torque as the inertia constant, H changes. As the inertia constant takes lower values, the value of torque in the transient also decreases further. This means that the machine rotor speed decreases and then rapidly increases to respond to a load change. This type of abnormal behavior can damage the rotor.

Figures 52 through 69 shows the turbine mechanical power output versus time as the inertia constant, H decreases. It can be observed that the turbine mechanical power output remains constant all through. This is because the load demand is constant at 0.85 MW. Hence, the power generated, P_G also remains the same to keep the system frequency at the rated value of 60 Hz.

The turbine mechanical power output value is 0.7113 pu. Since the nominal wind turbine mechanical power output is rated at 1.2 MW.

Hence, the power generated in MW is calculated as:

$P_G = 0.7113 \text{ x } 1.2 \text{ MW}$

$P_G = 0.85$ MW. Therefore $P_G = P_L$.

The ac microgrid was connected to the grid, while the grid was disconnected during the simulation; an external load was also connected and varied as shown in Figure 70. The following results were obtained in Figure 71 and 72.

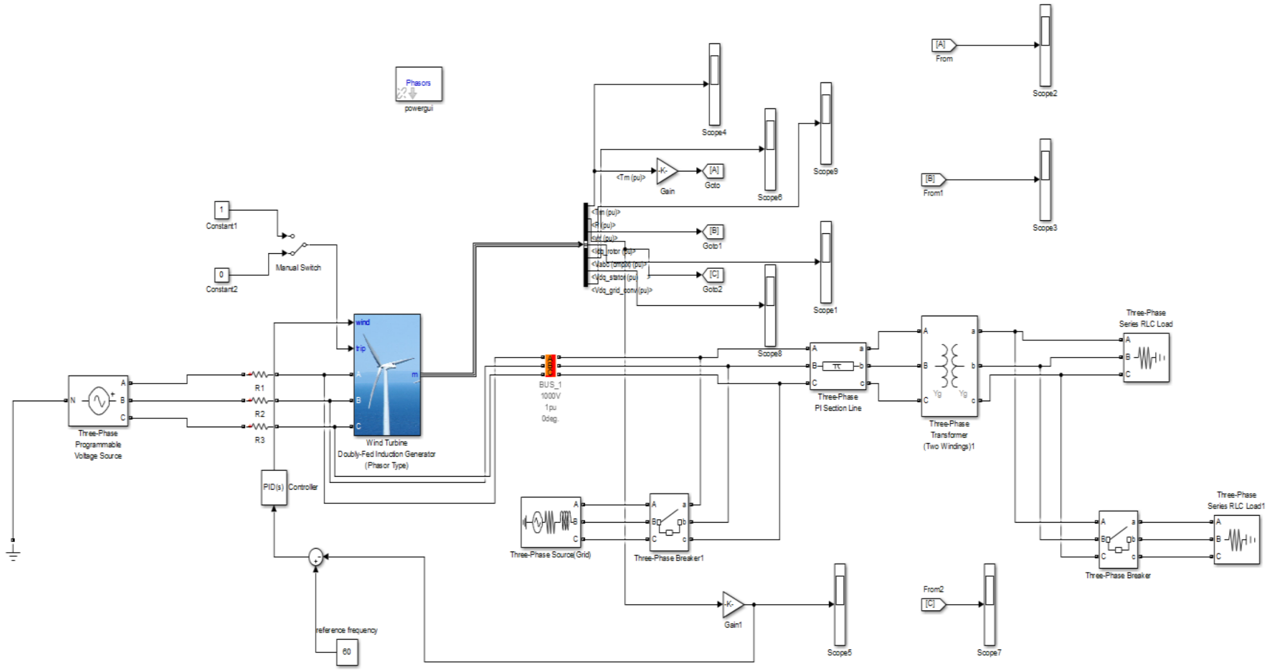

Figure 70. System architecture with varying load and different wind conditions.

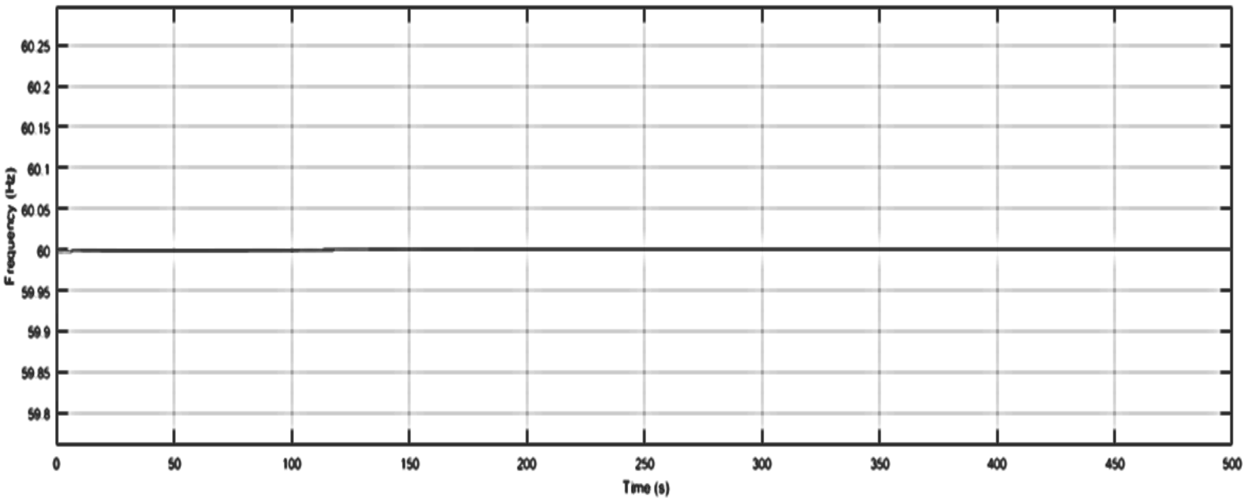

Figure 71. Graph of system frequency versus time using a state controller.

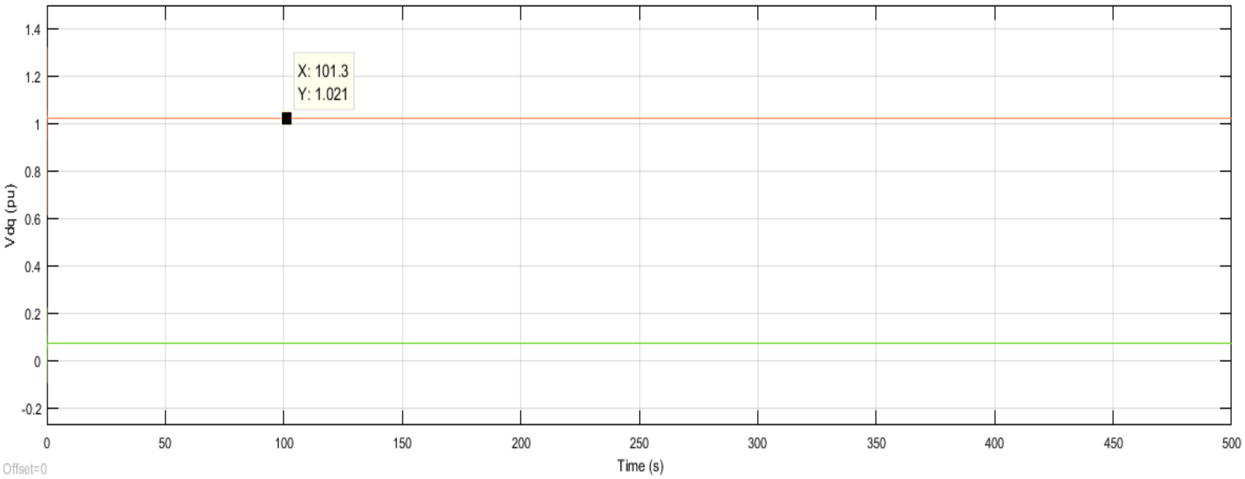

Figure 72. Graph of direct (red) and quadrature (green) axis voltage.

Figure 71 is an indication of the state controller in keeping the system frequency at a steady value of 60 Hz irrespective of the varying wind speeds and load conditions as simulated in Figure 70 in MATLAB/Simulink. This is specifically true for this case.

From Figure 72, V_d = 1.021 pu and V_q = 0.07148 pu.

Therefore, stator voltage, $V_s = \sqrt{{V_d}^2 + V_q}$ (36)

V_s = 1.023 pu.

The stator voltage value of 1.023 p u is obtained which is the grid voltage. This value is also indication of the ability of the state controller to keep the grid voltage at near 1.0 pu during the entire simulation period.

6.0 CONCLUSION

It can be observed that there is stability in the system used for study in this dissertation, where a system frequency of 60 Hz is maintained, also the transient behavior shows that the system frequency decreases within a very short time as the inertia decreases. These results have been able to prove the disadvantage of low inertia in power systems because of deploying many grid-connected wind turbine generation sources. Under varying wind conditions such as speed, the power generated is affected.

The results have been able to prove the contribution of a state controller in improving resilience while allowing for decentralized control and efficient management of the microgrid energy system under extreme conditions. Similarly, load variations can be abrupt. Both effects have impacts on the frequency and voltage stability of a microgrid system, which if it is beyond a certain limit of operation could lead to shut down. During these shutdowns, some part of the load will not receive power whereby characterizing increased downtimes. To mitigate this effect, a method has been proposed to control the microgrid through a state estimation of the microgrid system parameters. During a study of Hurricane Ike, the state controller was employed to increase the resilience of the system. PV sources do not depend on lifelines, and the required DER interface is the inverter, hence, various aspects of this work have proven both experimentally and analytically how the characteristic behavior of PV inverters can influence power system resilience during extreme events. A test was performed on a PV inverter from the results of a wild-fire PV inverter and the characteristic response was send to the state controller to maintain the stability of the system. The PV inverter has a PLL with the capability of measuring the angle and frequency of the grid to implement frequency and voltage ride-through capabilities. The output of the PLL was configured to form one of the states to the state controller to quickly establish the real and reactive power needs of the system during natural disasters.

This work confirms an improvement in the resilience of the microgrid during extreme weather effects using a state controller. The proposed state controller employs the state parameters to coordinate the system operations. A significant contribution of this work lies in the control of the microgrid based on quantifiable resilience metrics by using the state controller.

APPENDIX

Generator:

Nominal power (MW)	1.5
Line-to-line voltage (V)	575
Frequency (Hz)	60
Stator (pu): Rs Lls	0.00706 0.171
Rotor (pu): Rr' Llr'	0.005 0.156
Magnetizing inductance Lm (pu)	2.9
Inertia constant H(s)	0.1 – 10
Friction factor F(pu)	0.01
Pairs of poles p	3
Initial slip, s	-0.25

Turbine:

Nominal wind turbine mechanical power output: 1.2 MW

Tracking speed characteristic [speed_A(pu)….speed_D(pu)]: 0.7 0.71 1.2 1.21

Power at point C (pu/mechanical power): 0.73

Wind speed at point C (m/s): 12

Pitch angle controller gain [Kp]: 500

Maximum pitch angle(deg): 45

Maximum rate of change of pitch angle(deg/s): 2**Converter:**

Converter maximum power(pu)	0.5
Grid side coupling: L(pu) R(pu)	0.15 0.15/100
Coupling inductor initial current: IL(pu) Ph_IL(deg)	0 90
Nominal DC bus voltage (V)	575
DC bus capacitor(F)	10000e-6

Control

Reference grid voltage Vref (pu): 1.0 pu

Grid-side converter generated reactive current reference (Iq_ref) (pu): 0

Grid voltage regulator gains: [Kp Ki]: [1.25 300]

Droop Xs (pu): 0.02

Power regulator gains: [Kp Ki]: [1 100]

DC bus voltage regulator gains: [Kp Ki]: [0.002 0.05]

Grid-side converter current regulator gains: [Kp Ki]: [1 100]

Rotor-side converter current regulator gains: [Kp Ki]: [0.3 8]

Maximum rate of change of reference grid voltage (pu/s): 100

Maximum rate of change of reference power (pu/s): 1

Maximum rate of change of converter reference currents (pu/s): 200

BIBLIOGRAPHY

[1] https://energy.gov/eere/femp/achieving-30-renewable-electricity-use-2025.Accessed January 20, 2017.

[2] http://www.power-technology.com/features/featurethe-worlds-most-used-renewable-power-sources-4160168/. Accessed January 22, 2017.

[3] F. Fuchs, R. Dietz, S. Garske, T. Breithaupt, A. Mertens and L. Hofmann, “Challenges of Grid Integration of Distributed Generation in the Interdisciplinary Research Project Smart Nord,” *in 2014 IEEE 5th International Symposium on Power Electronics for Distributed Generation Systems (PEDG) 2014*, Galway, Ireland.

[4] O. Egbue, D. Naidu, and P. Peterson, “The role of microgrids in enhancing macrogrid resilience,” *2016 Int. Conf. Smart Grid Clean Energy Technol.*, pp. 125–129, 2016.

[5] A. Gholami, F. Aminifar, and M. Shahidehpour, “Front Lines Against the Darkness,” *IEEE Electrif. Mag.*, no. March, pp. 18–24, 2016.

[6] I. E. Outlook, “Industrial sector energy consumption,” pp. 127–140, 2013.

[7] H. Zhang, Z. Hu, and Z. Xu, “Evaluation of Achievable Vehicle-to-Grid Capacity using Aggregate PEV Model,” *IEEE Transactions on Power Systems*, vol. 32, no. 1, pp. 784–794, 2017.

[8] C. S. Holling, “Resilience and stability of ecological systems,” Annu. Rev. Ecol. Systematics, vol. 4, pp. 1–23, 1973.

[9] *U.S. Presidential Policy Directive 21*, accessed on March. 15, 2017.[Online]. Available: https://www.whitehouse.gov/the-press-office/2013/02/12/presidential-policy-directive-critical-infrastructure-securi-Resil

[10] https://www.nytimes.com/2018/08/28/us/puerto-rico-hurricane-maria-deaths.html?partner=google_editors_choice. Accessed September 20, 2018.

[11] A. Kwasinski, “Numerical evaluation of communication networks resilience with a focus on power supply performance during natural disasters,” *2015 IEEE International Telecommunications Energy Conference (INTELEC)*, pp. 85–90, 2015.

[12] A. Kwasinski and A. Kwasinski, “Increasing sustainability and resiliency of cellular network infrastructure by harvesting renewable energy,” *IEEE Commun. Mag.*, vol. 53, no. 4, pp. 110–116, Apr. 2015.

[13] Z. Bie, Y. Lin, G. Li, and F. Li, “Battling the Extreme: A Study on the Power System Resilience,” *Proc. IEEE, IEEE Journals & Mag.* vol. 105, no. 7, pp. 1253–1266, 2017.

[14] N. Yodo, P. Wang, and M. Rafi, “Enabling Resilience of Complex Engineered Systems Using Control Theory,” *IEEE Trans. Reliab.*, vol. PP, no. 99, pp. 1–13, 2017.

[15] M. Panteli and P. Mancarella, “The grid: Stronger, bigger, smarter?: Presenting a conceptual framework of power system resilience,” *IEEE Power Energy Mag.*, vol. 13, no. 3, pp. 58–66, May/Jun. 2015.

[16] A. A. Salam, A. Mohamed, and M. A. Hannan, “Technical Challenges on Microgrids,” *ARPN J. Eng. Appl. Sci.*, vol. 3, no. 6, pp. 64–69, 2008.

[17] B. Mukherjee, M. Habib, and F. Dikbiyik, “Network adaptability from disaster disruptions and cascading failures,” *IEEE Commun. Mag.*, vol. 52, no. 5, pp. 230–238, 2014.

[18] A. Kwasinski, V. Krishnamurthy, J. Song and R. Sharma, “Availability Evaluation of Micro-Grids for Resistant Power Supply During Natural Disasters,” ,” IEEE Trans. Smart Grid, vol. 3, no. 4, pp. 2007–2018, 2012.

[19] A. Kwasinski, “Technology planning for electric power supply in critical events considering a bulk grid, backup power plants, and microgrids,” IEEE Syst. J., vol. 4, no. 2, pp. 167–178, Jun. 2010.

[20] M. R. Vallem et al., "Hybrid cascading outage analysis of extreme events with optimized corrective actions," 2017 19th International Conference on Intelligent System Application to Power Systems (ISAP), San Antonio, TX, USA, 2017, pp. 1-6.

[21] B. Vyakaranam et al., "Novel Additions to DCAT to Analyze What-If Scenarios of Protection Maloperation and Intermittent Resources on Cascading Failures for Extreme Events," 2018 IEEE/PES Transmission and Distribution Conference and Exposition (T&D), Denver, CO, 2018, pp. 1-9.

[22] V. Krishnamurthy and A. Kwasinski, “Effects of Power Electronics , Energy Storage , Power Distribution Architecture and Lifeline Dependencies on Microgrids Resiliency During Extreme Events,” *IEEE J. Emerg. Sel. Top. Power Electron.*, vol. 6777, no. 99, p. 14, 2016.

[23] L. Riachy, S. Member, and Y. Azzouz, “Optimal Power Coefficient For Load Balancing and Reactive Power Compensation In DFIG-WTS*,” IECON 42nd Annual Conference of the IEEE Industrial Electronics Society*, pp. 4199–4204, 2016.

[24] G. Ding, X. Cheng, and H. Wang, “Coordinate Control of Distributed Generation and Power Electronics Loads in Microgrid,” *Proceedings of the 2016 International Conference on Advance Mechaatronics Systems*, pp. 68–72, 2016.

[25] M. Shahidehpour, xindong liu, Z. Li, and Y. Cao, “Microgrids for Enhancing the Power Grid Resilience in Extreme Conditions,” *IEEE Trans. Smart Grid*, vol. 8, no. 2, pp. 1–1, 2016.

[26] M. He and M. Giesselmann, “Reliability-constrained self-organization and energy management towards a resilient microgrid cluster,” *2015 IEEE Power Energy Soc. Innov. Smart Grid Technol. Conf.*, pp. 1–5, 2015.

[27] H. Gao, Y. Chen, Y. Xu, and C. C. Liu, “Resilience-Oriented Critical Load Restoration Using Microgrids in Distribution Systems,” *IEEE Trans. Smart Grid*, vol. 7, no. 6, pp. 2837–2848, 2016.

[28] H. Farzin, M. Fotuhi-Firuzabad, and M. Moeini-Aghtaie, “Enhancing Power System Resilience Through Hierarchical Outage Management in Multi-Microgrids,” *IEEE Trans. Smart Grid*, vol. 7, no. 6, pp. 2869–2879, 2016.

[29] R. Eskandarpour, H. Lotfi, and A. Khodaei, “Optimal microgrid placement for enhancing power system resilience in response to weather events,” *NAPS 2016 - 48th North Am. Power Symp. Proc.*, 2016.

[30] A. Gholami, T. Shekari, F. Aminifar, and M. Shahidehpour, “Microgrid Scheduling with Uncertainty: The Quest for Resilience,” *IEEE Trans. Smart Grid*, vol. 7, no. 6, pp. 2849–2858, 2016.

[31] R. Eskandarpour, G. Edwards, and A. Khodaei, “Resilience-constrained unit commitment considering the impact of microgrids,” *2016 North Am. Power Symp.*, pp. 1–5, 2016.

[32] E. Pashajavid, F. Shahnia, and A. Ghosh, “Development of a self-healing strategy to enhance the overloading resilience of islanded microgrids,” *IEEE Trans. Smart Grid*, vol. PP, no. 99, pp. 868–880, 2015.

[33] C. Buque, “Distributed Generation and Microgrids for Improving Electrical Grid Resilience : Review of the Mozambican Scenario,” pp. 1–5, 2016.

[34] L. Liang, Y. Hou, D. Hill, and S. Y. R. Hui, “Enhancing Resilience of Microgrids with Electric Springs,” *IEEE Trans. Smart Grid*, vol. PP, no. 99, 2016.

[35] Xinda Ke, Renke Huang, Mallikarjuna Vallem, Jesse Holzer, Nader Samaan, Yuri Makarov, Marcelo Elizondo, Bharat Vyakaranam, Siddharth Sridhar, “A Three-Stage Enhanced Reactive Power and Voltage Optimization Method for High Penetration of Solar,” *2017 IEEE Power & Energy Society General Meeting*, Chicago, July 2017

[36] Xinda Ke and R. Blum, "Optimum quantization and reconstruction of power flows from voltage measurements at dispersed buses," *2012 IEEE 7th Sensor Array and Multichannel Signal Processing Workshop (SAM)*, Hoboken, NJ, 2012, pp. 469-472.

[37] Marcelo A. Elizondo, Nader Samaan, Yuri V.Makarov, Jesse Holzer, Mallikarjuna Vallem, Renke Huang, Bharat Vyakaranam, Xinda Ke, and Feng Pan, “Literature Survey on Operational Voltage Control and Reactive Power Management on Transmission and Sub-Transmission Networks,” *2017 IEEE Power & Energy Society General Meeting*, Chicago, July 2017.

[38] N. Samaan et al., "Combined Transmission and Distribution Test System to Study High Penetration of Distributed Solar Generation," 2018 IEEE/PES Transmission and Distribution Conference and Exposition (T&D), Denver, CO, 2018, pp. 1-9.

[39] S. Bae and A. Kwasinski, “Dynamic Modeling and Operation Strategy for a Microgrid with Wind and Photovoltaic Resources,” IEEE Trans. Smart Grid, vol. 3, no. 4, pp. 1867–1876, 2012.

[40] J. Song, V. Krishnamurthy and A. Kwasinski, "Development of a Markov-Chain-Based Energy Storage Model for Power Supply Availability Assessment of Photovoltaic Generation Plants," IEEE Trans. on Sustainable Energy,vol. 4, no. 2, pp. 491–500, 2013.

[41] https://www.pplelectric.com/~/media/pplelectric/at%20your%20service/docs/remsi/metering-equipment-tables/grid-tied-inverter-guide.pdf. Accessed October 18, 2017.

[42] O. J. Aworo and J. Shek, "Transformer for contactless electric vehicle charging with bidirectional power flow," *in 2017 IEEE Power & Energy Society General Meeting,* July 2017, Chicago, IL, USA.

[43] M. B. Anurag, G. S. Thrinath, S. B. Karanki, and R. Yallamili, "Design of ZVS based high gain DC-DC converter for PV applications," *in 2016 IEEE 6th International Conference on Renewable Energy Research and Applications (ICRERA),* pp. 584 – 589, 2016.

[44] N. Chellammal, R. C. Ilambirai, S. SekharDash, and K.V. Rahul, "Integration of renewable energy resources in off GRID system using three port zeta converter," *in 2016 IEEE 6th International Conference on Renewable Energy Research and Applications (ICRERA),* pp. 971 – 976, 2016.

[45] A. Q. Huang, S. Bhattacharya, M. Baran, B. Chen, and C. Han, "Active Power Management of Electric Power System Using Emerging Power Electronics Technology," *in 2007 IEEE Power Engineering Society General Meeting,* July 2007, Tampa, FL, USA.

[46] A. Kwasinski, "Advanced power electronics enabled distribution architectures: Design, operation, and control," *in 8th International Conference on Power Electronics* - ECCE Asia, June 2011, Jeju, South Korea.

[47] W. T. Kuo, Y. C. Hsu, C. W. Liu, Y. M. Chen, and H. L Huang, "The Current Control of PV Inverter for Three-Phase Unbalanced Fault with Lagrange Multiplier," *in 2013 International Future Energy Electronics Conference (IFEEC*), pp. 510–514, 2013.

[48] E. Afshari, G. R. Moradi, R. Rahimi, B. Farhangi, Y. Yang, F. Blaabjerg, and S. Farhangi, "Control Strategy for Three-Phase Grid-Connected PV Inverters Enabling Current Limitation Under Unbalanced Faults," *IEEE Transactions on Industrial Electronics,* vol. 64, no. 11, pp. 8908–8918, 2017.

[49] H. Xiong, X. Du, P. Sun, and Y. Ji, "An Optimized Active Power Control Method of Two-Stage Grid-Connected Photovoltaic Inverter Under Unbalanced Grid Faults*," in 43rd Annual Conference of the IEEE Industrial Electronics Society (IECON),* pp. 817-822, 2017.

[50] M. Dong, H. Dong, L. Wang, J. Yang, L. Li, and Y. Wang, "A simple open-circuit detection strategy for a single-phase grid-connected PV inverter fed from power optimizers*," IEEE Trans. on Power Electronics,* vol.33, no. 4, pp. 2798-2802, 2018.

[51] F.Viola, M.C. Di Piazza, and G. Vitale, "Evaluation of Ground Currents in a PV System with High Frequency Modeling," *in International Journal of Renewable Energy Research (IJRER),* vol. 8, no. 3, pp. 1770-1778, 2018.

[52] A. Kowsar and S. Farid Uddin Farhad, "High Efficiency Four Junction III-V Bismide Concentrator Solar Cell: Design, Theory, and Simulation," *in International Journal of Renewable Energy Research (IJRER),* vol. 8, no. 3, pp. 1762-1769, 2018.

[53] R.F. Khelifa and K. Jelassi, "A Smart Control System For Solar Photovoltaic Power Supply In Rural Africa*," in International Journal of Renewable Energy Research (IJRER),* vol. 8, no. 3, pp. 1718-1728, 2018.

[54] N. Pachaivannan, "Cost Effective Solitary Stage Single Phase Inverter for Solar PV Integration in to Grid*," in International Journal of Renewable Energy Research (IJRER),* vol. 8, no. 3, pp. 1309-1317, 2018.

[55] O. A. Ajeigbe, S. P. Chowdhury, T. O. Olwal, and A. M. Abu-Mahfouz, "Harmonic Control Strategies of Utility-Scale Photovoltaic Inverters*," in International Journal of Renewable Energy Research (IJRER),* vol. 8, no. 3, pp. 1354-1368, 2018.

[56] A. Mojallal, and S. Lotfifard, 'Enhancement of Grid Connected PV Arrays Fault Ride Through and Post Fault Recovery Performance," *IEEE Transactions on Smart Grid*, vol.10, no. 99, pp. 1-10, 2017.

[57] H. Zhao, N. Wu, S. Fan, Y. Gao, L. Liu, Z. Zhao, and X. Liu, "Research on Low Voltage Ride Through Control of PV Grid-Connected Inverter Under Unbalance Fault*," in 2017 Chinese Automation Congress (CAC)*, vol. 86, no. 532.

[58] G. Ding et al., "Adaptive dc-link voltage control of two-stage photovoltaic inverter during low voltage ride-through operation," *IEEE Trans. Power Electron.*, vol. 31, no. 6, pp. 4182–4194, Jun. 2016.

[59] W. L. X. Guo, X. Zhang, X. Sun, Z. Lu, and J. M. Guerrero, "Flexible control strategy for grid-connected inverter under unbalanced grid faults without PLL," *IEEE Trans. Power Electron.,* vol. 30, no. 4, pp. 1773–1778, Apr. 2015.

[60] https://standards.ieee.org/standard/519-2014.html. Accessed September 11, 2018.

[61] S. S. Rangarajan , E. R. Collins, and J. C. Fox, "Detuning of harmonic resonant modes in accordance with IEEE 519 standard in an exemplary north american distribution system with PV and wind," *in 2017 IEEE 6th International Conference on Renewable Energy Research and Applications (ICRERA),* pp. 435 – 440, 2017.

[62] U. Sangpanich, “A novel method of decentralized battery energy management for stand-alone PV-battery systems,” *in 2014 IEEE PES Asia-Pacific Power and Energy Engineering Conference (APPEEC),* December 2014, Hong Kong, China.

[63] D. Sutanto, “Power management solutions for energy management, power quality and environment using battery energy storage systems,” *in proceedings of the IEEE 1999 International Conference on Power Electronics and Drive Systems. PEDS'99 (Cat. No.99TH8475),* vol. 1, pp 15, 1999.

[64] S. Bayhan, Y. Liu, and S. Demirbas, “A novel parallel control for modular energy storage system achieving high performance, redundancy and applicability,” *in 2017 IEEE 6th International Conference on Renewable Energy Research and Applications (ICRERA),* pp. 64 – 69, 2017.

[65] T. Sakagami, Y. Shimizu, and H. Kitano, “Exchangeable batteries for micro EVs and renewable energy,” *in 2017 IEEE 6th International Conference on Renewable Energy Research and Applications (ICRERA),* pp. 701 – 705, 2017.

[66] A. Kwasinski, “Local Energy Storage as a Decoupling Mechanism for Interdependent Infrastructures,” in Proc. 2011 IEEE International Systems Conference, pp. 435-441.

[67] J. Esch, “Prolog to Keeping the Energy Debate Clean: How Do We Supply the World's Energy Needs?,” *in Proceedings of the* ***IEEE Journals & Magazines*****, vol. 98, no. 1, pp. 39-41, 2010.**

[68] A. Zahedi, “Renewable energy-based power system to supply reliable electricity for remote applications,” *in proc. 2008 Australasian Universities Power Engineering Conference,* pp. 1-4, December 2008.

[69] P. Buchana and T.S. Ustun, “The Role of Microgrids & Renewable Energy in Addressing Sub-Saharan Africa’s Current and Future Energy Needs,” *in Proc. Renewable Energy Congress (IREC), 2015 6th International,* pp. 1-6, March 2015.

[70] https://www.pplelectric.com/~/media/pplelectric/at%20your%20service/docs/remsi/g-equipment-tables/grid-tied-inverter-guide.pdf. Accessed October 18, 2017.

[71] http://www.nerc.com/docs/pc/ivgtf/GEN-FRT-Stage1-Lit-review%20(2-4Task%20Force).pdf. Accessed October 18, 2017.

[72] A. Mojallal, and S. Lotfifard, ‘Enhancement of Grid Connected PV Arrays Fault Ride Through and Post Fault Recovery Performance,” *IEEE Transactions on Smart Grid,* vol.10, no. 99, pp. 1-10, 2017.

[73] Q. Wang, X. Wang, M. Ding, and Q. Yin, “A Novel Design Method of Digital Phase-locked Loop Applied to Three-Phase Rectifier,” *in proc. of the 36th Chinese Control Conference*, pp. 9244–9248, July 2017.

[74] C. Zhan, C. Fitzer, V. K. Ramachandaramurthy, A. Arulampalam, M. Barnes, and N. Jenkins, “Software phase-lock loop applied to dynamic voltage restorer (DVR),” *in Proceedings of Power Engineering Society Winter Meeting*, 2001: 1033–1038.

[75] S. Chung, “A Phase Tracking system for three phase utility interface inverters,” *IEEE Transactions on Power Electronics*, 15(3):431-438, May 2000.

[76] W. Qiu, J. Xiang, and J. Yu, “An Islanding Detection based on Virtual Impedance and Phase-Locked Loop,” *in proc. of the 36th Chinese Control Conference*, pp. 10553–10558, July 2017.

[77] Y. Song, and F. Blaabjerg, “Analysis of Middle Frequency Resonance in DFIG System Considering Phase-Locked Loop*,” IEEE Transactions on Power Electronics*, vol. 33, no. 1, pp. 343–356, January 2018.

[78] Best, Roland E. *Phase-Locked Loops: Design, Simulation and Applications*. 6th ed., McGraw-Hill, 2007.

[79] *Western Wind and Solar Integration Study Phase 3: Frequency Response and Transient Stability*. NREL. National Renewable Energy Laboratory, Dec. 2014.

[80] Distributed Energy Resources – Connection Modeling and Reliability Considerations, NERC, North American Electric Reliability Corporation, Feb. 2017, available at: http://www.nerc.com/comm/Other/essntlrlbltysrvcstskfrcDL/Distributed_Energy_Resources_Report.pdf

[81] *Composite Load Model for Dynamic Simulations.* WECC Modeling and Validation Work Group. Western Electricity Coordinating Council. Report 1.0: Jun. 12, 2012.

[82] *WECC Specifications for Modeling Distributed Generation in Power Flow and Dynamics.* WECC Renewable Energy Modeling Task Force, and WECC Load Modeling Task Force. Western Electricity Coordinating Council, Feb. 27, 2015.

[83] B. Mather and F. Ding, "Distribution-Connected PV's Response to Voltage Sags at Transmission-Scale," in proc. IEEE Photovolt. Spec. Conf., Portland, OR, Jun. 5-10, 2016.

[84] J. C. Boemer, E. Vittal, M. Rylander, B. Mather, “Derivation of WECC Distributed PV System Model Parameters from Quasi-Static Time-Series Distribution System Simulations,” in proc. IEEE PES Gener. Meet., Chicago, IL, Jul. 16-20, 2017.

[85] NERC Standard for Generator Frequency and Voltage Protective Relay Settings, NERC Std. PRC-024-2, available at: http://www.nerc.com / pa/Stand/Reliability%20Standards/PRC-024-2.pdf

[86] IEEE Standard for Interconnecting Distributed Resources with Electric Power Systems, IEEE Std. 1547-2003, Jul., 28, 2003.

[87] *1200 MW Fault Induced Solar Photovoltaic Resource Interruption Disturbance Report*, NERC, North American Electric Reliability Corporation, Jun. 2017, available at: http://www.nerc.com/pa/rrm/ea/1200_MW_Fault_Induced_Solar_Photovoltaic_Resource_/1200_MW_Fault_Induced_Solar_Photovoltaic_Resource_Interruption_Final.pdf

[88] D. M. Piper, D. L. Donaldson, "Response of Grid Interconnected Solar PV to Transmission System Faults," in proc. IEEE Photovolt. Spec. Conf., Washington, DC, June 25-30, 2017.

[89] A. Kwasinski, "Effects of notable natural disasters from 2005 to 2011 on telecommunications infrastructure: Lessons from on-site damage assessments," in *Proc. INTELEC*, Oct. 2011, pp. 1–9.

[90] L. Dueñas-Osorio and A. Kwasinski, "Quantification of lifeline system interdependencies after the 27 February 2010 Mw 8.8 Offshore Maule, Chile, earthquake," *Earthquake Spectra*, vol. 28, no. S1, pp. S581–S603, 2012.

[91] *TCLEE Report of the 11 March 2011 Mw 9.0 Tohoku, Japan Earthquake and Tsunami*, Amer. Soc. Civil Eng., TCLEE Tech. Council Lifeline Earthquake Eng., Reston, VA, USA, 2012.

[92] http://www.egr.msu.edu/~khalil/NonlinearControl/Slides-Full/Lect_11.pdf.

[93] http://www.cds.caltech.edu/archive/help/uploads/wiki/files/237/Lecture2_notes_CDS270.pdf.

[94] Kwasinski, A. 'Quantitative Model and Metrics of Electrical Grids' Resilience Evaluated at a Power Distribution Level. Energies 2016, 9, 93.

[95] "Dynamic paradigm for grid operations," Pacific Northwest National Laboratory, 2014 Advanced Grid Modeling Peer Review Project Summary, U.S. Department of Energy, October 2014.

[96] S. M. Nosratabadi, R.-A. Hooshmand, and E. Gholipour, "A comprehensive review on microgrid and virtual power plant concepts employed for distributed energy resources scheduling in power systems," *Renewable and Sustainable Energy Reviews*, vol. 67, pp. 341–363, 2017.

[97] X. Ke, N. Samaan, J. Holzer, R. Huang, B. V. M. Vallem, M. Elizondo, N. Lu, X. Zhu, B. Werts, Q. Nguyen *et al.*, "Coordinative real-time sub-transmission volt-var control for reactive power regulation between transmission and distribution systems," *IET Generation, Transmission & Distribution*, 2018.

[98] N. Etherden, V. Vyatkin, and M. H. Bollen, "Virtual power plant for grid services using IEC 61850," *IEEE Transactions on Industrial Informatics*, vol. 12, no. 1, pp. 437–447, 2016.

[99] R. Isermann, J. Schaffnit, and S. Sinsel, "Hardware-in-the-loop simulation for the design and testing of engine-control systems," *Control Engineering Practice*, vol. 7, no. 5, pp. 643–653, 1999.

[100] C. Dufour, C. Andrade, and J. Belanger, "Real-time simulation technologies in education: a link to modern engineering methods and practices," in *Proc. 11th Int. Conf. on Engineering and Technology Edu.(INTERTECH 2010)*, 2010, pp. 7–10.

[101] D. Jung and P. Tsiotras, "Modeling and hardware-in-the-loop simulation for a small unmanned aerial vehicle," in *AIAA Infotech@ Aerospace 2007 Conference and Exhibit*, 2007, p. 2768.

[102] A. Dubey, S. Chakrabarti, and V. Terzija, "Testing and validation of a dynamic estimator of states in opal-rt real time simulator," in *Power & Energy Society General Meeting, 2017 IEEE*. IEEE, 2017, pp. 1–5.

[103] M. Chamana, K. Prabakar, B. Palmintier, and M. M. Baggu, "Conversion and validation of distribution system model from a QSTS-based tool to a real-time dynamic phasor simulator," in *Green Technologies Conference (GreenTech), 2017 Ninth Annual IEEE*. IEEE, 2017, pp. 219–225.

[104] T. S. Basso and R. DeBlasio, "IEEE 1547 series of standards: interconnection issues," *IEEE Transactions on Power Electronics*, vol. 19, no. 5, pp. 1159–1162, 2004.

[105] V. Jalili-Marandi, F. J. Ayres, E. Ghahremani, J. Belanger, and V. La-´ pointe, "A real time dynamic simulation tool for transmission and distribution power systems," in *Power and Energy Society General Meeting (PES), 2013 IEEE*. IEEE, 2013, pp. 1–5.

[106] P. Siemens, "Power technologies inc," *PSS/E*, vol. 33, 2011.

[107] V. Jalili-Marandi, J. Belanger, and F. J. Ayres, "Model-in-the-loop realtime simulation in phasor domain," in *Industrial Electronics (ISIE), IEEE 23rd International Symposium on*. IEEE, 2014, pp. 2280–2284.

[108] https://www.mathworks.com/help/physmod/sps/powersys/ref/windturbinedoublyfedinductiongeneraorphasortype.html